

**RESONANT OPTICAL CAVITIES FOR THE
MEASUREMENT OF ATMOSPHERIC TRACE GASES**

IAN R. BURLING

A DISSERTATION SUBMITTED TO THE FACULTY OF GRADUATE STUDIES
IN PARTIAL FULFILMENT OF THE REQUIREMENTS
FOR THE DEGREE OF
DOCTOR OF PHILOSOPHY

GRADUATE PROGRAMME IN CHEMISTRY
YORK UNIVERSITY
TORONTO, ONTARIO

MARCH 2008

**RESONANT OPTICAL CAVITIES FOR THE
MEASUREMENT OF ATMOSPHERIC TRACE
GASES**

by **Ian R. Burling**

a dissertation submitted to the Faculty of Graduate Studies of
York University in partial fulfilment of the requirements for
the degree of

DOCTOR OF PHILOSOPHY

©

Permission has been granted to: a) YORK UNIVERSITY LIBRARIES to lend or sell copies of this dissertation in paper, microform or electronic formats, and b) LIBRARY AND ARCHIVES CANADA to reproduce, lend, distribute, or sell copies of this dissertation anywhere in the world in microform, paper or electronic formats *and* to authorize or and procure the reproduction, loan, distribution or sale of copies of this dissertation anywhere in the world in microform, paper or electronic formats.

The author reserves other publication rights, and neither the dissertation nor extensive extracts from it may be printed or otherwise reproduced without the author's written permission.

ABSTRACT

The highly sensitive cavity enhanced and cavity ringdown laser absorption spectroscopy techniques were investigated for the measurement of trace gases in the near-infrared and visible regions of the spectrum. An instrument was developed using the cavity enhanced absorption technique for measurement of CO₂, CO, and NH₃ in the near-IR. The highly-reflective mirrors in the near-IR produced effective pathlengths in the range of 2.5 to 3 km. The minimum detectable fractional absorbance was determined to be $3.7 \times 10^{-8} \text{ cm}^{-1}$ resulting in 3σ detection limits for CO₂ and NH₃ of 10 ppm and 10 ppb, respectively. The cavity enhanced absorption technique was extended to the visible region for detection of the nitrate radical, NO₃. Due to the higher reflectivity of the mirrors, the sensitivity was improved offering effective pathlengths of nearly 20 km, resulting in a minimum detectable fractional absorbance of $3 \times 10^{-10} \text{ cm}^{-1}$ using O₃ and NO₂ as test gases. Due to the strong dependence of pathlength on the alignment, frequent calibration was required. In addition, significant losses were observed when sampling NO₃ through the glass inlet and cavity due to the relatively long residence times within the cavity.

Cavity ringdown spectroscopy was applied to the investigation of NO₃ with adaptations to the software and sampling instrumentation to reduce the residence time and wall losses. Since cavity ringdown is an absolute absorption measurement, pathlength calibration is no longer required. In cavity ringdown spectroscopy the rate of

decay of light exiting an optical cavity is measured, making this technique immune to intensity variations of the laser source. The detection limit for NO_3 was 0.3 ppt neglecting sampling losses yielding a minimum detectable fractional absorbance of $1.5 \times 10^{-10} \text{ cm}^{-1}$. The first-order wall loss constant of NO_3 , k_{wall} , was determined to be 0.48 s^{-1} .

Nighttime ambient measurements of NO_3 and N_2O_5 were performed for four weeks in the summer of 2007 at York University using the cavity ringdown instrumentation modified for portability. With the exception of one evening immediately after sunset, NO_3 was below the detection limit of 2.0 ppt ($\alpha = 9.8 \times 10^{-10} \text{ cm}^{-1}$) during the entire study.

The cavity ringdown technique offered the best sensitivity of the techniques studied, and could be improved for ambient measurements by improving stability in the field and reducing sampling losses.

ACKNOWLEDGMENTS

There are many people that I owe a debt of gratitude. Among those, I would like to thank:

My supervisor, Dr Geoff Harris for your support and guidance with this research and for keeping me on track.

My supervisory committee, Dr Don Hastie and Dr Rob McLaren for your helpful and excellent advice.

Special thanks to Dr Corinne Schiller for all your help during late nights and weekends. Thanks for restoring my confidence whenever I needed it (every other day). Thanks also for helping proofread this thesis and thus making my grammar gooder.

All my many lab mates past and present: Rhian, Tina, Jean-François, Jeremy, Andrew and all who made coming into the lab everyday enjoyable.

All the members of the CAC, especially Carol, without whom none of this would have been possible (thanks for keeping me caffeinated). Thanks to all the groups I borrowed equipment from.

Special thanks to my family for your support even though you had no idea what I was doing (just like me!).

And most importantly, Briar, my wife, for your overwhelming support and infinite patience during this roller coaster ride. I would not have come this far without you.

TABLE OF CONTENTS

<u>ABSTRACT</u>	IV
<u>ACKNOWLEDGMENTS</u>	VI
<u>TABLE OF CONTENTS</u>	VII
<u>LIST OF TABLES</u>	XI
<u>LIST OF FIGURES</u>	XII
<u>1 INTRODUCTION</u>	1
<u>1.1 General Overview</u>	1
<u>1.2 Spectroscopic Methods</u>	1
<u>1.3 High Finesse Resonant Optical Cavities</u>	3
<u>1.4 Longitudinal and Transverse Cavity Modes</u>	6
<u>1.5 Mode-Matching and Off-Axis Cavity Alignment</u>	8
<u>1.6 Cavity Ringdown Laser Absorption Spectroscopy</u>	10
<u>1.7 Continuous-wave Cavity Ringdown Spectroscopy</u>	13
<u>1.8 Cavity Enhanced Absorption Spectroscopy</u>	14
<u>1.9 Use of Cavity Methods for the Detection of Atmospheric Gases</u>	17
<u>1.10 The Nitrate Radical, NO₃</u>	18
<u>1.11 Research Objectives</u>	23
<u>2 CAVITY ENHANCED ABSORPTION SPECTROSCOPY</u>	25
<u>2.1 Near-Infrared CEA Spectroscopy</u>	25
<u>2.1.1 FTIR and HITRAN Spectra in the Near-IR</u>	25

<u>2.1.2</u>	<u>Characterization of Near-IR Lasers</u>	27
<u>2.1.3</u>	<u>CEA Instrument Design in the Near-IR</u>	31
<u>2.1.3.1</u>	<u>Optical Setup in the Near-IR</u>	31
<u>2.1.3.2</u>	<u>Gas Sampling System for the Near-IR</u>	33
<u>2.1.3.3</u>	<u>Electronic Setup for Near-IR Cavity Enhanced Absorption Experiments</u>	35
<u>2.1.3.4</u>	<u>The Integrator Circuit</u>	38
<u>2.1.3.5</u>	<u>CEA Data Acquisition</u>	40
<u>2.1.4</u>	<u>Initial Setup and Alignment Procedure</u>	44
<u>2.1.5</u>	<u>Cavity Enhanced Absorption Measurements of CO₂</u>	45
<u>2.1.5.1</u>	<u>Effect of Laser and Cavity Length Modulation On On-Axis CEA of CO₂</u>	45
<u>2.1.5.2</u>	<u>Effect of Sample Pressure on Sensitivity</u>	46
<u>2.1.5.3</u>	<u>Detection Limits of CEA of CO₂</u>	49
<u>2.1.5.3.1</u>	<u>Instrument Stability Analysis: Allan Variance</u>	49
<u>2.1.5.3.2</u>	<u>Cavity Enhanced Absorption Spectra of CO₂</u>	51
<u>2.1.5.3.3</u>	<u>Spectra after Hardware and Software Modifications</u>	54
<u>2.1.6</u>	<u>Near-IR Cavity Enhanced Absorption of NH₃</u>	55
<u>2.1.7</u>	<u>Summary of CEA Results in the Near-IR</u>	57
<u>2.2</u>	<u><i>Cavity Enhanced Absorption in the Visible Region</i></u>	59
<u>2.2.1</u>	<u>Overview</u>	59
<u>2.2.2</u>	<u>Instrumental Setup for CEA in the Visible Region</u>	62
<u>2.2.3</u>	<u>Visible Diode Laser Characterization</u>	66
<u>2.2.4</u>	<u>Laboratory Synthesis of N₂O₅</u>	67

2.2.5	<u>Characterization of the N₂O₅ Sample</u>	71
2.2.6	<u>Gas Sampling System for the Detection of NO₃ in the Visible Region</u>	73
2.2.7	<u>Visible Cavity Effects as a Diagnostic Tool</u>	75
2.2.8	<u>CEA Tests in the Visible Region</u>	77
2.2.8.1	<u>Pathlength and Sensitivity Determination</u>	77
2.2.8.2	<u>Parameter Optimization of CEA in the Visible Region</u>	81
2.2.8.3	<u>Temperature and Pressure Effects on Cavity Output</u>	81
2.2.9	<u>In Situ Production of NO₃</u>	82
2.2.10	<u>Cavity Enhanced Absorption Using Solid N₂O₅ as the NO₃ Source</u>	85
2.2.11	<u>Summary of Results of CEA in the Visible Region</u>	91
3	<u>CAVITY RINGDOWN SPECTROSCOPY FOR NO₃ DETECTION</u>	93
3.1	<u>Instrument Design</u>	93
3.2	<u>Laboratory Tests of CRD Applied to NO₃ Detection</u>	96
3.2.1	<u>Generation and Analysis of Ringdown Signals</u>	96
3.2.2	<u>Determination of the L/d Factor</u>	99
3.2.3	<u>Comparison of Simultaneous Cavity Ringdown and Integrated Cavity Output</u>	100
3.2.4	<u>Cavity Ringdown Experiments of NO₃</u>	104
3.2.4.1	<u>Determination of the Wall Loss Constant for NO₃</u>	104
3.2.4.2	<u>Temperature Dependence on the NO₃ Losses</u>	107
3.2.4.3	<u>NO Titration of NO₃</u>	115
3.2.4.4	<u>Characterization of Potential Spectroscopic Interferences</u>	119
4	<u>CONTINUOUS-WAVE CAVITY RINGDOWN AMBIENT STUDY OF NO₃</u>	121

4.1.1	<u>Portable Cavity Ringdown Setup for Ambient NO₃ and N₂O₅ Measurements</u>	121
4.1.2	<u>Thermal Conversion of N₂O₅ in the Cavity under Ambient Conditions</u>	125
4.1.3	<u>NO₃ and N₂O₅ Measurement Site</u>	126
4.2	<u>Ambient NO₃ and N₂O₅ Measurements at York University</u>	127
4.3	<u>Nitrate Radical Chemistry at York University</u>	132
5	<u>CONCLUSIONS AND FUTURE WORK</u>	139
6	<u>REFERENCES</u>	143

LIST OF TABLES

Table 2-1	Estimates of detection limits of various species in the near-IR.....	58
Table 2-2	Comparison of CEA experiments of heated cavity with model results using N ₂ O ₅ as the NO ₃ source	89
Table 4-1	Summary of results of nighttime outdoor measurements at York University during the summer of 2007. All nights resulted in observed mixing ratios below the detection limits with the exception of July 30 – 31. Detection limits are based on the statistical detection limit given by equation E3.2. A summary of the ozone characteristics is also shown.....	133
Table 4-2	Fractional hourly loss rate for reaction of various VOCs with OH, O ₃ , and NO ₃ . Room temperature rate constants in brackets (cm ³ molecule ⁻¹ s ⁻¹). OH, O ₃ , and NO ₃ mixing ratios held constant at 0.1 ppt, 30 ppb and 2 ppt, respectively. References: * Atkinson (1990), †Platt et al. (1990).....	137
Table 4-3	Comparison of detection limits of various nitrate radical based spectroscopic instruments with integration time and confidence levels as reported in the references. The optical detection limit is the instrumental performance based on the minimum detected fractional absorbance, whereas the experimental detection limit takes into account the system losses	138

LIST OF FIGURES

Figure 1-1	a) Example of standing wave created from constructive interference when resonance condition satisfied (note: the standing wave shown above is shown with nodes at the ends but this is not necessary); b) Example of destructive interference producing no cavity output.....	5
Figure 1-2	Example of some TEM _{mn} mode output patterns (Silfvast, 1996)	7
Figure 1-3	Summary of relevant atmospheric reactions involving NO ₃	19
Figure 2-1	HITRAN linestrengths and FTIR spectra of various species in the near-IR	26
Figure 2-2	Laser emission wavelength as a function of laser current and temperature with HITRAN line positions and linestrengths	28
Figure 2-3	Laser output wavelength as a function of laser temperature and current (squares) with respect to the NH ₃ absorption spectrum (Lundsberg-Nielsen et al. 1993) (triangles) and H ₂ O linestrengths (circles)	30
Figure 2-4	Direct laser absorption of 6.4 Torr NH ₃ in 230 Torr N ₂ in a 14 cm cell (dotted curve) and reference absorption spectrum (triangles Lundsberg-Nielsen et al., 1993))	30
Figure 2-5	Manufacturer specified reflectivity curve of second set of highly reflective mirrors in the near-IR. The y-axis, %T, is equivalent to 100%-R (reflectivity).....	32
Figure 2-6	Optical setup and gas sampling system for CEA experiments in the near-IR	34
Figure 2-7	Electronic setup for CEA experiments.....	37
Figure 2-8	Schematic of op-amp integrator circuit. The gain could be controlled by varying the combination of resistors (R) and capacitors (C).....	39
Figure 2-9	Integrated signal of a 40 mV DC signal from TAMS software and hardware showing inconsistent timing	40

Figure 2-10 Timing of counter and triggering scheme of new Labview program for accurate timing of integrator switch.....	42
Figure 2-11 Integrated signal of a 40 mV DC signal from Labview software and new hardware showing consistent timing.....	43
Figure 2-12 Example of integration (black line) of the actual cavity output (grey data)	44
Figure 2-13 Effect of frequency modulation on integrated cavity output of CO ₂ near 1569.494 nm	46
Figure 2-14 Effect of pressure on absorption linewidth for constant concentration (1 Torr CO ₂ in variable N ₂ total pressures)	48
Figure 2-15 Absorption coefficient, $\alpha = A/L$ for 210 ppm CO ₂ as a function of pressure for the absorption line at 1570.80 nm.....	48
Figure 2-16 Allan plot for CEA experiment of 105 ppm CO ₂	50
Figure 2-17 Continuous series of 60 second average CEA scans of 210 ppm CO ₂ showing good stability (upper curve) and alignment drift (lower curve).....	53
Figure 2-18 Background subtracted spectrum of upper spectrum of Figure 2-17.....	54
Figure 2-19 CEA of CO ₂ with background subtraction for old TAMS software (dotted curve) and new Labview software and hardware (solid curve).....	55
Figure 2-20 CEA background subtracted absorption of 361 ppm NH ₃ (solid curve) and consecutive background – background results (dotted curve) normalized to 10 V	56
Figure 2-21 Absorption cross-sections of NO ₃ in the visible region (Sander et al., 2006).....	60
Figure 2-22 Absorption cross-sections of O ₃ and NO ₂ near 662 nm.....	62
Figure 2-23 Initial cavity setup for experiments in the visible region. The shaded region is the heated section. All glass is 1” OD	64
Figure 2-24 Manufacturer specified reflectivity curve for the highly reflective mirrors near 662 nm. The y-axis, %T, is equivalent to 100%-R (reflectivity).....	64

Figure 2-25 Modified cavity setup for experiments in the visible region. The shaded area is the heated section	65
Figure 2-26 NO ₃ laser output wavelength (nm) as a function of laser temperature and current	67
Figure 2-27 Trap to trap distillation setup for N ₂ O ₅ synthesis.....	68
Figure 2-28 Simplified single mixing scheme (Crowley, J., personal communication) for N ₂ O ₅ production.....	70
Figure 2-29 N ₂ O ₅ vapour pressure as a function of temperature (Linde, 2005).....	71
Figure 2-30 Mid-IR absorption cross-sections for N ₂ O ₅ , NO ₂ and HNO ₃ ; NO ₂ and HNO ₃ calculated from HITRAN database (Rothman et al., 2004) and N ₂ O ₅ from Cantrell et al. (1988).....	72
Figure 2-31 FTIR spectra of N ₂ O ₅ sample produced from trap-to-trap distillation (lower spectrum) and single mixing (Crowley, J., personal communication) (upper spectrum).....	73
Figure 2-32 Double dilution flow arrangement for CEA and CRD for N ₂ O ₅ and NO ₃ in the visible region	74
Figure 2-33 Photographs of off-axis cavity output as viewed on a white card approximately 1 to 2 m from the cavity output mirror. Photographs 1a to 1c show the typical TEM _{mn} modes obtained from off-axis alignment	76
Figure 2-34 2 second averages (grey curve) of integrated cavity signal over time showing decrease in signal with addition of NO ₂ ; the black portions are the sections used in the 5 minute average.....	78
Figure 2-35 Calibration curve of cavity enhanced absorbance for various mixing ratios of NO ₂	78
Figure 2-36 2 second averages (grey data) of integrated cavity signal over time showing decrease in signal with addition of O ₃ ; the black portions are the sections used in the 5 minute average.....	80
Figure 2-37 Calibration curve for cavity enhanced absorbance of various mixing ratios of O ₃	80

Figure 2-38 Examples of the integrated cavity enhanced absorption signal as NO_2 and O_3 are added producing NO_3 for the inlet and cavity heated to 90°C	83
Figure 2-39 Simple Accuchem model for in situ production of N_2O_5 and NO_3 showing mixing at room temperature for the first 84 seconds, followed by heating at 90°C . The cavity residence time is shown by the grey section	84
Figure 2-40 Cavity enhanced absorption results for addition of O_3 and solid N_2O_5 sample from Aug. 29, 2006 for a cavity and inlet temperature of 70°C ; modeled NO_3 mixing ratio shown as triangles	86
Figure 2-41 Modeled room temperature concentrations of NO_3 , N_2O_5 and NO_2 in the FTIR cell from the N_2O_5 sample. In this case, $\text{NO}_2 = \text{NO}_3$	87
Figure 2-42 Modeled room temperature results after double dilution of N_2O_5 , NO_3 and NO_2 from the solid N_2O_5 source. In this case, $\text{NO}_2 = \text{NO}_3$	88
Figure 2-43 Modeled results of N_2O_5 , NO_3 and NO_2 after double dilution and heating to a cavity and inlet temperature of 80°C ($\text{NO}_3 = \text{NO}_2$)	88
Figure 3-1 Cavity setup for cavity ringdown experiments. The shaded area is the heated section	94
Figure 3-2 Actual detected cavity output signal with laser chop rate of 20 Hz (generating 20 ringdown decays per second)	97
Figure 3-3 Actual detected ringdown signals for 1 second at 50 Hz (50 ringdowns in one second) showing fitted region in black	98
Figure 3-4 Normalized ringdown signals of Figure 3-3 showing independence of ringdown on initial intensity – all ringdowns are nearly identical	99
Figure 3-5 Comparison of simultaneous integrated cavity output lock-in detection and cavity ringdown signals for O_3 absorption	101
Figure 3-6 Improved cavity ringdown signal for various O_3 additions	103
Figure 3-7 Ringdown results of various additions of NO_3 from solid N_2O_5 source over time with sample inlet and cavity at room temperature – comparison of experimental and modeled NO_3 concentrations for determination of wall loss constant	106

Figure 3-8 CRD experiment of variable additions of N_2O_5 as NO_3 source over time at an inlet and cavity temperature of $70^\circ C$ – comparison of experimental and modeled NO_3 concentrations	108
Figure 3-9 CRD experiment of variable additions of N_2O_5 as NO_3 source over time at inlet and cavity temperature of $90^\circ C$ – comparison of experimental and modeled NO_3 concentrations	109
Figure 3-10 CRD experiment of variable additions of N_2O_5 as NO_3 source over time at inlet and cavity temperature of $105^\circ C$ – comparison of experimental and modeled NO_3 concentrations	109
Figure 3-11 Comparison of experimentally determined NO_3 concentration with modeled NO_3 for various cavity temperatures; 1:1 ratio shown by the diagonal line (note the error bars, determined from (E3.2), are not shown here as they are within the size of the points)	110
Figure 3-12 Normalized NO_3 concentration as a function of temperature from Brown et al. (2002a)	112
Figure 3-13 Comparison of experimentally determined NO_3 concentration with modeled NO_3 including thermal decomposition for various cavity temperatures; 1:1 ratio shown by the diagonal line (note the error bars, determined from (E3.2), are not shown here as they are within the size of the data points)	114
Figure 3-14 Effect of inlet and cavity temperature on experimentally determined NO_3 for similar initial N_2O_5 conditions	115
Figure 3-15 Ringdown experiment with addition of NO to room temperature inlet and cavity to effectively titrate NO_3 from the N_2O_5 solid source.....	117
Figure 3-16 Simulation of addition of 50 ppb NO to ambient room temperature air ($NO_3 = 10$ ppt, $N_2O_5 = 50$ ppt)	118
Figure 3-17 Simulation of addition of 50 ppb NO to heated air at 353 K ($NO_3 = 10$ ppt, $N_2O_5 = 50$ ppt)	119
Figure 4-1 Compact optical setup on breadboard for ambient measurements.....	122
Figure 4-2 Flow system for ambient CRD measurements of NO_3	124
Figure 4-3 Simulation of thermal conversion of N_2O_5 to NO_3 at 353 K with 20 ppb NO_2 initially ($NO_3 = 10$ ppt, $N_2O_5 = 50$ ppt).....	126

Figure 4-4 Simulation of thermal conversion of N_2O_5 to NO_3 at 353 K with 50 ppb NO_2 initially ($NO_3 = 10$ ppt, $N_2O_5 = 50$ ppt).....	126
Figure 4-5 July 30 - 31, 2007, Meteorological conditions and NO_3 results of outdoor CRD for unheated inlet and cavity corrected for NO_2 production during background titration with NO and wall and filter losses. Positive data points were multiplied by the wall and filter loss factor with the error bars equivalent to the standard deviation in τ_0 ; Negative data points were not corrected for the wall and filter loss although the positive error bar represents the standard deviation in τ_0 multiplied by the wall and filter loss factor	129
Figure 4-6 Aug 8 – 9, 2007 meteorological data and $N_2O_5 + NO_3$ ambient results of heated cavity corrected for wall loss and for NO_2 production during background titration with NO (as described in Figure 4-5	132

1 INTRODUCTION

1.1 *General Overview*

With increasing public awareness and concern with the environment and in particular, atmospheric pollution, global warming and climate change, there is a great deal of interest in understanding the various mechanisms and components of the atmosphere. While only comprising a very small fraction of the atmosphere, trace gases are very important factors regarding air quality and climate change.

To further enhance understanding of the chemistry of the atmosphere, sensitive measurements of the various components are necessary. Techniques are constantly developed for detection of various trace gases. Spectroscopic methods are a valuable tool for *in situ* detection and quantification of trace gases, drawing upon the ability for small molecules to absorb discrete wavelengths of radiation dependent upon their size and structure.

1.2 *Spectroscopic Methods*

Electromagnetic radiation from a source (laser, lamp, sunlight, etc.) is attenuated as it passes through a sample. In absorption spectroscopy of gas samples, the molecules of the sample absorb photons of wavelengths corresponding to their characteristic transitions. The transitions corresponding to absorbance in the mid- and near-infrared

regions of the electromagnetic spectrum are vibrational transitions combined with rotational transitions. The rotational structure is typically well defined for smaller molecules and lower sample pressures. The mid-infrared vibrations are fundamental transitions and are typically of higher absorption strength than the vibrational transitions in the near-IR which are combinations and overtones of the fundamental vibrations. In the higher energy visible region, the transitions are vibronic (electronic, vibrational and unresolved rotational). These vibronic transitions are typically stronger than the infrared transitions but are also considerably broadened and thus overlap with vibronic transitions of other molecules can occur.

In the typical absorption spectroscopy experiment the intensity of the light at the source, $I_0(\lambda)$, at wavelength, λ , is compared to the intensity of the light, $I(\lambda)$, after passing through a certain pathlength of sample, L . At the detector, $I(\lambda)$ is attenuated according to the Beer-Lambert law of absorption:

$$\begin{aligned} I(\lambda) &= I_0(\lambda) \exp(-\sigma(\lambda)L[X]) \\ I(\lambda) &= I_0(\lambda) \exp(-\alpha(\lambda)L) \end{aligned} \tag{E1.1}$$

where $\sigma(\lambda)$ is the absorption cross-section relating to the ability of the molecule to absorb radiation at a particular wavelength, and $[X]$ is the concentration of species X . For the gas phase, σ and $[X]$ are given typically in the units of $\text{cm}^2 \text{ molecule}^{-1}$ and molecules cm^{-3} , respectively. The quantity, $\sigma(\lambda) \times [X]$, is the absorption coefficient, $\alpha(\lambda)$, and $\sigma(\lambda)L[X]$ is the absorbance, A . The concentration of a particular species can be determined by choosing a wavelength at which only the species of interest absorbs

radiation strongly, thus minimizing interferences from other species. The intensity I_0 is usually determined from a background spectrum where the species of interest is absent. Often, the concentration of the species is obtained by comparing the sample spectrum to the spectrum of a well-quantified calibration source.

One drawback with the straightforward laser absorption experiment is the difficulty with discriminating a small change in intensity from an intense detected baseline signal. This is often the determining factor relating to the detection limit of direct absorption techniques. Small fluctuations in the source output I_0 contribute a large noise portion to the detected signal. Sensitivity can be increased in this case by increasing the pathlength or by modulation methods. Alternatively, the dependence on the initial intensity can be eliminated with other techniques using resonant optical cavities, such as cavity ringdown spectroscopy.

With recent technological advances in telecommunications, lasers and other instrumental components for the near-infrared and visible regions are readily available, relatively cheap and lead to compact instrumentation.

1.3 High Finesse Resonant Optical Cavities

The use of high finesse optical cavities can increase sensitivity by increasing the time the radiation is in contact with the sample, thus increasing the effective pathlength. Two or more highly reflective mirrors (>99.9%) form the optical cavity. These cavities differ from multipass cells in that the radiation is injected *through* one of the highly

reflective mirrors into the cavity and reflects back and forth traversing the same path with each reflection, with some light exiting the cavity by transmission through the highly reflective mirrors with each reflection. When radiation from a continuous-wave laser is input into an optical cavity, the wavelike properties of the radiation must be considered since the optical cavity acts as an interferometer. As the beam reflects back and forth within the cavity, it interferes with light from previous reflections and light that is continuously injected into the cavity. The radiation within the cavity can interfere either constructively or destructively. In the case of destructive interference, as the beam reflects back and forth, with each round trip there is a phase shift in the wave. Since the beam is essentially trapped within the cavity for upwards of a thousand reflections, these phase shifts cause the beam to interfere destructively, with the result that there is no intensity within the cavity and thus no intensity at the detector (see Figure 1-1b). On the other hand, if the beam remains in phase as it propagates within the cavity, the light within the cavity interferes constructively, a very intense buildup of radiation occurs, and a strong signal is observed at the detector (see Figure 1-1a). The cavity and laser are said to be in resonance. The light within the cavity can build up to several watts from a laser source of only a few milliwatts.

Those wavelengths (λ) at which the resonance condition is satisfied are given by:

$$2L = q\lambda \quad (\text{E1.2})$$

where q is an integer and L is the mirror separation. The frequency separation between consecutive resonances q to $q+1$ is defined by the free spectral range of the cavity, ν_{fsr} :

$$\nu_{fsr} = \frac{c}{2L} \quad (\text{E1.3})$$

where c is the speed of light, and L is the mirror separation.

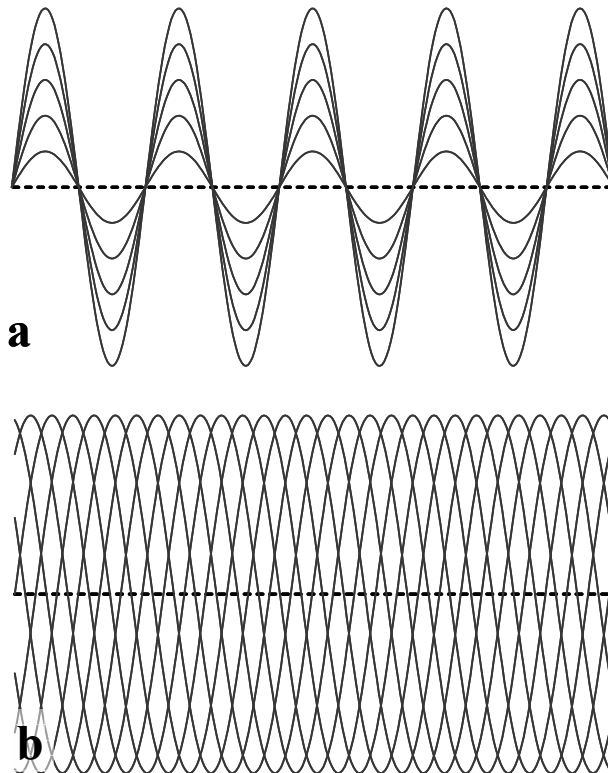


Figure 1-1 a) Example of standing wave created from constructive interference when resonance condition satisfied (note: the standing wave shown above is shown with nodes at the ends but this is not necessary); b) Example of destructive interference producing no cavity output

The full-width at half max (FWHM), $\nu_{1/2}$, of the resonance peaks is dependent on the mirror reflectivity R (Yu and Yang, 1997):

$$\Delta \nu_{1/2} = \frac{c}{2L} \frac{1 - \sqrt{R_1 R_2}}{\pi (R_1 R_2)^{1/4}} \quad (\text{E1.4})$$

The cavity finesse, F , is given by the ratio of the free spectral range to the FWHM (Mazurenka, *et al.*, 2005):

$$F = \frac{\nu_{fsr}}{\Delta \nu_{1/2}} = \frac{\pi (R_1 R_2)^{1/4}}{1 - \sqrt{R_1 R_2}} \quad (\text{E1.5})$$

For example, for a cavity with mirror reflectivities $R_1 = R_2 = 99.99\%$, separated by 1 m, the free spectral range is 150 MHz, $\Delta \nu_{1/2} = 4.8$ kHz, and the finesse is 31400. For the typical continuous-wave tunable diode laser the laser linewidth is approximately 10 MHz, which is considerably less than the free spectral range of the cavity. The high finesse implies that only those frequencies of the input laser that match the cavity resonance conditions will transmit through the cavity. All other wavelengths will have a transmitted intensity of zero. On the other hand, the typical tunable pulsed laser sources (Nd:YAG pumped dye lasers) have linewidths much greater than the free-spectral range of such a cavity, thus ensuring the resonance condition is satisfied with each laser pulse.

1.4 Longitudinal and Transverse Cavity Modes

The simple example of the cavity resonance condition above considers only the resonance in the axial direction of the cavity consisting of plane mirrors. For a Gaussian beam coupled to a resonant cavity consisting of spherical mirrors, the cavity output may

also exhibit transverse mode resonance dependent on the geometry of the cavity; specifically the mirror separation, L , and the mirror radius of curvature, r (not to be confused with the mirror reflectivity, R). The general expression for the resonance modes of a cavity is given by (Berden *et al.*, 2000):

$$v_{mnq} = \frac{c}{2L} \left\{ q + \frac{(1+m+n)}{\pi} \arccos \sqrt{\left(1 - \frac{L}{r_1}\right) \left(1 - \frac{L}{r_2}\right)} \right\} \quad (\text{E1.6})$$

where q is the longitudinal mode index, and m and n are the transverse mode indices ($m, n, q = \text{integers}$). These ‘‘Hermite-Gaussian’’ modes are denoted TEM_{mn} (Transverse ElectroMagnetic) modes. A sample of the cavity output of some TEM_{mn} cavity modes is shown in Figure 1-2 (Silfvast, 1996).

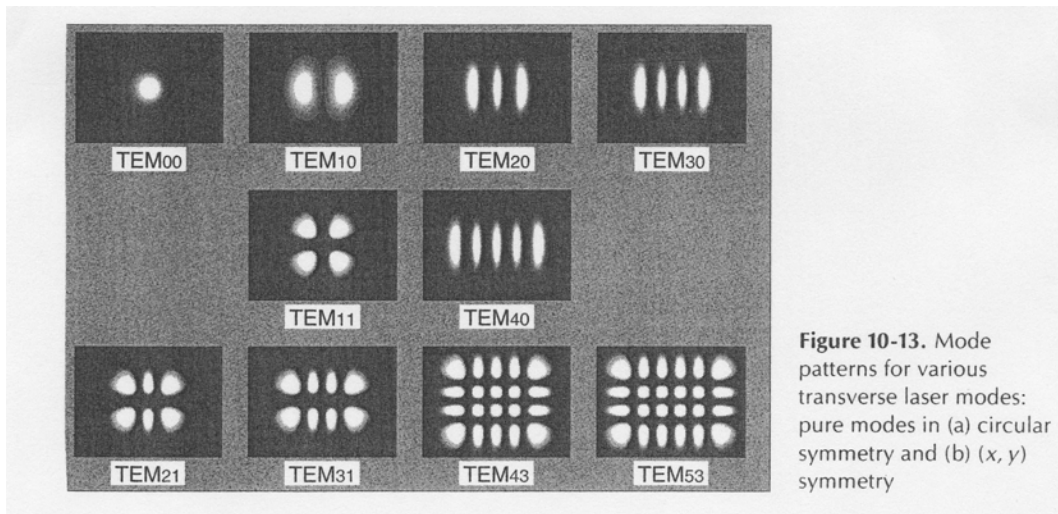


Figure 1-2 Example of some TEM_{mn} mode output patterns (Silfvast, 1996)

1.5 Mode-Matching and Off-Axis Cavity Alignment

In order to ensure that only one transverse mode is excited within the cavity, the laser and cavity can be mode-matched. Typically, the laser is mode-matched to the fundamental transverse electromagnetic mode, TEM₀₀. This mode-matching is achieved by matching the beam waist of the laser beam to the natural waist of the cavity. The natural waist of a cavity, ω_0 , formed by concave mirrors of radius of curvature, $r_1 = r_2 = r$, and separated by a distance L is given by (Kogelnik and Li, 1966):

$$\omega_0^2 = \frac{\lambda}{2\pi} \sqrt{L(2r - L)} \quad (\text{E1.7})$$

The laser beam waist can be matched to the cavity waist with a simple two-lens telescope system.

When the laser is matched to the TEM₀₀ cavity mode and aligned coincident with the cavity axis, the free spectral range of the cavity is given by equation (E1.3) shown previously. If the laser is then aligned slightly off the cavity axis by adjustment of the input angle or position into the cavity the beam no longer retraces the same path with each roundtrip. The beam reflects back and forth within the cavity following a “folded path”. The beam traces an elliptical pattern on the mirrors rather than a single spot. With each reflection through the cavity, the spot on the mirror is rotated about the cavity axis by an angle θ . For a cavity composed of concave-concave mirrors, the angle is dependent only on the geometric factors of the cavity, the mirror separation and the radius of curvature (Herriott and Schulte, 1965):

$$\cos \theta = \left(1 - \frac{L}{r}\right) \quad (\text{E1.8})$$

where $r_1 = r_2 = r$. After a number of roundtrips within the cavity, the beam retraces its original path. At this point, the beam is said to be “re-entrant”. The re-entrant condition is satisfied when after j roundtrips the rotation is an integer multiple of 2π :

$$2j\theta = 2k\pi \quad (\text{E1.9})$$

where k is an integer. The key aspect of off-axis alignment is that the free spectral range, ν_{fsr} , decreases as the number of roundtrips increases to satisfy the reentrant condition. By decreasing the free spectral range, the resonance condition becomes slightly more relaxed. If the free spectral range is reduced to less than the bandwidth of the laser, the resonance condition is thus satisfied for all wavelengths of the laser scan. By introducing an astigmatism to one or both of the mirrors, a Lissajous spot pattern is formed on the mirrors (McManus *et al.*, 1995) equivalent to a reentrant condition satisfied after several hundred to many thousand roundtrips.

The number of roundtrips the beam makes before becoming reentrant is only dependent on the geometry of the cavity. Careful consideration of the geometric factors can help to reduce the resonant peak contrast with an off-axis alignment.

With high finesse optical cavities, much of the intensity of the initial laser radiation is reflected back towards the laser or transmitted through the entrance mirror when resonance occurs. Back-reflection on to the laser can create optical feedback which affects the output of the laser, and is thus undesirable. When the cavity is aligned off-

axis, the back-reflection no longer hits the laser, eliminating the need for expensive optical isolation components.

1.6 Cavity Ringdown Laser Absorption Spectroscopy

Several spectroscopic methods have been developed taking advantage of the increase in sensitivity due to the long pathlengths achievable with resonant optical cavities. The introduction of Cavity Ringdown Laser Absorption Spectroscopy, CRLAS or CRD, in the late 1980s provided a novel method for the study of very weak absorptions (O'Keefe and Deacon, 1988). In conventional absorption experiments, the *amount* of absorption is measured using a continuous radiation source whereas in the typical CRD experiment, absorption information is obtained from the *rate* of absorption by monitoring the rate of decay of light exiting an optical cavity from a pulsed laser source.

In the traditional CRD experiment, a tunable pulsed laser source is used producing a high-energy pulse of radiation of short duration (on the order of a few nanoseconds) and is injected into the optical cavity. Most of the pulse intensity is reflected back towards the laser but a small amount of the pulse is transmitted into the optical cavity created by two highly reflective mirrors separated by length, L . The pulse makes many round-trips within the cavity and with each round-trip, the intensity of the pulse is decreased. The intensity decay within the cavity is caused by losses within the cavity (absorption and scattering, as well as transmission through the mirrors). The

detector is placed behind the exit mirror and detects the small fraction of light transmitted through the cavity. The intensity of light transmitted through the cavity follows a simple single exponential decay.

The ringdown time, τ , is given as the time for the detected intensity to decay to $1/e$ of the initial intensity. A key feature of the CRD technique is that the ringdown time is independent of the initial intensity of the pulse and thus this technique is immune to the problems associated with measuring small changes of intensity over an intense baseline signal and fluctuations in the source intensity. The highly reflective mirrors also ensure that the light is trapped within the cavity for a long time leading to long pathlengths. The ringdown time, and thus the effective pathlength, is dependent on the mirror reflectivities. The higher the reflectivity, the longer the effective pathlength.

The ringdown time, τ , is given as (Mazurenka *et al.*, 2005):

$$\tau = \frac{L}{c} \frac{1}{[(1-R) + \sigma[X]d]} \quad (\text{E1.10})$$

where R is the mirror reflectivity (assuming the two mirrors have the same reflectivity), L is the mirror separation, c is the speed of light, and $\sigma[X]d$ is the Beer-Lambert equivalent absorption, where d is now the length of the cavity containing the sample.

In the absence of absorbing species, only transmission through the mirrors contributes to the loss of intensity within the cavity. The empty cavity ringdown time, τ_0 , is given by (Mazurenka *et al.*, 2005):

$$\tau_0 = \frac{L}{c} \frac{1}{(1-R)} \quad (\text{E1.11})$$

The concentration can be obtained by determining the ringdown times in the presence and absence of an absorber, τ and τ_0 , respectively. From the above two equations, (E1.10) and (E1.11), the concentration becomes:

$$[X] = \frac{1}{c\sigma} \frac{L}{d} \left(\frac{1}{\tau} - \frac{1}{\tau_0} \right) \quad (\text{E1.12})$$

The factor, L/d , is the ratio of the mirror separation, L , to the length of the cavity containing the sample, d .

In the cavity ringdown experiment, care must be taken to align and set up the cavity such that only one transverse mode is excited by mode-matching the laser to the cavity. Simultaneous excitation of more than one transverse mode within the cavity leads to multiexponential decays and causes uncertainty in the ringdown time determination. The different ringdown time for different transverse modes is due to diffraction losses since the spot patterns on the mirrors for different transverse modes are typically larger with higher m and n (Wheeler *et al.*, 1998).

With highly reflective mirrors, the cavity ringdown technique can achieve effective pathlengths of tens of kilometres with a mirror separation of less than a meter. This results in typical optical density limits (the minimum detectable change in I/I_0) on the order of 10^{-8} and better for the ringdown technique whereas conventional absorption experiment, typically obtained minimum detectable changes in I/I_0 of 10^{-5} at best. The high sensitivity achievable with cavity ringdown spectroscopy makes this technique (and its analogues) well suited towards atmospheric trace gas measurements.

1.7 Continuous-wave Cavity Ringdown Spectroscopy

In the conventional pulsed cavity ringdown experiment, the laser is typically a dye laser pumped by a high-energy laser such as an Nd:YAG. The bandwidth of these laser systems is typically broad so that cavity resonance condition is satisfied for all pulses. These laser systems are usually very bulky and expensive and thus are not very well suited for compact, portable instruments for ambient measurements. Continuous-wave tunable diode lasers are desired for portable instruments due to their small size, and straightforward control electronics. Since the bandwidth of continuous-wave TDLs is much smaller than the free spectral range of an on-axis cavity, special adaptations must be applied for use in the CRD technique. In addition, due to the smaller bandwidth of CW-TDLs they offer greater spectral resolution than pulsed lasers. The CW-CRD technique benefits from greater spectral resolution, compact instrumentation of the CW lasers, while also benefiting from the CRD sensitivity due to the independence of the ringdown signal on intensity variations of the laser source.

The cavity can be locked to the laser so that a single mode is continuously resonant (Romanini *et al.*, 1997). Complex monitoring of the laser and cavity signals via a feedback circuit and continuous automatic adjustment of the cavity length with a piezoelectric transducer achieve locking. When the cavity and laser are locked, the cavity throughput intensity is maximized. The input beam is then rapidly switched off with a fast optical switch (AcoustoOptic Modulator, AOM) and a ringdown decay signal is generated. Locking the cavity to the laser is not straightforward and very sensitive to

external vibration and thermal drift. Thus, it is not particularly suitable for a portable, ambient monitoring system, although it offers excellent sensitivity.

Less complex approaches to CRD with a continuous-wave laser source have also been developed which do not require tracking of the cavity length to the laser frequency. CRD with a continuous-wave laser can be performed with an off-axis alignment to create a dense mode structure (Paul *et al.*, 2001; Kasyutich *et al.*, 2002). With the resonance condition satisfied for all frequencies due to the high number of passes until the beam is reentrant, the cavity throughput is essentially constant. The ringdown signal can be acquired by mechanical chopping of the laser beam at an intermediate focus (Paul *et al.*, 2001; Kasyutich *et al.*, 2001) or by modulating the laser intensity on and off electronically (Ayers *et al.*, 2005).

The method used in this research to generate ringdown signals is to align the cavity off-axis such that there is a near constant throughput of laser intensity while simultaneously modulating the laser source on and off. The laser source is turned on and off by square-wave modulation of the current to the laser diode such that the current is modulated to below threshold of the laser.

1.8 Cavity Enhanced Absorption Spectroscopy

As shown in section 1.3, the high sensitivity resulting from a high finesse optical cavity is due to the thousands of roundtrips within the cavity leading to long effective pathlengths. For a continuous-wave laser, only those laser wavelengths that are resonant with the cavity will transmit through the cavity. When the laser and cavity are resonant,

the buildup of light within the cavity follows a “ringup” profile until the peak intensity is reached, or until the laser and cavity are moved off-resonance. As the laser and cavity are moved off-resonance, the intensity in the cavity follows a “ringdown” exponential decay with the ringup and ringdown times dependent on the various losses within the system as in the CRD technique.

By jittering the cavity length via a piezoelectric transducer (PZT), the frequencies of the various transverse modes change, thus allowing for different laser wavelengths to be transmitted through the cavity. Typically, the cavity length is jittered at a frequency of a few hundred Hertz, over a distance equivalent to a few wavelengths of the laser light, such that several longitudinal modes are transmitted. Modulation of the laser wavelength further randomizes the output of the cavity. In addition, the laser is not mode-matched to one particular transverse mode. Many different transverse modes are excited thus filling in some of the frequency gaps.

Even with the resonance of many transverse modes, the cavity output still fluctuates in and out of resonance, yielding a highly variable detected signal. Time integration of the detected signal for each wavelength step results in a relatively flat signal, reducing the variability of the cavity output significantly. The key to producing a flat transmitted signal is to ensure that all wavelengths are transmitted through the cavity equally. This is typically achieved by designing the cavity such that there is a dense, quasi-continuous mode structure (Engeln *et al.*, 1998) due to the geometry of the cavity, and many transverse modes can be excited according to equation (E1.6). The

geometrical conditions for a quasi-continuous transverse mode structure is given by (Engeln *et al.*, 1998):

$$0 < L < r \quad \text{or} \quad r < L < 2r \quad (\text{E1.13})$$

A cavity setup under these conditions helps to minimize the degeneracy of the various transverse modes and ensures that the beam stays within the cavity with each reflection.

There are many benefits to this Cavity Enhanced Absorption (CEA) technique. Compact and relatively cheap continuous-wave lasers can be employed with no need for external optics to mode-match the laser to the cavity. The technique does not require fast electronics, and highly reflective mirrors are available in many spectral regions.

The primary factor limiting the sensitivity of this technique is the inherent noise created by the cavity mode resonance condition and thus unequal contributions of all wavelengths in the laser scan.

Another method of generating cavity enhancement, Integrated Cavity Output Spectroscopy, ICOS, is a technique very similar to the CEA technique. In fact, in the literature, the two techniques are often considered the same and their names are often used interchangeably. The experimental setups are very similar. In the CEA technique the laser and cavity modulation frequency are slow compared to the ringup and ringdown times. When the resonance condition is satisfied there is enough time for the intensity buildup within the cavity to reach its maximum and enough time to reach the minimum. Thus, the cavity output exhibits the highly variable mode structure. In the ICOS experiment, the laser and cavity are modulated at a rate much faster than the

characteristic ringup and ringdown times. In other words, before the light has a chance to ringup and ringdown fully within the cavity, it is in resonance with another mode which also is not resonant long enough for full buildup to occur. As a result, the cavity output signal is considerably lower in intensity but the residual mode structure is suppressed.

1.9 Use of Cavity Methods for the Detection of Atmospheric Gases

The CEA and ICOS experiments have been applied to the detection of many species. Open-path CEA measurements of NH_3 in the near-IR (Peeters *et al.*, 2000) obtained a 1 second detection limit of 100 ppb. Off-axis ICOS measurements of various species in the near-IR (CO , CH_4 , C_2H_2 and NH_3) were performed by Baer *et al.* (2002), resulting in a minimal detectable absorption of 1.4×10^{-5} . Bakhirkin *et al.* (2004) used a quantum cascade laser in the mid-IR and off-axis ICOS for the measurement of nitric oxide, NO , in exhaled breath and achieved a 10 ppb detection limit with a cavity length of only 5.3 cm.

Several groups have recently developed cavity-based methods for detection of the nitrate radical, NO_3 and/or dinitrogen pentoxide, N_2O_5 . King *et al.* (2000), and Brown *et al.* (2001) developed a pulsed cavity ringdown instrument for detection of NO_3 and N_2O_5 using a Nd:YAG pumped dye laser. Brown *et al.* (2002a) then modified their instrument for simultaneous detection of NO_3 and N_2O_5 by addition of a second cavity. Simpson (2003) introduced a continuous-wave CRD instrument for detection of NO_3 and N_2O_5 where the laser is locked to a cavity mode to ensure resonance. Ayers *et al.* (2005)

developed an off-axis cavity ringdown instrument using a continuous-wave laser as the source and a mechanical chopper to generate ringdown signals. Kasyutich *et al.* (2002) applied the off-axis continuous-wave CEA technique for measurement of NO_3 , although primarily for laboratory kinetic studies. Another recent innovation is to acquire the NO_3 spectrum with a single broad laser pulse by broadband cavity ringdown spectroscopy (Ball *et al.*, 2001). In addition, while not cavity related, the laser induced fluorescence technique has been applied to detection of NO_3 and N_2O_5 (Wood *et al.*, 2003, Matsumoto *et al.*, 2005).

1.10 The Nitrate Radical, NO_3

The nitrate radical, NO_3 , was first detected in the troposphere by Platt *et al.* (1980) by Differential Optical Absorption Spectroscopy, DOAS. This discovery has led to a great deal of research on the role of NO_3 in the atmosphere. Due to its high photolysis rate, NO_3 chemistry is restricted to primarily nighttime where it is a key oxidizing agent and plays a role similar to that of the hydroxyl radical, OH, an important daytime oxidizing species.

Until recently, NO_3 has most commonly been measured by DOAS. Observed concentrations of NO_3 vary widely depending on the region. For heavily polluted areas, peak concentrations can reach the hundreds of ppt, whereas for moderately polluted regions the peak concentrations can vary from between <1 ppt (Platt *et al.*, 1980) and tens

of ppt. For example, under the highly polluted conditions of Los Angeles, the maximum observed NO_3 was 355 ppt (Platt *et al.*, 1980).

A summary of the NO_3 chemistry in the atmosphere is given in Figure 1-3.

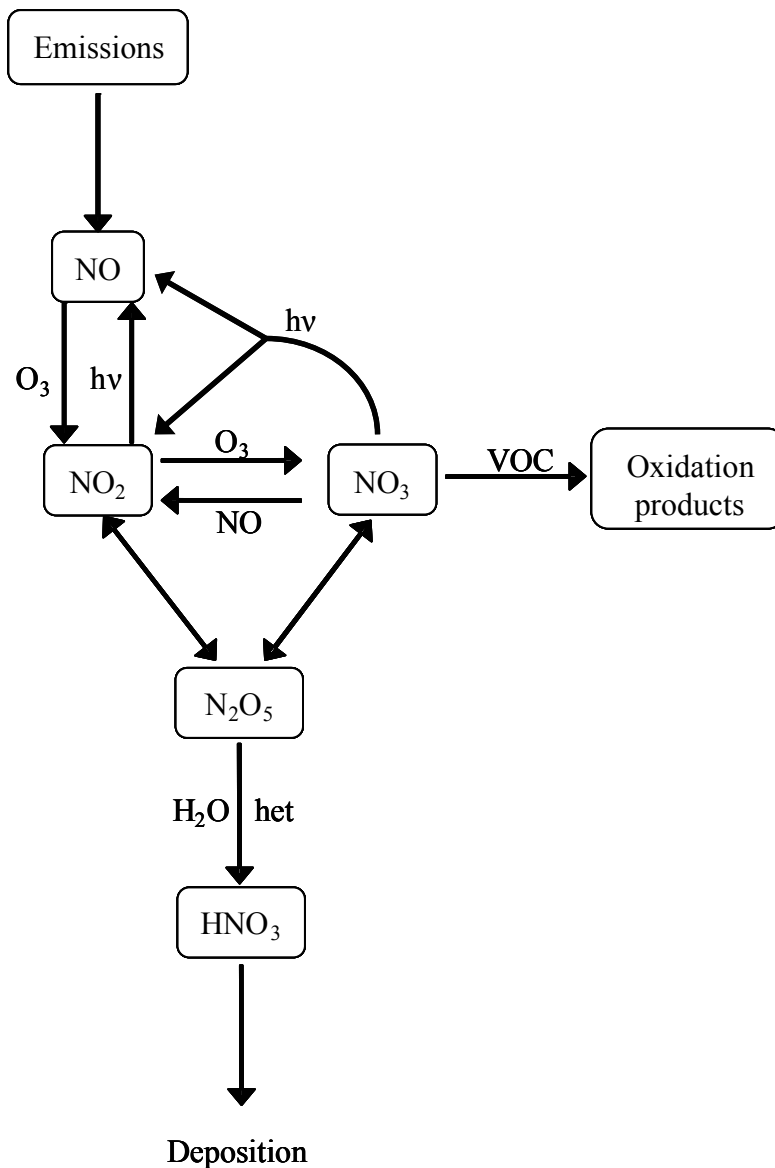
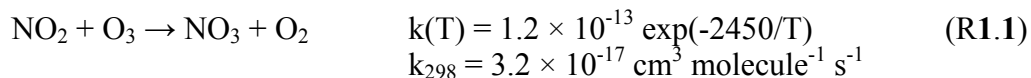
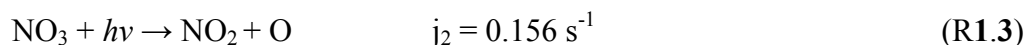


Figure 1-3 Summary of relevant atmospheric reactions involving NO_3

The primary tropospheric source of NO₃ is the relatively slow reaction between O₃ and NO₂ (Note: all kinetic data from Sander *et al.* (2006) unless otherwise indicated):

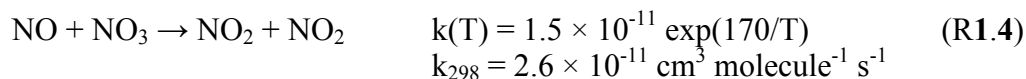


During the daytime, for overhead sun at the Earth's surface, NO₃ photolyzes rapidly at wavelengths below 640 nm (Johnston *et al.*, 1996) by two channels:

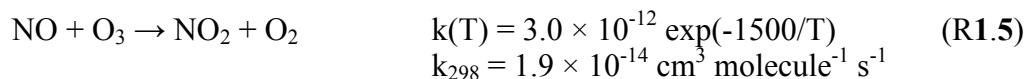


Therefore, the photolytic lifetime of NO₃ during the day is on the order of a few seconds.

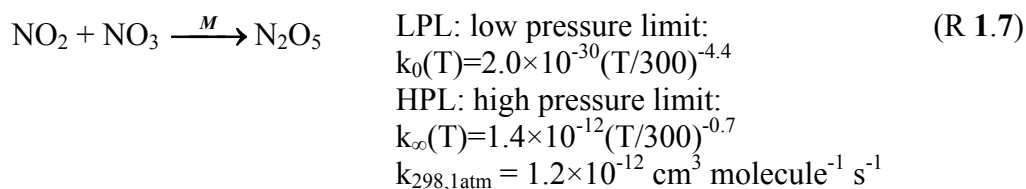
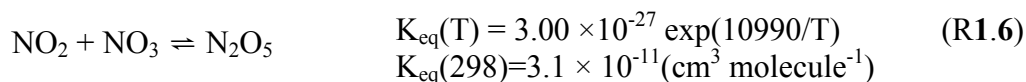
The main NO₃ chemical loss reaction is titration with NO:



NO also reacts with O₃:



The nitrate radical can also be stored via the formation of the reservoir species, N₂O₅:

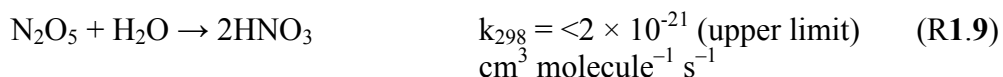


N₂O₅ acts as a reservoir species for NO_x and NO₃, and under certain atmospheric conditions has a lifetime long enough to be a source of odd-nitrogen in more rural

locations by transport. However, the reservoir species N_2O_5 can also act as an irreversible mechanism for NO_3 removal via the heterogeneous reaction of N_2O_5 with liquid water in cloud droplets or on aerosols to form HNO_3 (Mozurkewich and Calvert, 1988; Hu and Abbatt, 1997).

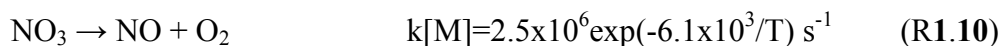


Compared to the heterogeneous reaction, the analogous gas phase reaction of N_2O_5 with water vapour is too slow to be of significance in the atmosphere:



The above reaction is shown as an upper limit due to the difficulties with distinguishing the homogeneous reaction from the heterogeneous reaction at high relative humidities.

Thermal unimolecular decomposition of NO_3 has been suggested (Johnston *et al.*, 1986; Davidson *et al.*, 1990) based on a review of previous laboratory experiments:



This rate constant for NO_3 thermal decomposition predicts significantly lower NO_3 concentrations than those observed in ambient studies (Russell *et al.*, 1986; Platt and Heintz, 1994). The loss attributed to the thermal decomposition of NO_3 was likely in fact due to the humidity dependent heterogeneous reaction of N_2O_5 with liquid water (Russell *et al.*, 1986; Platt and Heintz, 1994).

A key characteristic of NO_3 is its nighttime role as an oxidizing agent of volatile organic carbon (VOC) species. The rate constants for reaction of VOC oxidation by NO_3 are typically a few orders of magnitude lower than oxidation by OH. NO_3 concentrations

can potentially reach hundreds of ppt making the rates of the VOC – NO₃ reactions comparable to that of VOC – OH. The products of oxidation with NO₃ differ from OH oxidation as the products of NO₃ oxidation typically contain nitrate functional groups. Biogenic VOCs, such as isoprene, and the monoterpenes are quite reactive to NO₃ oxidation due to the presence of double bonds.

The concentration of nighttime NO₃ can be highly variable and is dependent on many factors. During the daytime, NO from direct emission sources is converted to NO₂ by O₃ mainly via reaction (R1.5). NO₃ formed by reaction of NO₂ and O₃, reaction (R1.1), is rapidly photolyzed during the day (R1.2), (R1.3) and reacts with NO (R1.4). Near sunset, NO₃ gradually increases in the absence of photolysis. As photolytic production of O₃ no longer occurs at night, fresh NO emissions react to remove O₃ (R1.5). As the O₃ decreases, the rate of formation of NO₃ by reaction (R1.1) decreases while the available NO reacts rapidly with NO₃ (R1.4), thus causing the NO₃ concentration to decrease. NO₃ is also in equilibrium with N₂O₅ (R1.6). Under conditions of high relative humidity, N₂O₅, and thus NO₃ (and thus NO_x), is removed irreversibly by reaction with liquid water to form HNO₃ (R1.8). The concentration of NO₃ is therefore highly dependent on many factors, most importantly, O₃, NO₂, temperature and relative humidity, and the proximity to direct emissions of NO. NO₃ will thus likely be highest in polluted air, with high NO₂ and O₃, but far enough away from direct NO emission sources so that the air mass has had time to process the NO emissions to NO₂.

1.11 Research Objectives

Resonant cavity spectroscopic techniques such as CRD and CEA/ICOS hold great promise for the detection of trace gases in the atmosphere due to the high sensitivity offered, as well as the potential for compact instrumentation. The goal of this research was to investigate the various cavity techniques, particularly CEA/ICOS and CRD, with the ultimate aim of developing an instrument capable of ambient measurements in the field.

As with any spectroscopic technique, the sensitivity is dependent on the absorption line strengths of the molecule of interest as well as the pathlength. The pathlength for resonant cavity techniques is dependent on the mirror reflectivity and separation. The absorption strengths of the molecules are strongly dependent the type of transition (vibronic, fundamental or overtone vibrational). Thus, the sensitivity of the techniques is strongly influenced by the wavelength region examined.

Due to the availability of highly reflective mirrors and instrumentation, resonant cavity techniques were investigated in the near-IR and visible regions. In the near-IR, CO, CO₂ and NH₃ were explored using CEA. With the recent availability of a compact, tunable diode laser at 662 nm, the instrumentation was adapted for use in the visible region. The extension of this study into the visible region also provided more insight into the techniques since the cavity effects were visible to the naked eye, also increasing the ease of alignment. The measurement of NO₃ in the visible region was the obvious choice due to its strong absorption in the red region of the spectrum, 662 nm. The

instrumentation was adapted for portability for ambient measurements at York University. The results and implications of field measurements here at York University in the summer of 2007 are discussed.

2 CAVITY ENHANCED ABSORPTION SPECTROSCOPY

2.1 *Near-Infrared CEA Spectroscopy*

2.1.1 FTIR and HITRAN Spectra in the Near-IR

The near-IR region, particularly around the 1550 nm region of the spectrum is an excellent candidate for the cavity enhanced absorption technique. Being a key region for the telecommunications industry, instrumental components are readily available. Several chemical species have absorption bands in this wavelength region, such as NH₃ (1470 – 1540 nm), H₂S (1560 – 1620 nm), C₂H₂ (1510 – 1540 nm), CO (1560 – 1600 nm), CO₂ (1565 – 1590 nm), and CH₄ (1630 – 1700 nm) with various absorption strengths. Figure 2-1 shows the various absorption line wavelengths for these species. The spectra for CO and CO₂ were obtained from the HITRAN database (Rothman *et al.*, 2004), while the remainder of the species spectra were obtained from the FTIR spectra of these gases.

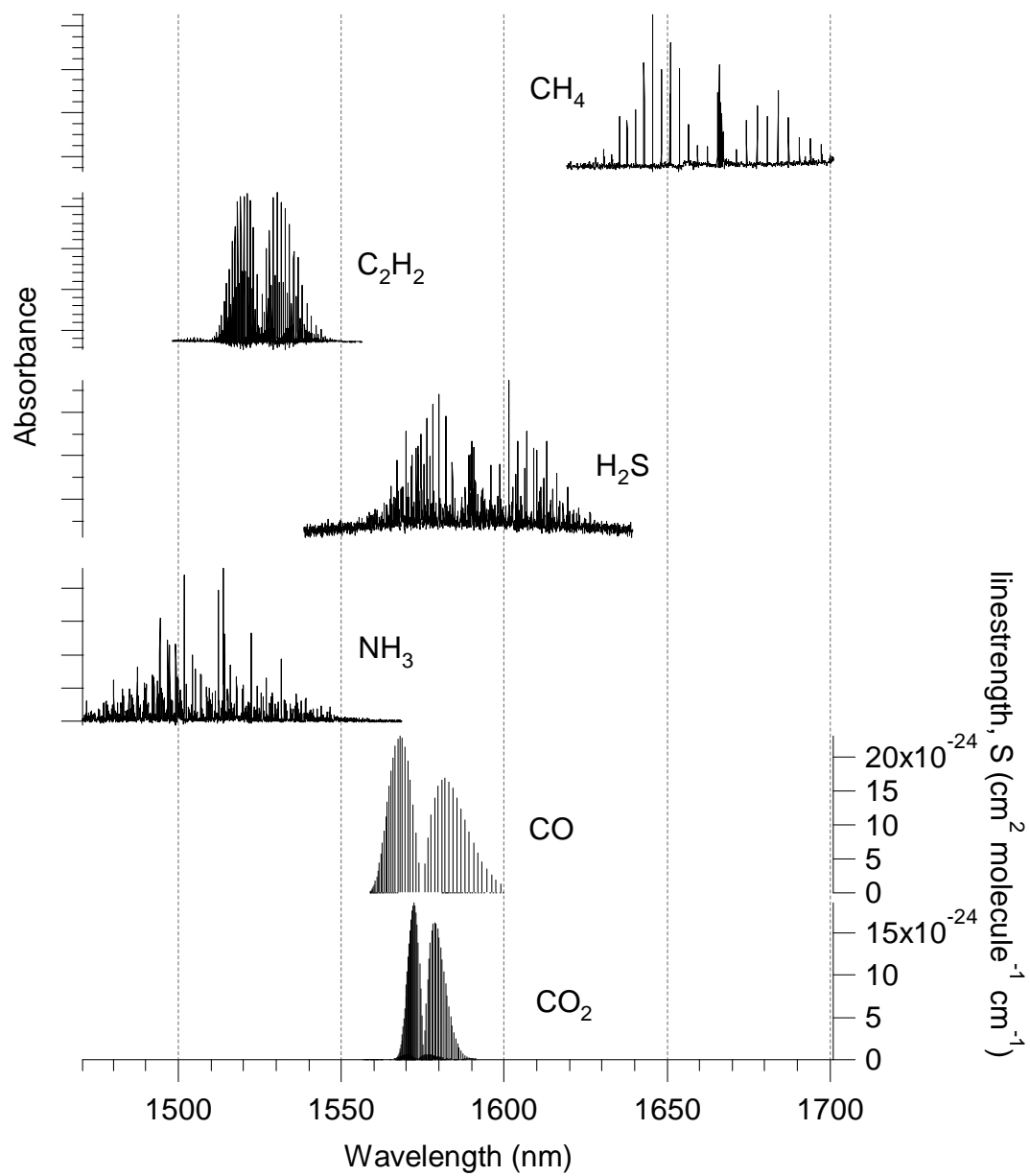


Figure 2-1 HITRAN linestrengths and FTIR spectra of various species in the near-IR

2.1.2 Characterization of Near-IR Lasers

The original aim of this research project was the implementation of a highly advanced, widely tunable diode laser in the near-IR in a commercially available spectrometer, a LasIR, manufactured by Unisearch. This SG-DBR laser (Sampled Grating - Distributed Bragg Reflectance) manufactured by GE Marconi, could be tuned almost continually from approximately 1490 to 1565 nm, by controlling the current of 4 separate sections of the diode chip. In a conventional TDLAS experiment, a separate laser is required for each species, or wavelength range, monitored. This widely tunable behaviour of the SG-DBR is desirable since multispecies monitoring can be performed with one laser. The intention was to utilize this laser as the source for the near-IR cavity enhanced absorption experiments with the LasIR instrument as the laser controller. Unfortunately, after a lengthy period of instrumentation modifications and a short period of testing, the SG-DBR laser failed permanently. The company manufacturing the laser was purchased by another company and support for this laser was discontinued. Research in the CEA technique continued in the near-IR using conventional DFB (Distributed FeedBack) tunable diode lasers.

Carbon dioxide was used for proof-of-principle type experiments in the near-IR since it is safe to handle, easy to sample, and has a well-characterized absorption band in the near-IR. Figure 2-1 shows the linestrengths, S , of the CO₂ band from the HITRAN database (Rothman *et al.*, 2004). Ammonia, NH₃, an important trace gas due to its negative impact on human health and the environment, was also investigated. As the

main basic gas in the atmosphere, ammonia is an important species as it reacts to neutralize sulfuric and nitric acids on wet aerosols (Harrison and Abdul-Massih, 1992). Ammonia is a notoriously difficult molecule to sample as it adsorbs onto surfaces rather easily (Yokelson *et al.*, 2003). Typical ambient ammonia mixing ratios are in the range of 0.1 to 10 ppb (Seinfeld and Pandis, 1998)

A DFB laser (Mitsubishi, ML925B22F) was chosen for the measurement of CO₂, with a specified tuning range of 1567 to 1573 nm. Characterization of the laser included the determination of the output wavelength as a function of laser temperature and current using a Bruker IFS 66v FTIR. The result is shown in Figure 2-2 superimposed on the accessible CO₂ lines. The characterization indicates that the strongest lines accessible to the laser are at 1570.543 nm ($S = 1.21 \times 10^{-23} \text{ cm}^{-1}/(\text{molecule cm}^{-2})$) and 1570.824 nm ($S = 1.37 \times 10^{-23} \text{ cm}^{-1}/(\text{molecule cm}^{-2})$).

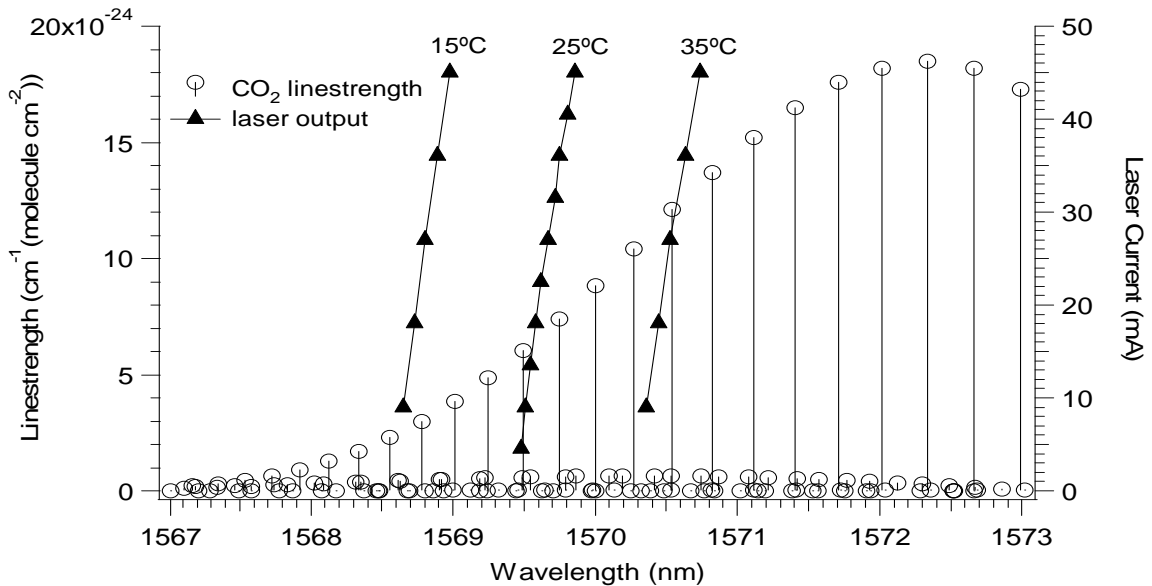


Figure 2-2 Laser emission wavelength as a function of laser current and temperature with HITRAN line positions and line strengths

To measure NH₃, a second DFB laser (Mitsubishi, ML, ML925B11F) was required to access the wavelength range of 1507 to 1513 nm. Figure 2-3 shows the tuning range of the laser for NH₃, superimposed on the absorption spectrum of NH₃ (Lundsberg-Neilson *et al.*, 1993) and the HITRAN spectrum of H₂O (Rothman *et al.*, 2004) which can have significant absorption in this spectral region. Although not shown in Figure 2-2, the absorption lines near 1514 nm could be accessed by increasing the laser temperature to 56°C. Unfortunately, there is little spectroscopic data available for this NH₃ band (Lundsberg-Neilson *et al.*, 1993; Webber *et al.*, 2001). The absorption cross-section was thus measured from the direct absorption spectrum of a 14 cm cell containing 6.4 Torr NH₃ in 230 Torr N₂ (Figure 2-4). From the figure, the maximum absorption is approximately 25% for the 1513.86 nm feature. This yields an absorption cross-section, σ , of $9.9 \times 10^{-20} \text{ cm}^2 \text{ molecule}^{-1}$, 500 times stronger than the CO₂ absorption cross-section at 1570.80 nm. The absorption feature at 1513.86 nm was used for CEA detection of NH₃ in the near-IR

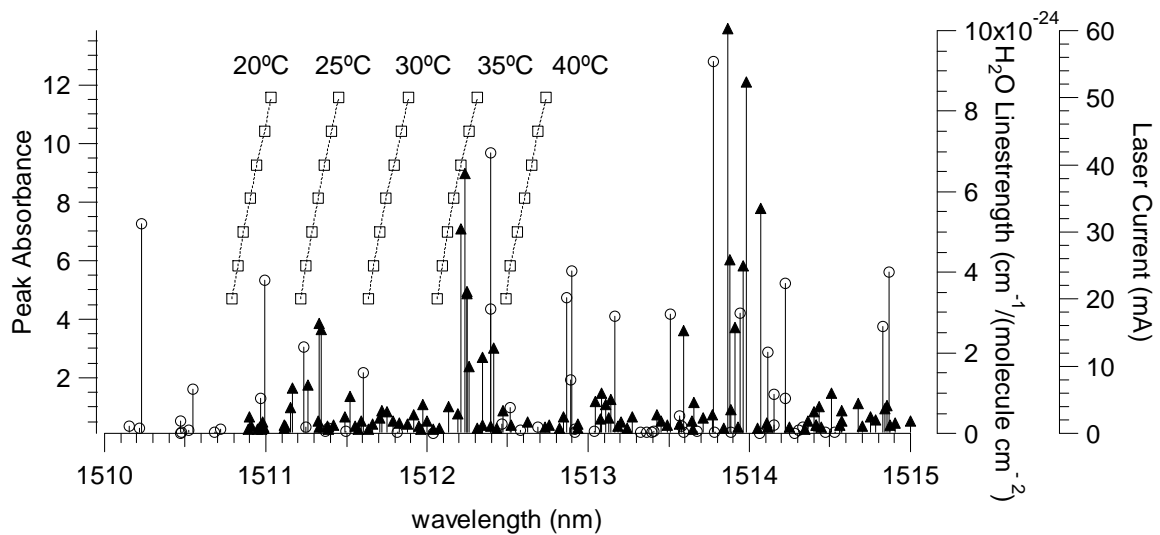


Figure 2-3 Laser output wavelength as a function of laser temperature and current (squares) with respect to the NH₃ absorption spectrum (Lundsberg-Nielsen et al. 1993) (triangles) and H₂O linestrengths (circles)

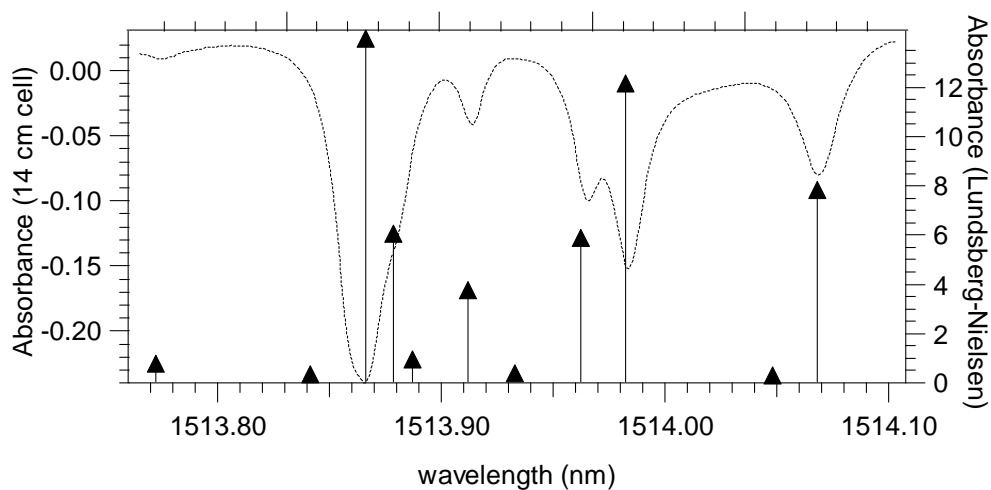


Figure 2-4 Direct laser absorption of 6.4 Torr NH₃ in 230 Torr N₂ in a 14 cm cell (dotted curve) and reference absorption spectrum (triangles Lundsberg-Nielsen et al., 1993))

2.1.3 CEA Instrument Design in the Near-IR

2.1.3.1 *Optical Setup in the Near-IR*

The DFB laser for CO₂ was installed in a laser diode mount (Thorlabs, TCLDM9) with various collimating lenses. Control of the laser was provided initially by an OEM laser diode temperature and current controller (Melles Griot, 56DLD403), and eventually replaced by a separate laser current controller (Thorlabs, LDC 202) and temperature controller (Melles Griot, 06 DTC 101). No mode-matching optics were used in the near-IR.

The resonance cavity was constructed out of stainless steel at various lengths (10, 50, 75, and 100 cm), with TEM₀₀ free spectral ranges of 1500, 300, 200, and 150 MHz, respectively. A gas inlet and an outlet were positioned near the two ends of the cavity. The cavity was mounted on vertical and transverse translation stages to allow for off-axis alignments.

Due to the high reflectivity required for long effective pathlengths, mirrors are manufactured specifically for the wavelength of interest. The highly reflective mirrors (0.8" diameter, 6 m radius of curvature, Los Gatos Research, Inc., $R > 99.99\%$ at 1570 nm) were installed in the mounts provided (Los Gatos Research, Inc.). A second set of highly reflective mirrors was used in later experiments for NH₃. These had a 1" diameter and 1 m radius curvature and the cavity mounts were modified to fit these mirrors. These mirrors had a specified reflectivity of approximately 99.993% at 1515 nm. The manufacturer supplied reflectivity curve is shown in Figure 2-5.

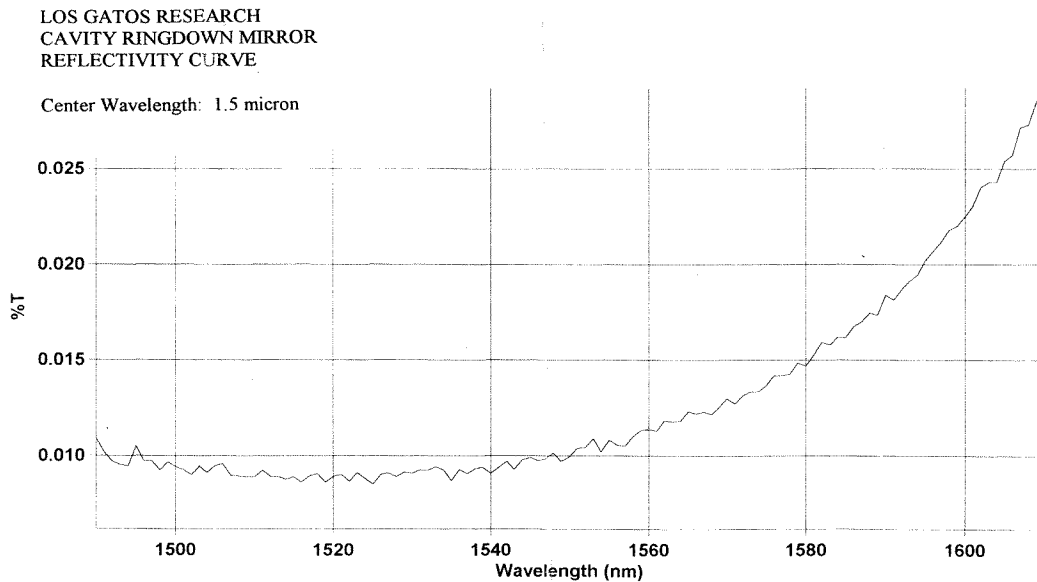


Figure 2-5 Manufacturer specified reflectivity curve of second set of highly reflective mirrors in the near-IR. The y-axis, %T, is equivalent to 100%-R (reflectivity)

The highly reflective mirrors were installed in the mount on an o-ring and brass retaining ring. The cavity was sealed directly on the mirror – o-ring connection. Three micrometer screws provided fine adjustment control of the highly reflective mirror alignment. One of the micrometer screws contained the piezo-electric transducer, PZT, (Thorlabs, 06 DTC 101). The cavity mount was attached to the stainless steel cavity cell and sealed with an o-ring with the mount containing the PZT located at the cavity entrance. The cavity assembly was attached to the breadboard by two posts located adjacent to the cavity tube ends.

A detector assembly (Los Gatos Research, Inc.), consisting of an InGaAs photodiode and a lens, matched to the mirror mount was installed in the exit mirror

mount to collect the cavity output. The optical bench configuration is shown in Figure 2-6.

A reference spectrum was required in several experiments so a small portion of the beam was reflected from a window to a reference cell to another detector (not shown in Figure 2-6).

2.1.3.2 Gas Sampling System for the Near-IR

The gas handling system for the near-IR was fairly straightforward and was included in Figure 2-6. For the CO₂ experiments, variable mixing ratios of CO₂ in N₂ were produced by dilution of a cylinder mixture of 210 ppm CO₂ in N₂ (BOC) into another N₂ flow. Higher CO₂ concentrations in air were obtained by sampling laboratory air or air sampled from exhaled breath when required. Cavity flow rates varied from roughly 500 to 1000 sccm and were controlled with a 1000 sccm mass flow controller (MFC).

The gas sample was introduced to the cavity at 90° to the cavity axis and flowed through the cavity and was removed via a pressure controlled vacuum pump. A needle valve was placed at the cavity outlet before the vacuum pump in order to restrict the flow to the pump and allow the cavity sample to be at the desired reduced pressure. The cavity pressure was monitored with a 1000 Torr pressure gauge (MKS Baratron).

For experiments with NH₃ as the test gas, the CO₂ calibration source was replaced with an NH₃ calibration mixture cylinder (10 ppm NH₃ in N₂, BOC) and all sample tubing lengths were minimized.

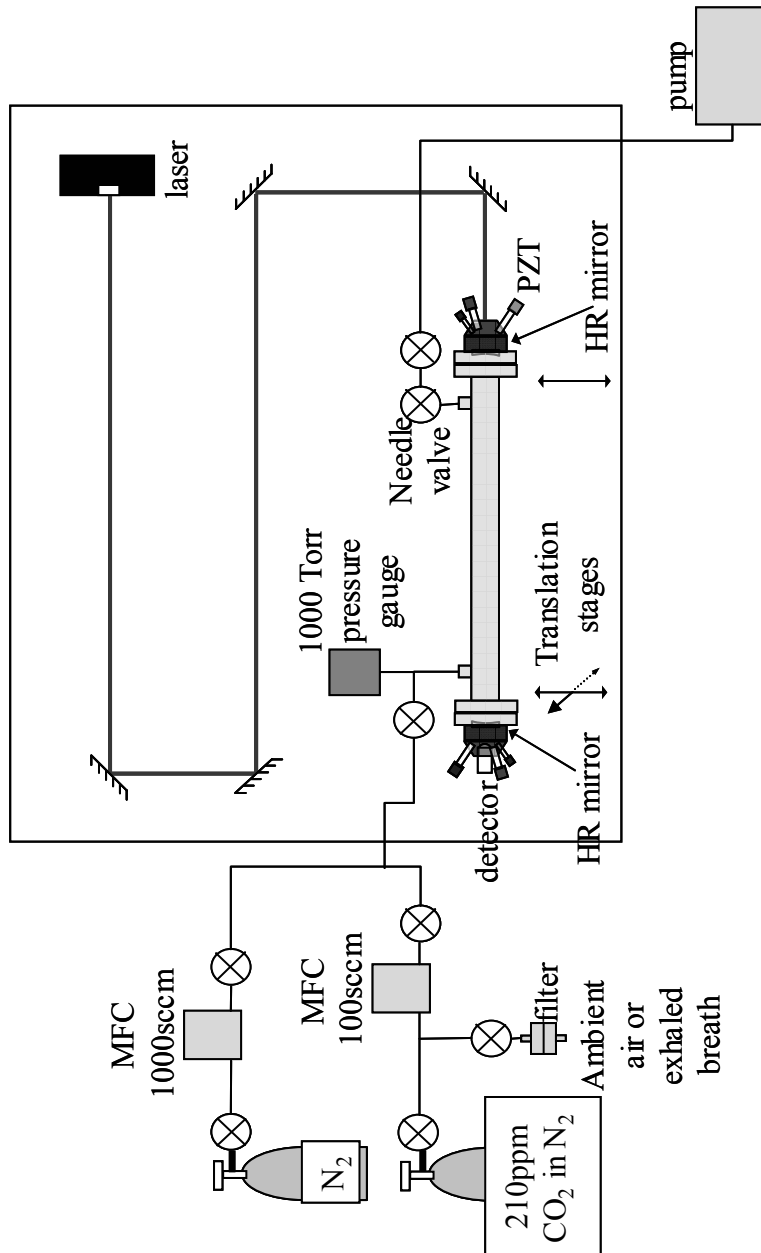


Figure 2-6 *Optical setup and gas sampling system for CEA experiments in the near-IR*

2.1.3.3 Electronic Setup for Near-IR Cavity Enhanced Absorption Experiments

The electronic setup for the CEA experiments is shown in Figure 2-7. To provide wavelength scanning of the laser, a voltage ramp was supplied from an analog output channel of the data acquisition board housed in the computer. This ramp voltage was sent to a variable voltage divider for control of the ramp amplitude and then combined with a triangle waveform voltage from a function generator (Hameg 8030) to provide modulation of the laser wavelength. The combined signal was sent to the modulation input of the laser current controller.

The piezo-electric transducer was powered by a single-channel PZT power supply (Thorlabs, MDT694). Modulation of the PZT was provided by a triangle waveform voltage from a second function generator (Hameg HM 8030). Both the frequency and amplitude of the PZT and laser wavelength modulation were adjustable.

The detector signal was sent to a large dynamic range amplifier (Melles Griot, 13 AMP 003), the output of which was split to a storage oscilloscope (Tektronix 2211) for visual feedback of the cavity output and to the integrator circuit which was adjusted for further gain control. The integrator circuit was triggered by the digital sync out (0, +5V) output from the data acquisition board. The signal from the integrator was split to the oscilloscope and to the I/O interface for a computer mounted data acquisition board. The acquisition board and computer were used for prior tunable diode laser experiments using the TAMS (Trace Atmospheric Monitoring System) instrument in the laboratory. The program, written in C++, was modified for control of the integrator. The

I/O board interface provided the ± 2.5 V ramp in 128 voltage steps for control of the laser ramp. The duration of each ramp step could be altered by the user to allow for different integration times.

For later experiments in the near-IR and visible, the acquisition system was replaced. A computer running Windows XP was purchased along with a new data acquisition board, (National Instruments, NI6026E), as well as an interface for I/O (National Instruments, BNC-2110). New software was written using Labview for Windows. The program was thus readily customizable for the various resonant optical cavity absorption spectroscopy analogs.

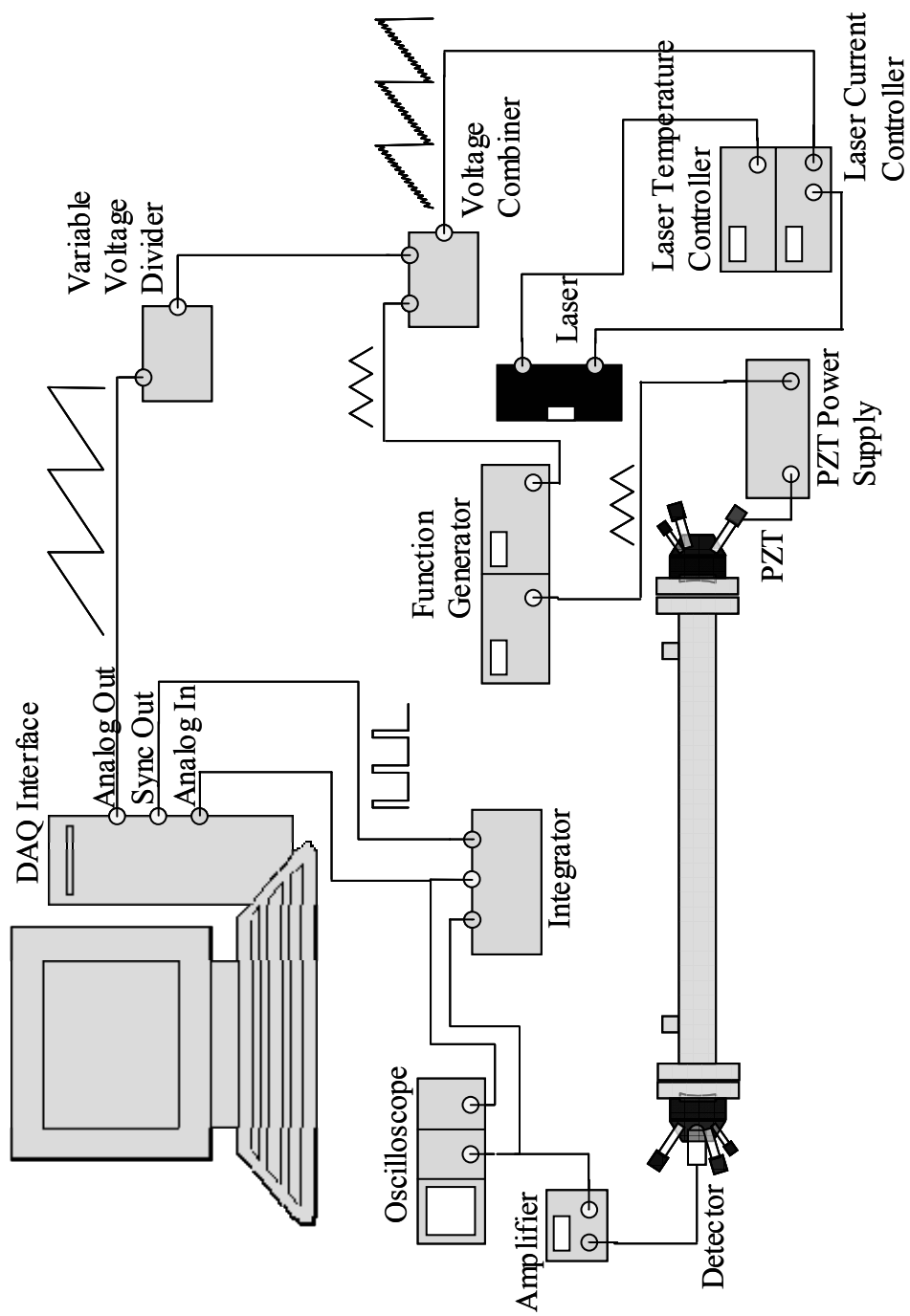


Figure 2-7 Electronic setup for CEA experiments

2.1.3.4 *The Integrator Circuit*

In order to reduce the variability in the detected signal due to the cavity resonance conditions, the detected signal was time-integrated to ensure a relatively flat detected signal.

The integrator circuit is based on a common RC op-amp circuit, Figure 2-8. When the capacitor bypass switch is open, charge builds up on the capacitor proportional to the time integral of the incoming voltage until either saturation occurs or the integrator is reset. The output voltage, V_{out} , is related to the time integral of the input voltage, V_{in} , by (Simpson, 1987):

$$V_{out} = \frac{-1}{RC} \int V_{in} dt \quad (\text{E2.1})$$

where R and C are the resistance and capacitance, respectively.

A circuit board was designed and printed, with an IC switch controlling the capacitor bypass (Motorola MC14016B, not shown in the figure). The components were mounted in a box with switches for varying the resistor and capacitor values and BNC receptacles for I/O. The ± 15 V power to the circuit was provided from either batteries or a separate power supply.

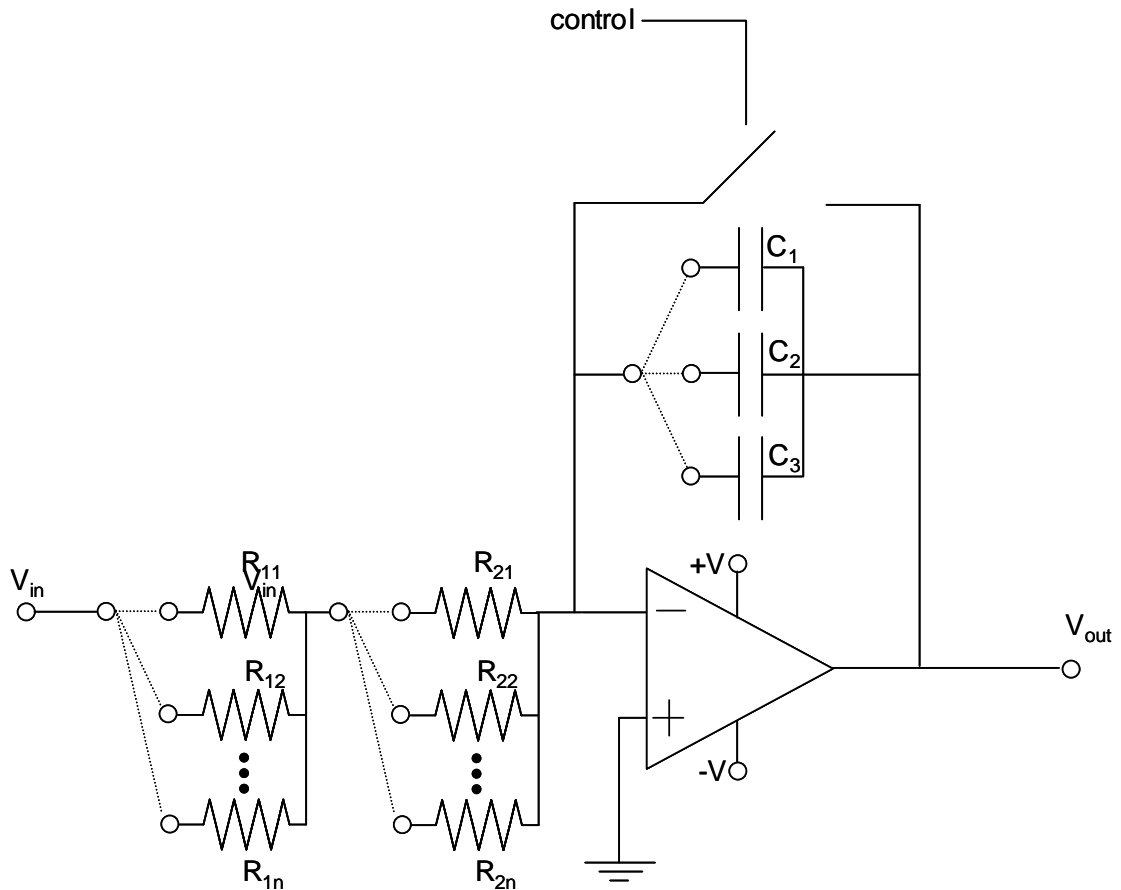


Figure 2-8 Schematic of op-amp integrator circuit. The gain could be controlled by varying the combination of resistors (R) and capacitors (C)

To allow for a wide range of input voltage and integration times, the circuit was designed with two user-selectable resistors in series, each with eight resistances to choose from, as well as selection of one of three capacitor values.

2.1.3.5 CEA Data Acquisition

The CEA experiment was originally performed with a modified version of the software and data acquisition hardware from another instrument in the laboratory (TAMS). It was found that the timing of the integrator triggering was inconsistent. In other words, the period the integrator was switched on was slightly different for each ramp step. This is evident in Figure 2-9, the acquired values of the integral of a DC signal for each step (channel) of one ramp, which ideally should be constant for the entire ramp.

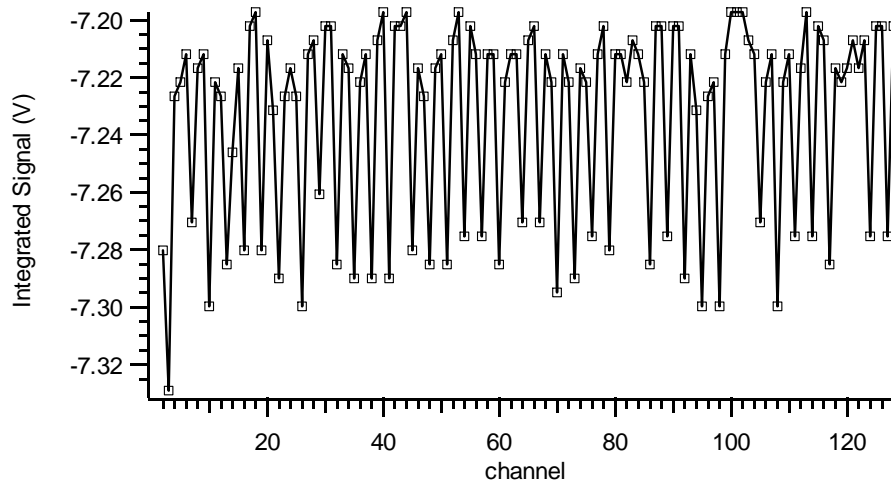


Figure 2-9 Integrated signal of a 40 mV DC signal from TAMS software and hardware showing inconsistent timing

It was decided at this point to upgrade the hardware and software. A new data acquisition board (National Instruments, NI6026E) was purchased as well as a new computer for controlling the experiment. A LabVIEW program was written to control

the laser ramp, trigger the integrator, and acquire and save the data. Creation of the program allowed maximum flexibility for the various modifications required.

By utilizing the built in general purpose counters of the acquisition board, very accurate and reproducible timing of the integrator switch was achieved. Figure 2-10 shows the schematic of the timing signals. The laser ramp was controlled from Analog Out0 of the board. The integrator switch was controlled by the gating counter Counter1. At the beginning of each ramp step (Analog0), the switch was closed for 1 ms to fully discharge the capacitor, and then opened. The voltage at the analog input (detector signal) was read according to Counter0, precisely 15.8 ms after the falling edge of the integrator reset (Counter1). The timing parameters were user-selectable, although for all experiments the values were maintained as shown in the figure. These timing values allow for a 2 second ramp of 128 channels or a 1 second ramp of 64 channels.

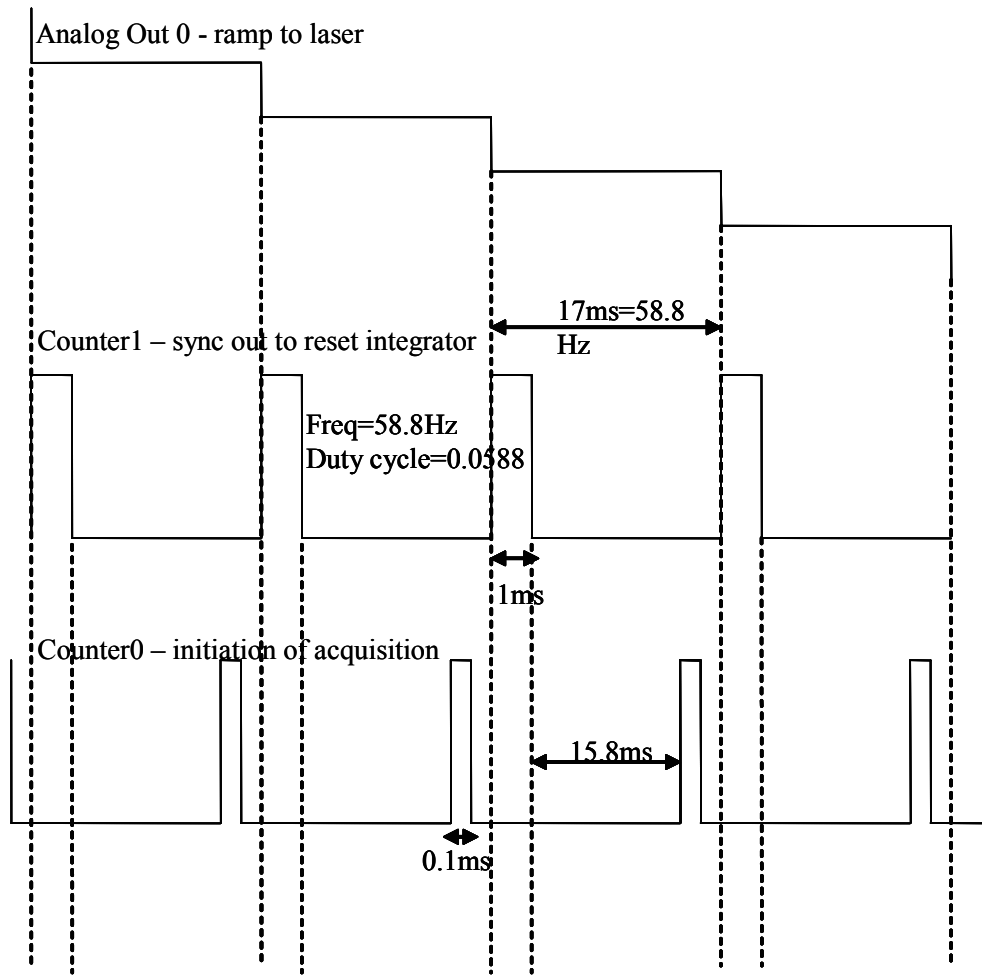


Figure 2-10 *Timing of counter and triggering scheme of new Labview program for accurate timing of integrator switch*

Figure 2-11 shows the result of the new setup for the integral of a 40 mV DC signal with the same integrator gain conditions. From Figure 2-11, it can be seen that the integrator timing problems have been solved; the integrator is switched on for the same length of time for each ramp step with the few outlying points representing the resolution of the data acquisition board.

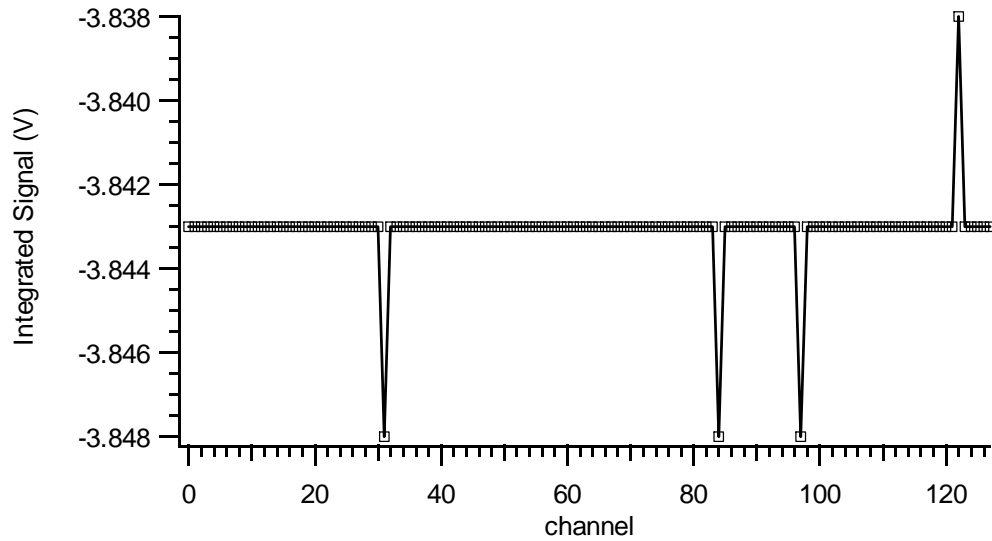


Figure 2-11 Integrated signal of a 40 mV DC signal from Labview software and new hardware showing consistent timing

The effect of integration of the cavity output is shown in Figure 2-12. From the figure it is readily evident that integration after a certain period of time dramatically decreases the variability in the signal. Hardware integration also eases the requirement for fast acquisition response times.

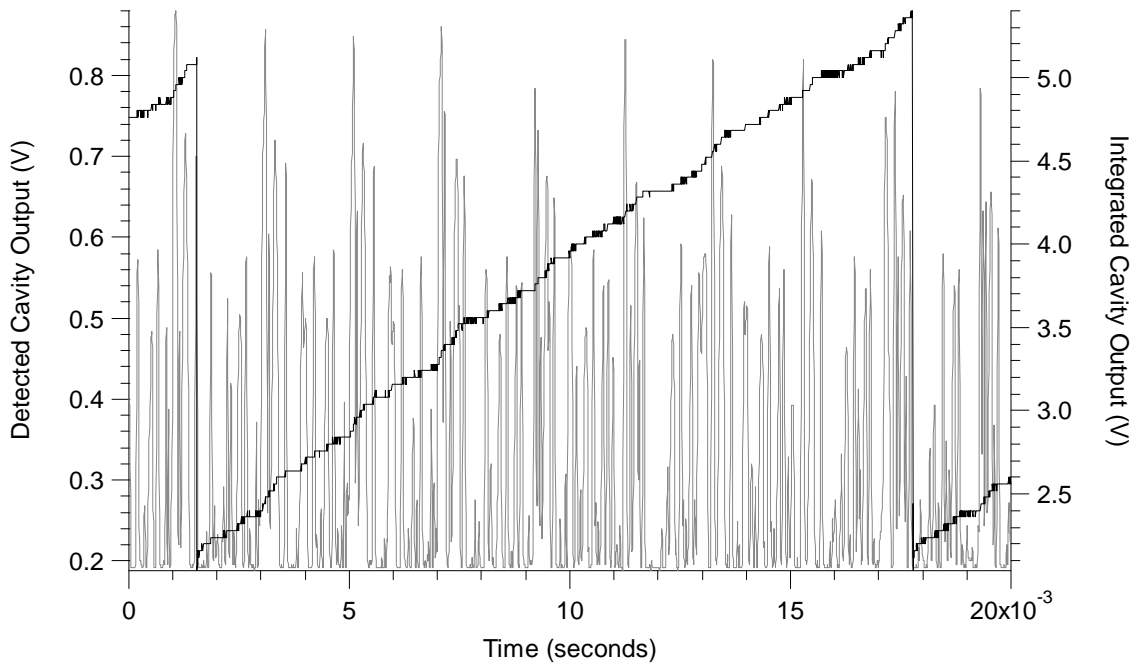


Figure 2-12 Example of integration (black line) of the actual cavity output (grey data)

2.1.4 Initial Setup and Alignment Procedure

Proper alignment of the resonant cavity was very important. Initial alignment required the removal of the cavity mirrors and the beam directed down the centre of the cavity. Since the near-IR beam was invisible to the naked eye, an IR-sensitive card was used during alignment. The exit mirror mount was then mounted and adjusted such that the back-reflection was located just slightly below the laser collimating lens on the laser mount. The cavity entrance mirror mount was then mounted to the cavity and the back-reflection was adjusted to the same position on the laser mount. A long optical path from the laser to the cavity was used to help minimize the back-reflection to the laser while

keeping the beam aligned as close to the cavity axis as possible. This procedure for the initial alignment of the optical system was similar for all iterations of this research.

2.1.5 Cavity Enhanced Absorption Measurements of CO₂

With the cavity setup in the on-axis configuration, the various parameters were investigated such as, PZT modulation frequency and amplitude, laser modulation frequency and amplitude, integration time and gain (by varying the resistor and capacitor), cavity sample pressure, and cavity alignment, to name a few. The parameters were qualitatively optimized and tests were performed on CO₂ gas samples.

2.1.5.1 Effect of Laser and Cavity Length Modulation On On-Axis CEA of CO₂

Initial tests showed a considerable amount of noise on the detected integrated cavity output as a function of wavelength. With the 75 cm cavity ($\nu_{fsr} = 300$ MHz), and the laser tuned to the 1569.494 nm line, the effect of laser modulation on the cavity output was investigated and the result is shown in Figure 2-13. The ramp consists of 128 wavelength steps and the cavity output of each ramp step is integrated for 16 ms to give a 2 second scan. The displacement on the PZT of 6.6 μm , a distance equivalent to roughly 8 free-spectral ranges, at a frequency of 300 Hz, cycles roughly 4.5 times per ramp step (ramp step length = 16 ms; PZT period = 3.3 ms). Figure 2-13 shows the 5 minute average spectra with no modulation (red curve) and with a 1 kHz laser modulation (62 cycles per ramp step, blue curve) applied with an amplitude of approximately 900 MHz

(3 free-spectral ranges). Without the modulation (red curve), the characteristic cavity output fringe pattern of 300 MHz is easily evident even after 5 minutes of averaging. The modulation has the effect of smearing the cavity output by ensuring that at each wavelength step there are many cavity modes excited.

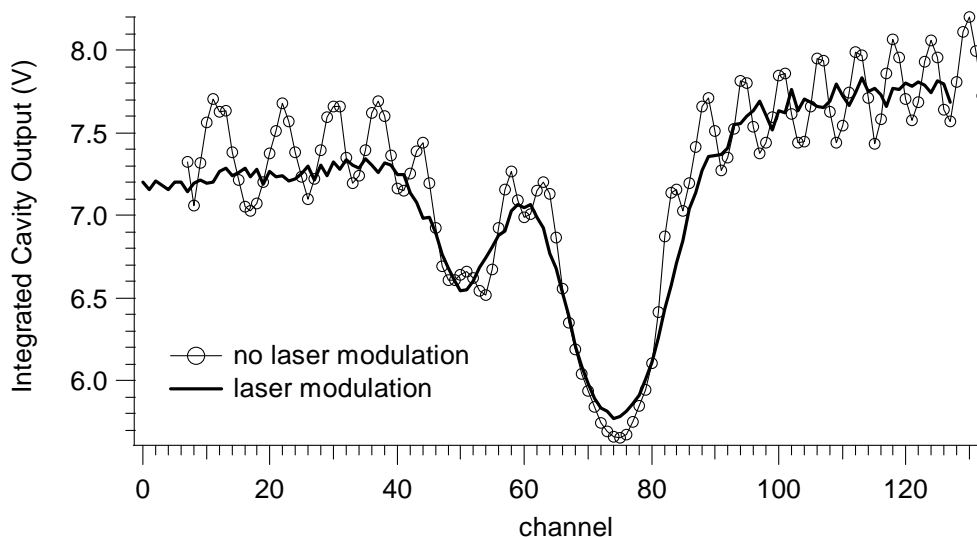


Figure 2-13 *Effect of frequency modulation on integrated cavity output of CO₂ near 1569.494 nm*

The slight upward slope of the baseline is due the increasing power of the laser as the applied current increases during the ramp. The laser output power and wavelength are dependent upon the current applied so the laser power is increasing across the ramp.

2.1.5.2 *Effect of Sample Pressure on Sensitivity*

The pressure sensitivity of the technique with various samples of CO₂ in air was investigated. Figure 2-14 shows the absorption signal of 1 Torr CO₂ in N₂ as a function

of total pressure for pressures ranging from 1 Torr to 500 Torr. In this case the concentration (molecules cm^{-3}) remains constant while the mixing ratio is varied. At low pressures, Doppler broadening dominates so the absorption lines are narrow. It is preferable to work at lower pressures since the lines are narrow offering better selectivity, thus reducing spectral interferences from other species. As the pressure increases, the absorption linewidth broadens with higher total pressure (pressure or collision broadening). When sampling ambient air at reduced pressure, the mixing ratio stays constant, although the concentration (molecules cm^{-3}) decreases with decreasing pressure. From the Beer-Lambert law, $A = \sigma L[X]$, the absorption strength is dependent on the concentration, $[X]$, and the absorption cross-section, σ . With decreasing pressure, the concentration decreases but σ increases as the linewidth decreases. This results in little loss in signal as the pressure is reduced to a pressure just above where Doppler broadening begins to dominate. Near this pressure, the absorption linewidth is narrow without sacrificing absorption strength. In addition, the signal-to-noise is optimum near this pressure. With knowledge of the linestrength of a typical CO_2 line in the region of the laser, α ($A/L = \sigma[X]$) can be determined by assuming a Voigt profile (the lineshape is a combination of both Doppler and collisional broadening (Brassington, 1995)) for the absorption lineshape. The calculated α (A/L) for 210 ppm of the 1570.80 nm line at line centre as a function of total pressure is shown in Figure 2-15.

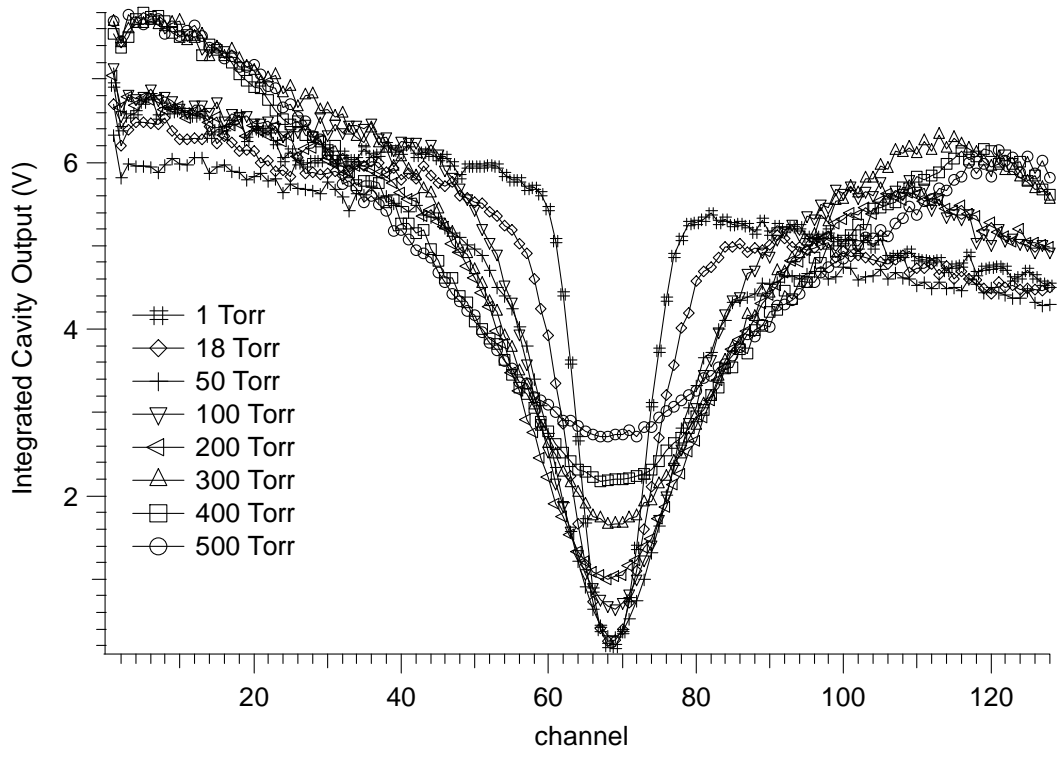


Figure 2-14 Effect of pressure on absorption linewidth for constant concentration (1 Torr CO₂ in variable N₂ total pressures)

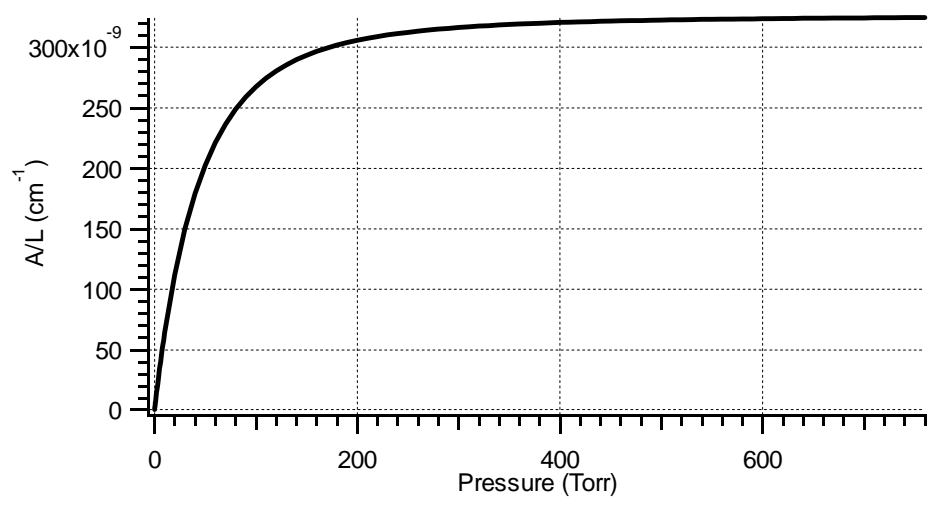


Figure 2-15 Absorption coefficient, $\alpha = A/L$ for 210 ppm CO₂ as a function of pressure for the absorption line at 1570.80 nm

Figure 2-15 shows that the detected optical density for CO₂ in air stays relatively constant from atmospheric pressure until approximately 200 Torr below which the optical density begins to decrease rapidly. Therefore, CO₂ samples can be pumped down to approximately 200 Torr for optimum sensitivity.

2.1.5.3 Detection Limits of CEA of CO₂

2.1.5.3.1 Instrument Stability Analysis: Allan Variance

The stability of the instrument was analyzed to determine the optimum averaging time for an actual measurement. In general, the signal to noise ratio increases as \sqrt{N} for N elements averaged. Therefore, longer or more signal averaging yields a better signal to noise. Unfortunately, in the case of tunable diode lasers, this \sqrt{N} dependence does not hold indefinitely. In a TDL absorption experiment, the laser and other experimental components experience drift, causing the signal to noise to decrease after a finite time. A useful method for quantifying this behaviour is by determining the Allan Variance (Werle *et al.*, 1993).

A summary of the Allan Variance procedure is the following. A data set containing N elements is divided into M subsets each containing k elements.

The average for each subset, $A_s(k)$, is calculated,

$$A_s(k) = \frac{1}{k} \sum_{l=1}^k x_{(s-1)k+l} \quad (\text{E2.2})$$

$$s = 1, \dots, m, \quad m = m' - 1$$

then the Allan Variance is calculated for a particular k group by the following:

$$\langle \sigma_A^2(k) \rangle_t = \frac{1}{2m} \sum_{s=1}^m [A_{s-1}(k) - A_s(k)]^2 \quad (\text{E2.3})$$

This procedure is repeated for different M and k values and the Allan Variance is then plotted as a function of k , which is directly related to the number of points in the average.

The Allan plot (Figure 2-16) was generated from a continuous flow of 105 ppm CO₂ in N₂ at 235 Torr. The laser was centred at 1570.80 nm CO₂ absorption line. Each ramp (wavelength scan) consisted of 128 wavelength steps, with each step lasting 17 ms (integration time of 15.8 ms per step) for a 2 second total scan time and averaged to 1 minute. Each 1 minute average was simultaneously fit to a background and calibration spectrum recorded earlier. The coefficient of this fit yields the concentration.

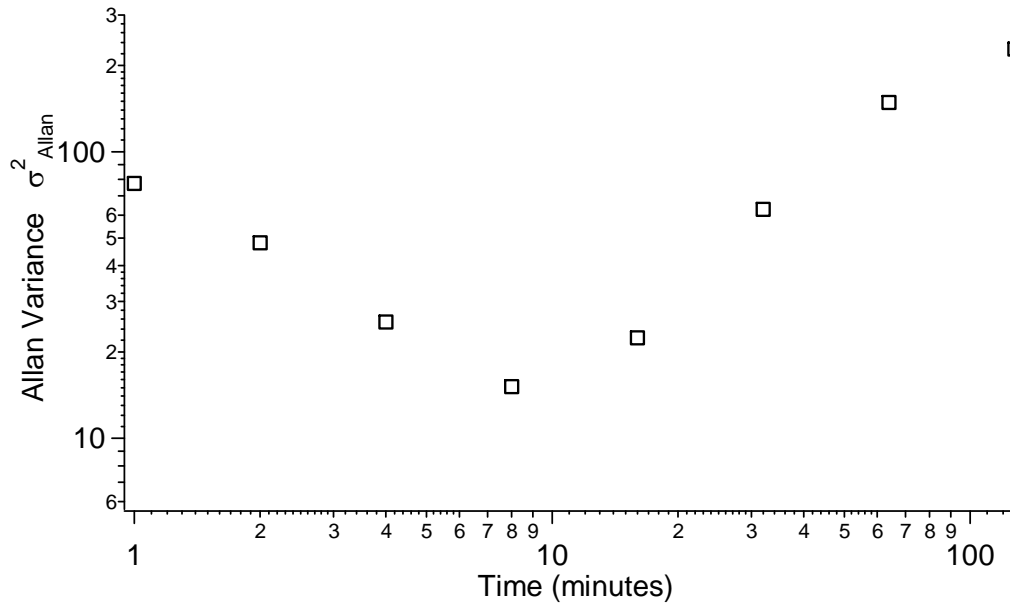


Figure 2-16 Allan plot for CEA experiment of 105 ppm CO₂

Figure 2-16 shows the Allan Variance for a sample experiment following the above procedure. This plot is a log-log plot of the Allan Variance as a function of k , the number of elements averaged. The minimum in this plot indicates the optimum number of elements in the average for best signal to noise. In this case, the optimum averaging time is approximately 10 minutes. This means that 10 minutes is the optimum total time to perform a measurement, including calibration, background acquisition, and any flushing required.

From the Allan plot, the minimum Allan variance, σ_A^2 , is 13.6 ppm². The 3σ detection limit, 3 times the square root of σ_A^2 , is 11.1 ppm. In terms of minimum detectable fractional absorbance, this detection limit is $1.65 \times 10^{-8} \text{ cm}^{-1}$, or 1.23×10^{-6} for the 75 cm cavity.

2.1.5.3.2 Cavity Enhanced Absorption Spectra of CO₂

Tests were performed in order to gain insight on the sensitivity of the technique. Figure 2-17 shows a series of 60 second ramp averages of 210 ppm CO₂ in air at 230 Torr total pressure. Each ramp was approximately 2 seconds long (approximately 16 ms per ramp step) therefore 30 ramps were averaged in 60 seconds. A background N₂ sample is also shown. Note also that the data has been smoothed via the Savitzky-Golay least-squares smoothing procedure (Savitzky and Golay, 1964). This removes the high frequency noise component but does not affect the low frequency component (although it makes it more obvious to the eye). These two sets of data show a problem that was often

encountered; the loss of signal power with time. As shown in the lower graph of Figure 2-17, the cavity alignment drifted over the acquisition time, in this case 10 minutes, causing lower throughput through the cavity and thus lower detected signal. Obviously, the cavity output is dependent on cavity alignment.

The upper graph of Figure 2-17, showing consistently stable alignment, contains enough information to estimate the pathlength of the instrument and the detection limit. The background subtracted spectrum is shown in Figure 2-18. Since α is known from Figure 2-15 for these conditions ($3.1 \times 10^{-7} \text{ cm}^{-1}$) and the estimated cavity enhanced signal, A , from Figure 2-18 is 7.1%, from the Beer-Lambert law this yields an effective pathlength of 2.4 km. In other words, an absorbance that is 2.325×10^{-5} in a 75 cm pathlength appears as an absorbance of 0.071, an enhancement of 3054 times.

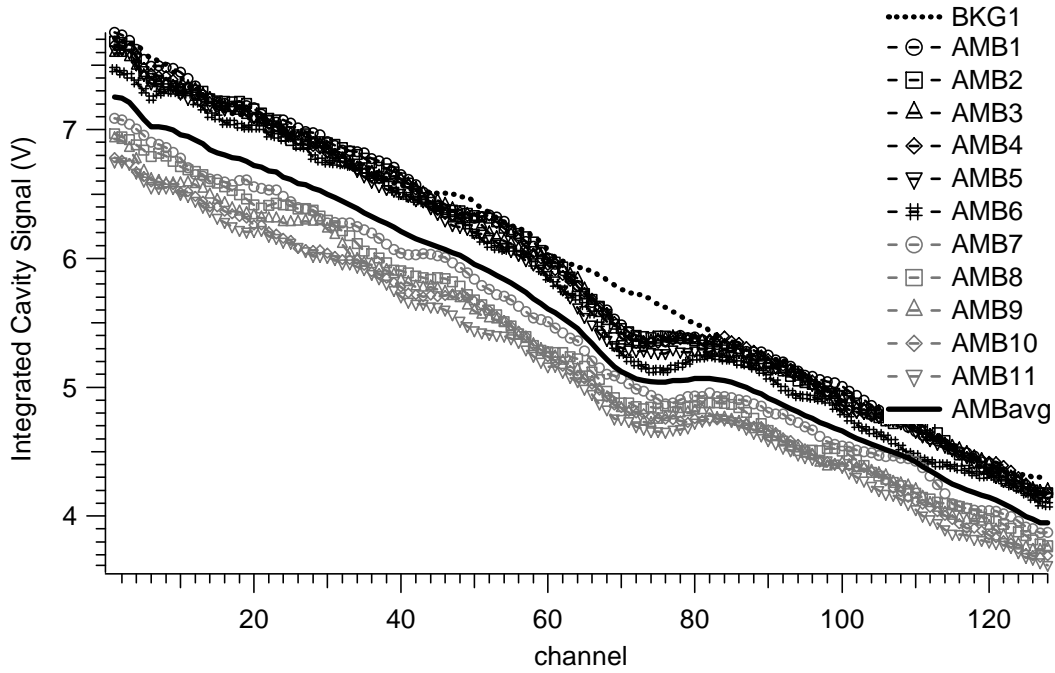
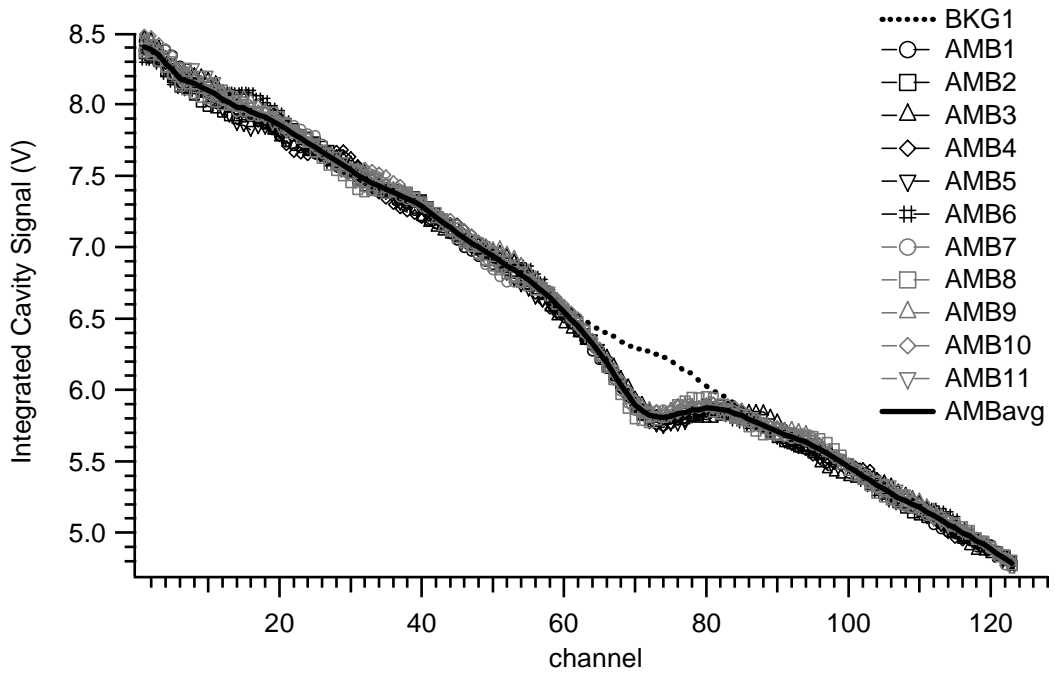


Figure 2-17 Continuous series of 60 second average CEA scans of 210 ppm CO₂ showing good stability (upper graph) and alignment drift (lower graph)

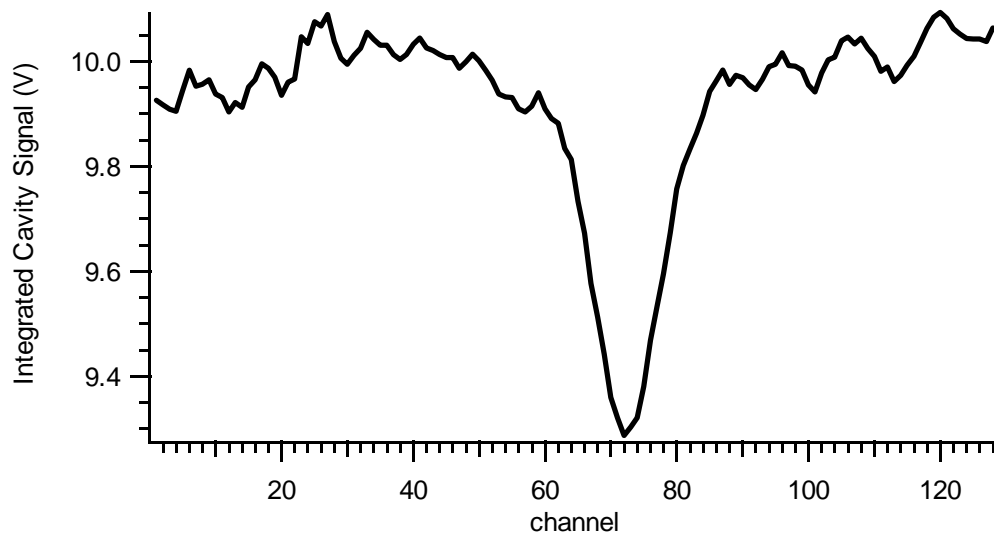


Figure 2-18 Background subtracted spectrum of upper spectrum of Figure 2-17

From the Figure 2-18, it appears that there is still some residual cavity mode structure evident in the detected signal. This is typically the limiting noise source in CEA experiments. The signal-to-noise ratio of this spectrum is 14. To estimate the 3σ detection limit, for a SNR of 3, the minimum detectable optical density is 1.5×10^{-2} for a 75 cm pathlength. Taking into account the enhancement factor, this is equivalent to a minimum detectable optical density of 5×10^{-6} , or a minimum detectable fractional absorbance of $6.6 \times 10^{-8} \text{ cm}^{-1}$. This is equivalent to a CO_2 mixing ratio of 45 ppm.

2.1.5.3.3 Spectra after Hardware and Software Modifications

A comparison of the results before and after the Labview software and hardware modifications is shown in Figure 2-19. All other conditions were identical. The figure shows a slight increase in the absorption strength of the run performed with the new

hardware and software. This was likely due to an increase in the pathlength as the mirrors had been recently cleaned. Following a similar analysis as that in section 2.1.5.3.2, the effective pathlength was 3.03 km, and the minimum detectable optical density was $4.65 \times 10^{-8} \text{ cm}^{-1}$. This is equivalent to a CO_2 mixing ratio of 31 ppm. It appears from this figure that the residual cavity mode signal has also been minimized.

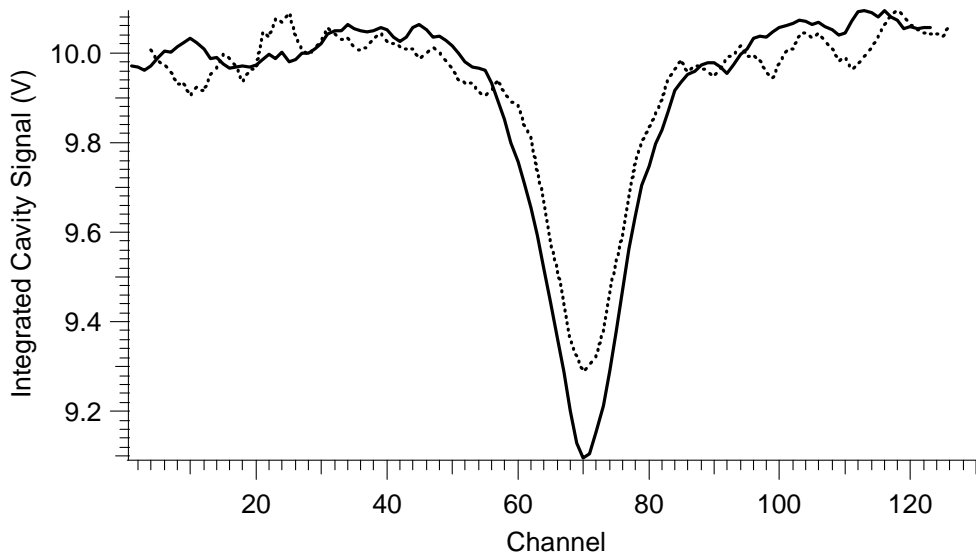


Figure 2-19 CEA of CO_2 with background subtraction for old TAMS software (dotted curve) and new Labview software and hardware (solid curve)

2.1.6 Near-IR Cavity Enhanced Absorption of NH_3

The second set of new highly reflective mirrors was used for the NH_3 cavity experiments ($R \sim 99.993\%$ at 1515 nm). The 10 ppm calibration cylinder was diluted to various concentrations and experiments similar to the CO_2 experiment were performed. Figure 2-20 below shows the integrated cavity output for 361 ppb NH_3 at 250 Torr of the

1513.86 nm absorption line. This yields an effective pathlength of 3.0 km from the 75 cm cavity. Figure 2-20 also shows the result of the difference between two consecutive backgrounds, with the cavity filled with N₂. The 3σ standard deviation of this bkg-bkg is 1.1%. This means the minimum detectable optical density is 1.1% for a 3.0 km pathlength. For the 75 cm cavity, this is equivalent to a minimum detectable fractional absorbance of 2.75×10⁻⁶ or 3.7×10⁻⁸ cm⁻¹. The equivalent detection limit for NH₃ of 47.3 ppb is at least an order of magnitude too high for typical ambient measurements.

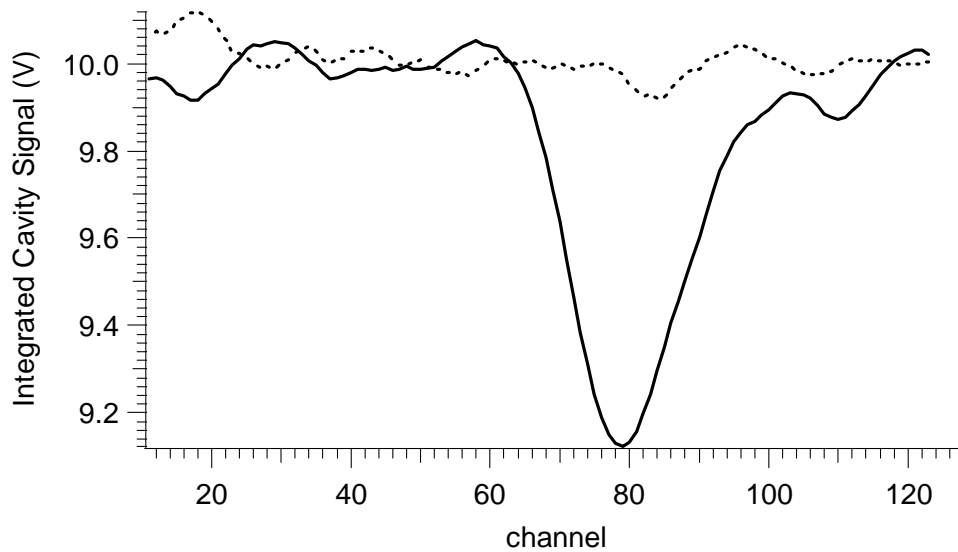


Figure 2-20 CEA background subtracted absorption of 361 ppm NH₃ (solid curve) and consecutive background – background results (dotted curve) normalized to 10 V

As NH₃ is adsorbed easily onto surfaces, especially uncoated stainless steel (Yokelson *et al.*, 2003), sampling of NH₃ through Teflon tubing and a stainless steel cavity is less than optimal. Strong memory effects of NH₃ addition to the cavity were

observed as well. It was typically very difficult to totally flush the cavity of residual NH_3 . For a more thorough investigation of the CEA of NH_3 in the near-IR, an appropriate sampling system would be required to minimize sampling losses. In the above calculation of the detection limit, the result is based on the mixing ratio of the diluted calibration gas from the ratio of flow rates. This calculated mixing ratio is likely much higher than the actual due to the sampling artifacts noted above. Therefore, the minimum detectable NH_3 mixing ratio would be much lower for a setup that minimizes sampling losses.

In addition, although these were brand new mirrors with a specified reflectivity of 99.993% at 1515 nm, the experimentally determined pathlength of 3.0 km is much lower than expected. The predicted effective pathlength for 99.993% reflective mirrors is 10.7 km as calculated from equation (E2.4). Using equation (E2.4) below, a 3 km effective pathlength corresponds to a mirror reflectivity of 99.975%.

$$L_{eff} = \frac{L\sqrt{R}}{1-R} \quad (\text{E2.4})$$

2.1.7 Summary of CEA Results in the Near-IR

The investigation of the CEA technique as applied to CO_2 in the near-IR was an ideal starting point. The instrumental setup was modified as required and experience into the technique was gained.

The experimentally determined effective pathlength from these experiments is roughly 2.5 km, a considerable enhancement from a 75 cm cavity. A 2.5 km pathlength

corresponds to a mirror reflectivity of 99.97% compared to the specified reflectivity >99.99%. As the mirrors were in use for nearly two years, it is possible that the reflectivity may have degraded over time. The reflectivity is very sensitive to any perturbations of the surface. The actual cleaning procedure was tedious and very delicate.

The estimated detection limits of various species absorbing in the near-IR region based on this experimentally determined pathlength, and on estimates of the absorption cross-sections as compared to CO₂ is given in Table 2-1.

Based on these estimates, the detection limits are too high for typical ambient measurements, although they may be adequate for process monitoring, or detection in certain environments. The detection limits could be lowered by many means. Using mirrors with higher reflectivity leads to longer effective

Species	Detection Limit
CO ₂	10 ppm
H ₂ O	8 ppm
CH ₄	100 ppb
NH ₃	10 ppb
C ₂ H ₂	10 ppb

Table 2-1 Estimates of detection limits of various species in the near-IR

pathlengths. In addition, keeping the mirrors free from any impurities will help prolong the high reflectivity. The signal-to-noise ratio in these CO₂ experiments is low.

Minimum detectable optical densities of 1% in a 75 cm cavity are not particularly good, so optimization of the minimum optical density would help to decrease the detection limits. In addition, the absorption transitions in the near-IR are relatively weak, so

utilizing absorptions in other wavelength regions, such as the mid-IR or visible, with strong absorptions would be advantageous.

The Allan Variance method offered the most realistic detection limit. This is likely because in the analysis of the results, the spectra were fitted to the calibration spectrum. In this case, nearly all points of the generated spectrum are used in the fit. In the other analyses, the peak absorption value is used to determine the effective pathlength and minimum optical density. It would be advantageous to use all points to increase the signal-to-noise.

2.2 Cavity Enhanced Absorption in the Visible Region

2.2.1 Overview

To help understand the factors limiting the sensitivity in the near-IR, the study moved to the visible region. The motivation for this adaptation included a recently available diode laser with powerful output at 662 nm, the strong absorption feature corresponding to NO₃, and the weak absorptions of O₃ and NO₂. Another benefit is that working in the visible region provides an excellent diagnostic tool as the cavity effects are visible to the naked eye.

There has been a great deal of research into the absorption spectrum of NO₃ and quantification of the absorption cross-section. The absorption spectrum of NO₃ is shown in Figure 2-21 (Sander *et al.*, 2006). The absorption cross-section at 662 nm is approximately $2.25 \times 10^{-17} \text{ cm}^2 \text{ molecule}^{-1}$ with a width of approximately 80 cm^{-1} , (3.5

nm) FWHM (Brown *et al.*, 2002a). Based on a compilation of the available data, Wayne *et al.*(1991) estimated the temperature dependence of σ_{662} based on an upper limit temperature dependence, $\sigma_1 = 4.39 \times 10^{-17} - (7.69 \times 10^{-20} \times T) \text{ cm}^2 \text{ molecule}^{-1}$, and an average temperature dependence, $\sigma_2 = 3.63 \times 10^{-17} - (5.13 \times 10^{-20} \times T) \text{ cm}^2 \text{ molecule}^{-1}$. In another study, Yokelson *et al.* (1994), calculated the temperature dependence of the cross-section at 661.9 nm to be $\sigma_{661.9} = (4.56 - 0.00787T) \times 10^{-17} \text{ cm}^2 \text{ molecule}^{-1}$.

The width of the absorption at 662 nm is broader than the tuning range of a typical tunable diode laser. Because of this, the laser wavelength was typically held constant at peak centre rather than tuned continuously to generate the spectrum.

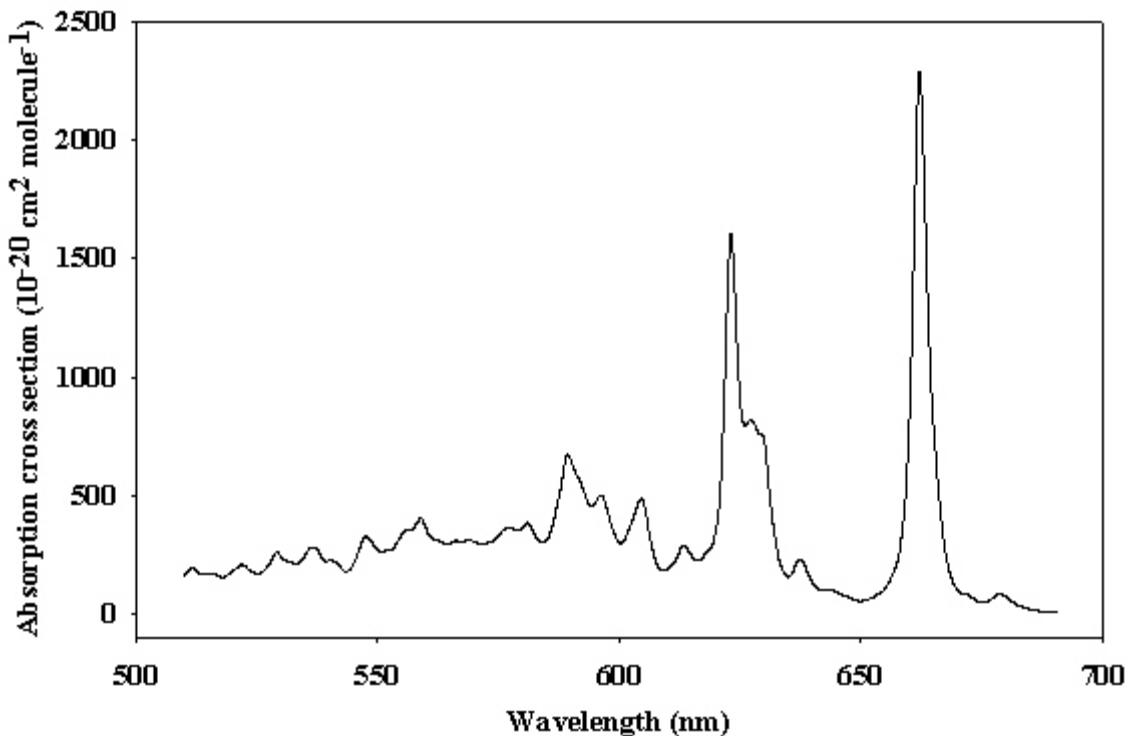


*Figure 2-21 Absorption cross-sections of NO₃ in the visible region (Sander *et al.*, 2006)*

Because of this, an alternative method is required to obtain the background signal. Titration of the ambient sample with a small amount of NO will rapidly convert the NO₃ to NO₂ yielding a background where only the analyte of interest has been removed. This background determination is highly effective for minimizing any possible interferences since they will be present in both the sample and the background. Although NO₂ does absorb radiation at 662 nm, the optical attenuation produced by the production of two NO₂ molecules from this titration is negligible since the absorption cross-section of NO₂ is roughly 10⁴ times less than that of NO₃ at 662 nm.

Since the air is sampled through an optical cavity, the N₂O₅ (or more precisely N₂O₅ + NO₃) can also be measured, simply by heating of the sample. Heating of the sample converts the N₂O₅ to NO₃ + NO₂ via the strongly temperature dependent equilibrium reaction (R1.6) allowing for detection of N₂O₅ as NO₃.

One of the biggest challenges with the various cavity techniques with respect to NO₃ is the difficulty with sampling. Since NO₃ is a radical species, it is highly reactive, thus sampling losses need to be minimized and characterized.

Two important species for studies of the nitrate radical, O₃ and NO₂, also have appreciable absorption features at 662 nm. The absorption cross-sections at 1000 mbar and 293 K of NO₂ by Fourier Transform Spectroscopy, FTS (Voigt *et al.*, in preparation) and the GOME spectrometer (Burrows *et al.*, 1998) and of O₃ by FTS (Voigt *et al.*, 2001) and GOME (Burrows *et al.*, 1999) are shown in Figure 2-22.

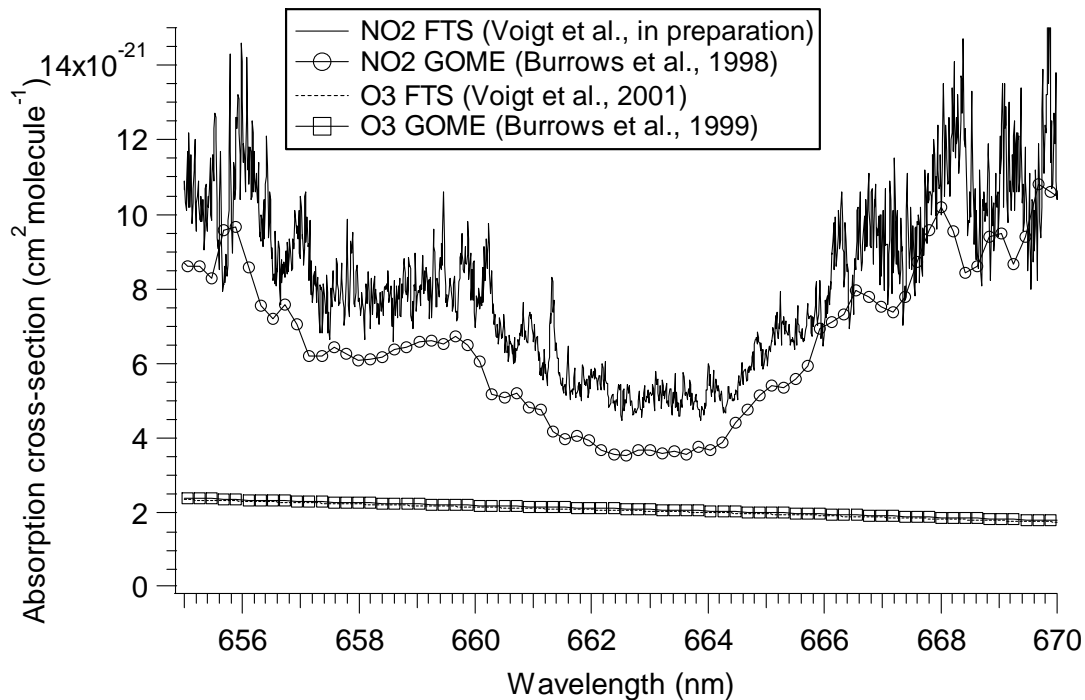


Figure 2-22 Absorption cross-sections of O_3 and NO_2 near 662 nm

The presence of O_3 and NO_2 absorption in this region allows these species to be utilized as test gases since they are relatively easy to handle. O_3 in particular is useful for testing purposes, as it can be produced inline from the air carrier gas without the need for addition of other gases. In addition, for O_3 the absorption cross-section is more easily deduced around 662 nm due to the lack of fine structure compared to the spectrum of NO_2 .

2.2.2 Instrumental Setup for CEA in the Visible Region

For the NO_3/N_2O_5 experiments in the visible region, the laser used (Thorlabs ML101J8) had a specified wavelength range of 655 to 666 nm with a typical power of up

to 45 mW in continuous-wave operation. The optical components were setup on a vibrationally isolated optical bench in a similar configuration as shown in Figure 2-6. An anamorphic prism pair (Thorlabs PS877) was placed directly in front of the laser mount to transform the elliptical beam profile to a circular profile. To allow for off-axis experiments, rather than adjusting the tilt of the cavity with respect to the beam, the cavity was mounted solidly and the external mirror closest to the cavity was placed on two translational stages (x-y) and mounted on a kinematic plate for adjustment of the beam input angle. The cavity output was focused onto a silicon photodiode detector (Thorlabs, FDS 010) located approximately 10 cm from the exit mirror.

The initial cavity setup was based on a system used by Brown *et al.* (2001) for cavity ringdown detection of NO₃ and is shown in Figure 2-23. For the cavity experiments in the visible region, the highly reflective mirrors (Los Gatos Research, Inc.), with a radius of curvature of 1 m, diameter of 1", and a specified reflectivity of 99.9995% at 662 nm (Figure 2-24) were used. A small flow of dry N₂ (50 sccm per mirror) was introduced adjacent to the mirrors to act as a cushion gas to keep the mirrors clean. The gas sample inlet and outlet were connected to the cavity at a 45° angle to reduce turbulence. The sample inlet and the cavity section were independently temperature controlled.

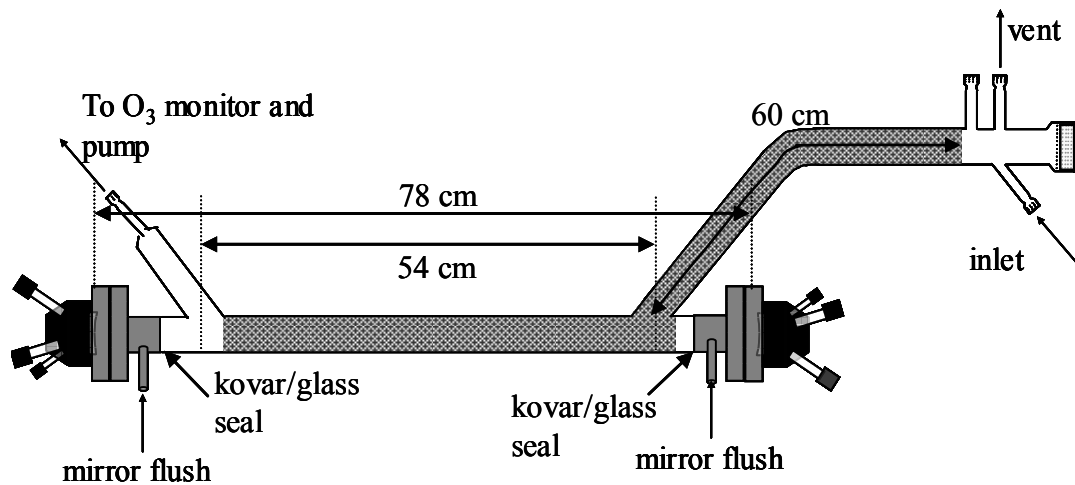


Figure 2-23 Initial cavity setup for experiments in the visible region. The shaded region is the heated section. All glass is 1" OD

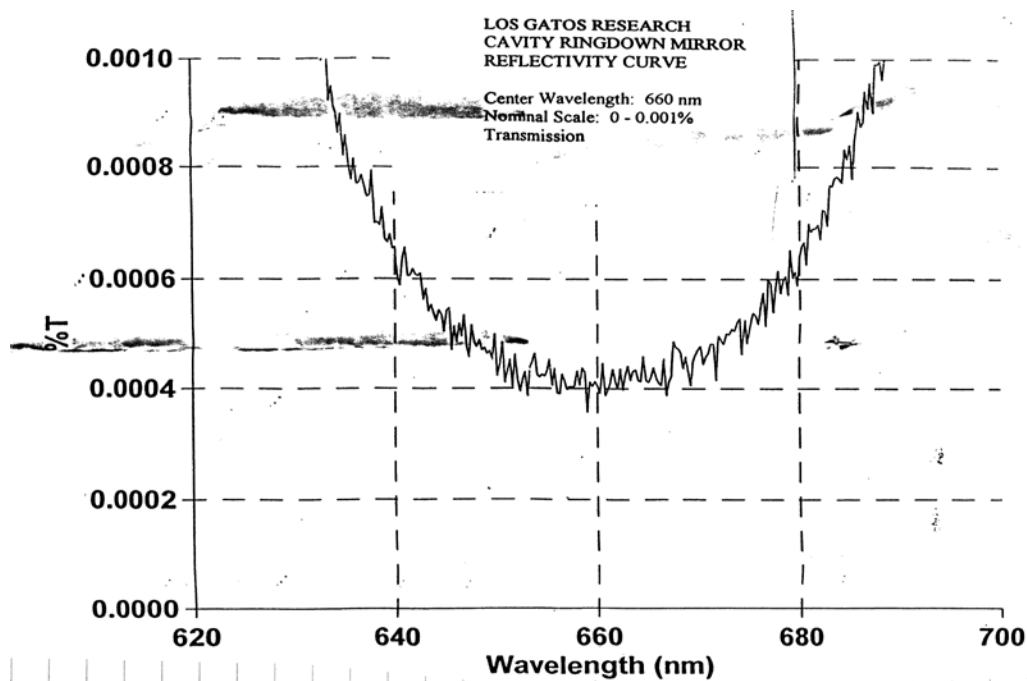
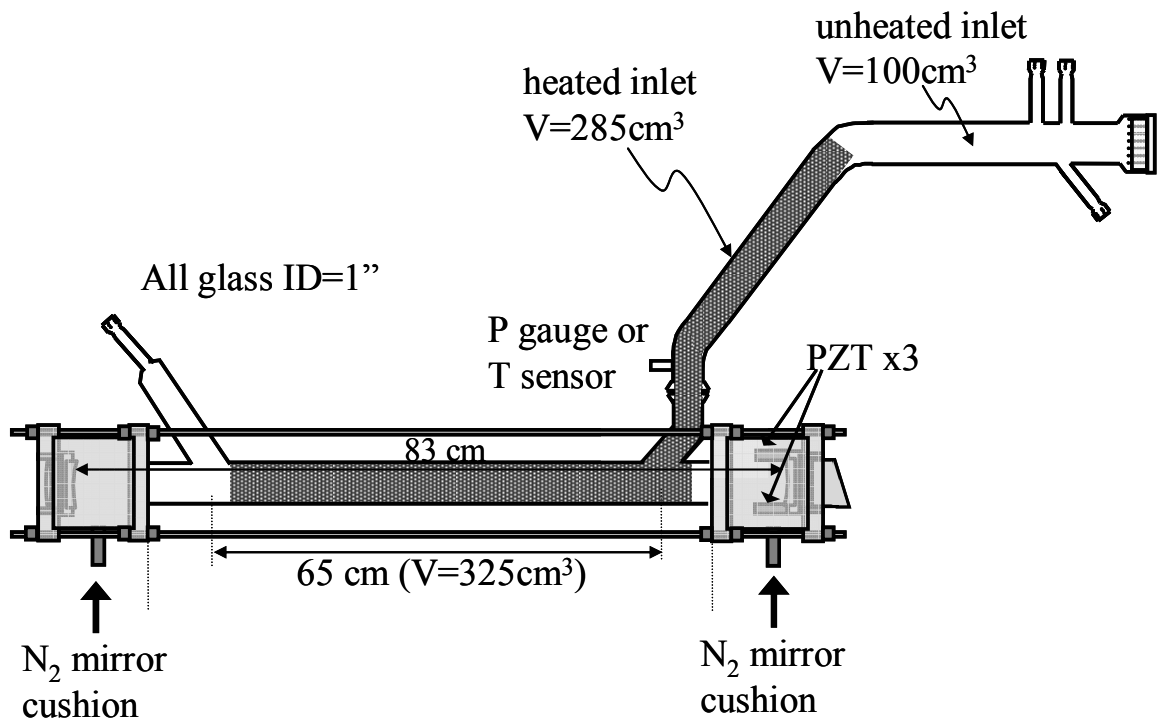


Figure 2-24 Manufacturer specified reflectivity curve for the highly reflective mirrors near 662 nm. The y-axis, %T, is equivalent to 100%-R (reflectivity)

A second set of mirror mounts was constructed to allow for thermal expansion of the glass cavity without affecting the mirror separation (Figure 2-25) with a mirror separation of 75 cm and a sample length of 65 cm. The mirrors were mounted on kinematic plates with adjustment screws located on the outside of the back plate. Three piezo-electric transducers (Thorlabs, AE0505D16) were attached to the three adjustment screws of the kinematic plate holding the entrance mirror. The cavity optical entrance was sealed on an angled window. The optical exit was sealed on a lens with a focal length of 10 cm to allow for focusing onto the detector. With the exception of the highly reflective mirrors, all optical components were coated with an anti-reflection coating.



**Figure 2-25 Modified cavity setup for experiments in the visible region.
The shaded area is the heated section**

The two mirror mount sections were connected by four threaded steel rods. The glass tube was sealed to the mirror mounts on o-rings at each end and the end plates squeezed together to seal to the glass. A connector attached to each mirror mount allowed for addition of a small flow of N_2 as a cushion gas to protect the mirrors.

2.2.3 Visible Diode Laser Characterization

Since the width of the NO_3 absorption feature at 662 nm was beyond the continuous tuning range of the tunable diode laser (Thorlabs ML101J8), the laser output was held constant at 662 nm. The laser was characterized with a monochromator (Jarrell Ash, 0.5 m) which was calibrated with a He-Ne laser prior to use. The laser temperature and current were chosen such that the laser output power was maximized at 662 nm. The laser conditions for output at 662 nm were a laser temperature and current of 30.1°C and 110 mA, respectively, providing an output power of approximately 37 mW of continuous-wave radiation. The result of the laser characterization is shown in Figure 2-26.

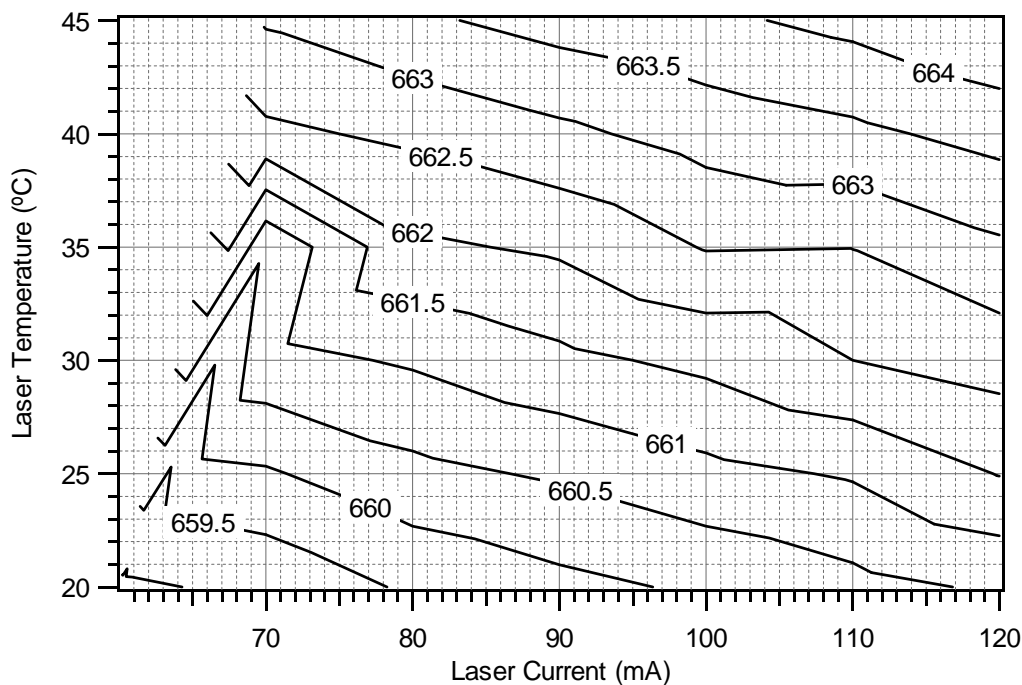


Figure 2-26 *NO₃ laser output wavelength (nm) as a function of laser temperature and current*

2.2.4 Laboratory Synthesis of N₂O₅

Solid N₂O₅ was used as the source for NO₃ and N₂O₅ for laboratory studies. The initial procedure was trap-to-trap distillation (Davidson *et al.*, 1978). In this synthesis, a small flow of pure NO was added to an excess of O₃ and the resulting product was collected in a dry ice/ethanol trap.

A diagram of the trap-to-trap setup is shown in Figure 2-27 and was set up inside a fumehood. Approximately 1% O₃ in O₂ was generated by passing P₂O₅ dried O₂ (Extra dry, BOC) at several lpm through a commercial ozone generator (PCI Ozone Corp.). A

small flow of pure NO (CP grade, BOC), dried with a P_2O_5 trap, was added to the O_3 flow and allowed to mix in a 2 l mixing volume.

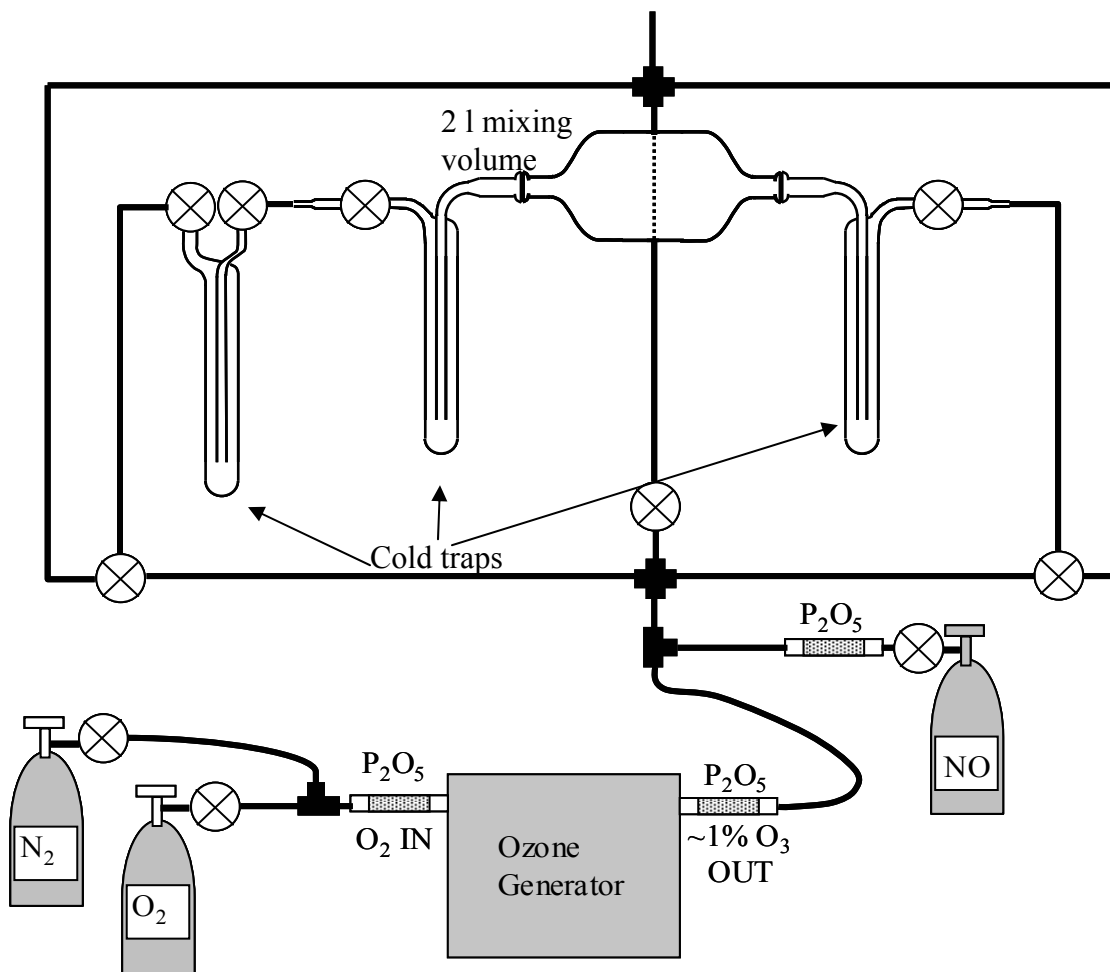


Figure 2-27 Trap to trap distillation setup for N_2O_5 synthesis

Nitric oxide was used as the starting reagent rather than NO_2 since NO is easier to dry (Osborne *et al.*, 2000). Due to the high O_3 concentrations, the NO is titrated completely with O_3 , to produce NO_2 (R1.5). The NO_2 further reacts with O_3 to produce NO_3 (R1.1). Once created, the NO_3 reacts with NO_2 to form N_2O_5 (R1.6). The N_2O_5 was

collected in a -78.5°C (dry ice/ethanol) trap. At this trap temperature, the $\text{NO}_3 + \text{NO}_2 \rightarrow \text{N}_2\text{O}_5$ strongly favours N_2O_5 . Further purification was required to remove any impurities, such as the NO_2 dimer, N_2O_4 . The collected impure solid sample was a white crystalline powder corresponding to N_2O_5 with some blue colour characteristic of N_2O_4 . Purification of the product was attained by evaporation followed by further reaction with O_3 in the reverse direction. Several purification steps were required to obtain a pure solid N_2O_5 sample.

A simplified method for producing solid N_2O_5 was obtained from J. Crowley (personal communication). With the previously described setup, a significant HNO_3 contamination was observed. HNO_3 is produced by the reaction of N_2O_5 and water vapour suggesting a H_2O source. To eliminate this H_2O source, all tubing was replaced with stainless steel or glass. The modified setup is shown in Figure 2-28. The three glass valve arrangement of this trap allowed the trap to be bypassed for flushing of the lines with the trap closed. N_2O_5 was produced by the same reactions described above. More rigorous control of the flow rates produced a much purer product, thus not requiring further purification. In this method, the initial reactants (O_3 and NO) were mixed in a 1 l mixing volume with a residence time of approximately 1 minute. With the high concentrations and the long mixing time, NO_3 and N_2O_5 are formed rapidly with negligible NO and NO_2 remaining.

The flow rates for formation of the solid N_2O_5 were 1 lpm for the 1% O_3 in O_2 and 2 sccm for the pure NO flow. Using FACSIMILE (Curtis and Sweetenham, 1987) to

model this N_2O_5 production method, based on the high concentrations and the excess O_3 , the NO conversion to NO_2 and further oxidation to NO_3 are extremely rapid, yielding high concentrations of NO_3 and N_2O_5 with limited NO_2 left over and essentially no NO after the 1 minute mixing time. At the low temperature of the cold trap ($-78.5^\circ C$), the only remaining species are NO_3 and N_2O_5 , which forms as an essentially pure solid at this temperature.

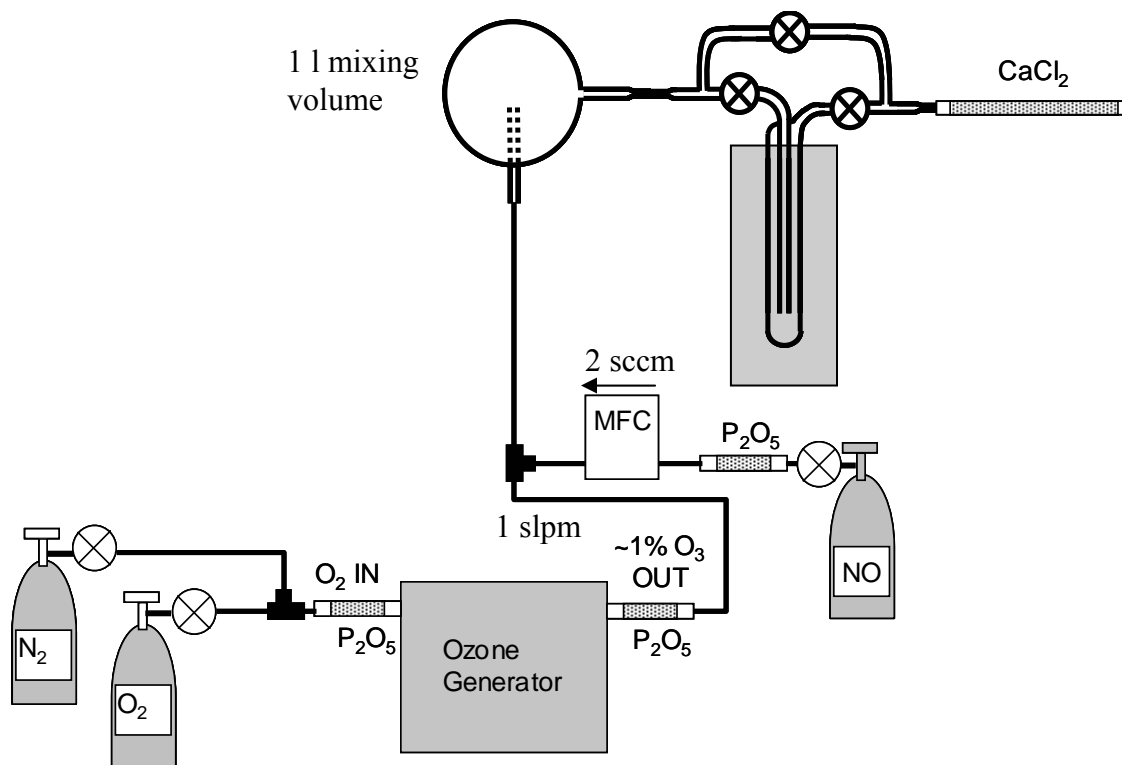


Figure 2-28 *Simplified single mixing scheme (Crowley, J., personal communication) for N_2O_5 production*

2.2.5 Characterization of the N₂O₅ Sample

Solid N₂O₅ was used as a source for NO₃. After production of the N₂O₅ sample, the sample was characterized and quantified using a Bruker IFS 66v FTIR. N₂O₅ sublimates above 33°C, and the vapour pressure as a function of temperature (Linde, 2005) is shown in Figure 2-29.

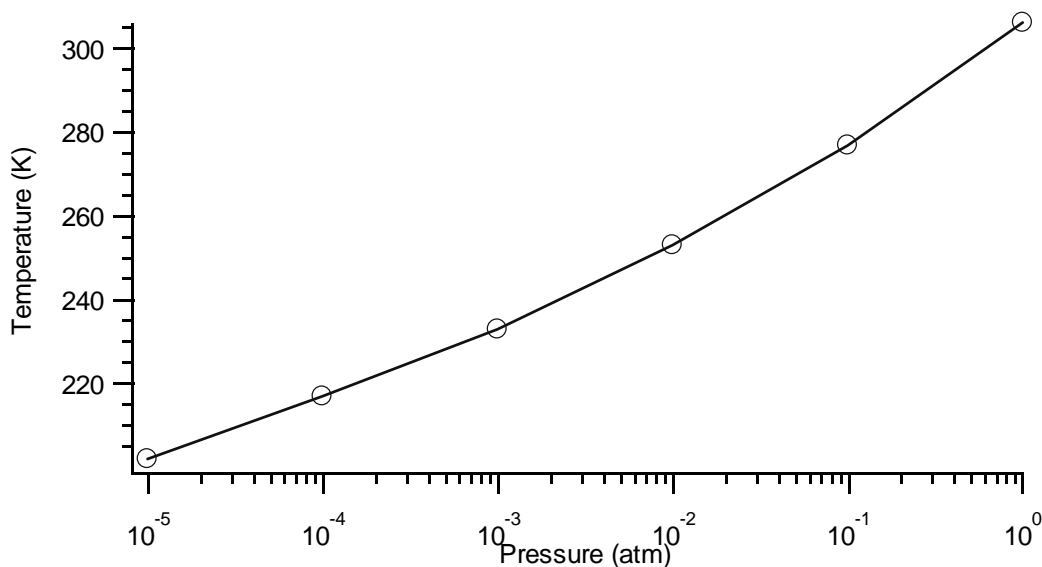


Figure 2-29 N₂O₅ vapour pressure as a function of temperature (Linde, 2005)

A Labview routine was created to calculate the HNO₃ and NO₂ absorption cross-sections at 1 atm and 298 K in the mid-IR using a Voigt profile based on the known linestrengths and linewidths from the HITRAN database (Rothman *et al.*, 2004). The N₂O₅ peak absorption cross-section at 1246 cm⁻¹ and 1716 cm⁻¹ are 1.81 × 10⁻¹⁸ and 1.97 × 10⁻¹⁸ cm² molecule⁻¹, respectively (Cantrell *et al.*, 1988). The measured FTIR spectrum for N₂O₅ (298 K, 1 atm), as well as the absorption cross-sections for HNO₃ and

NO₂ are shown in Figure 2-30. The presence of NO₂ in an N₂O₅ gas sample would suggest thermal decomposition of the N₂O₅, particularly if the trap temperature (-78.5°C) is not maintained while in storage. The peak at 1246 cm⁻¹ was used to quantify the N₂O₅ since it is clear of these potential interfering species.

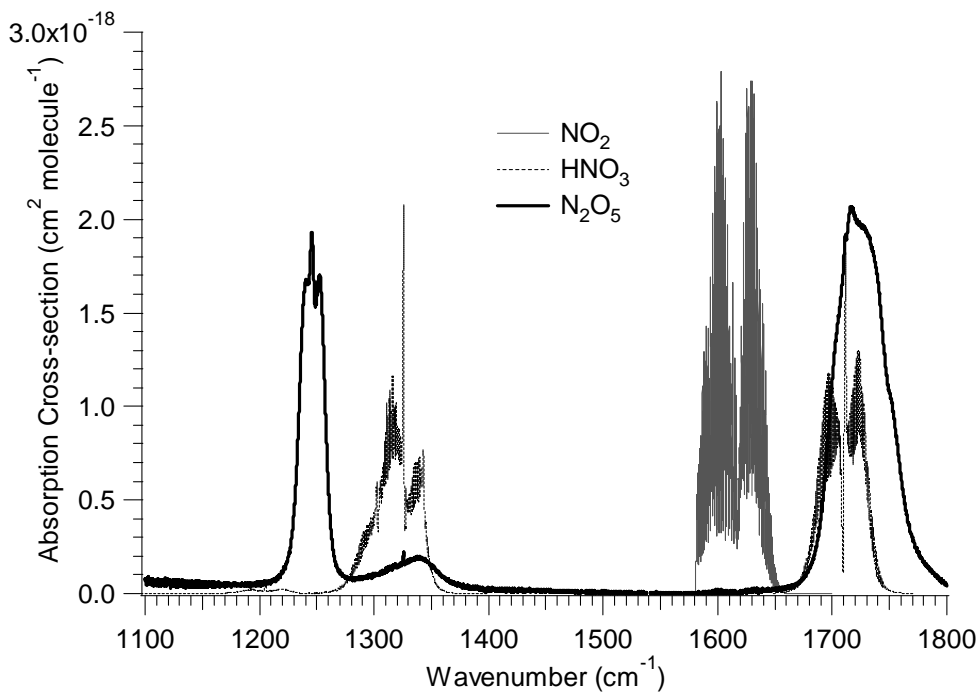


Figure 2-30 Mid-IR absorption cross-sections for N₂O₅, NO₂ and HNO₃; NO₂ and HNO₃ calculated from HITRAN database (Rothman et al., 2004) and N₂O₅ from Cantrell et al. (1988)

Figure 2-31 shows an example of the FTIR spectrum for the N₂O₅ sample at a bath temperature of approximately -50°C for the two production methods. As can be seen from the lower graph, implementation of the Crowley method effectively removed the HNO₃ and NO₂.

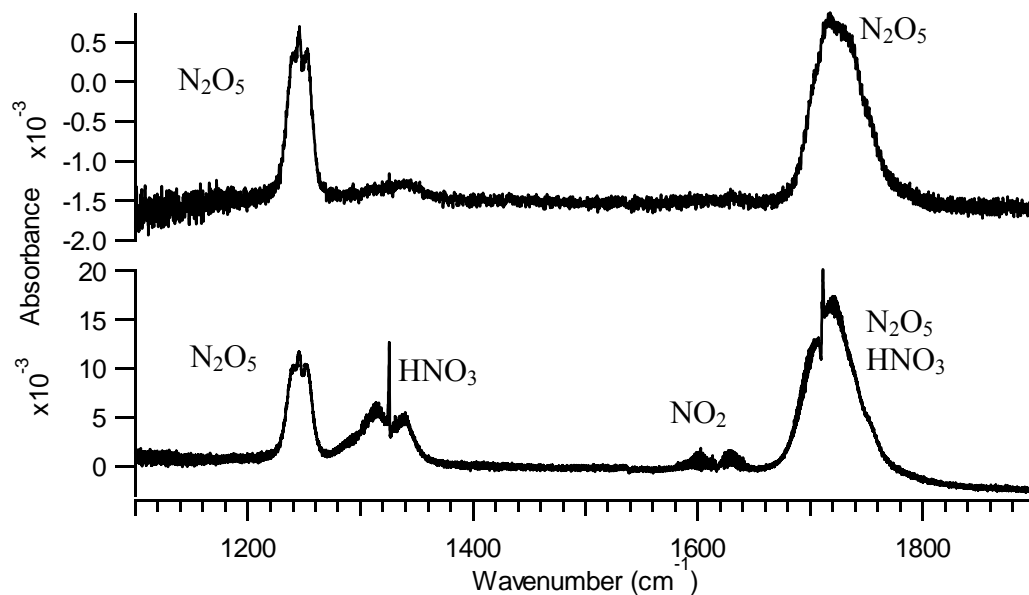


Figure 2-31 FTIR spectra of N_2O_5 sample produced from trap-to-trap distillation (lower spectrum) and single mixing (Crowley, J., personal communication) (upper spectrum)

2.2.6 Gas Sampling System for the Detection of NO_3 in the Visible Region

The NO_3 radical was produced by the thermal decomposition of N_2O_5 (R1.6). The high sensitivity of CEA and CRD required double dilution of the N_2O_5 source (Figure 2-32). A small carrier flow of air (500 sccm MFC) flowed through the N_2O_5 trap and the N_2O_5 vapour/air mixture was quantified with the FTIR, generating flows of approximately 10 ppm N_2O_5 . This flow was then diluted with a high flow of dried ultrazero air (10 slpm MFC) and a large fraction of this flow was drawn off through an MFC (10 slpm) and a pump. The small remaining flow (a few hundred sccm) was then

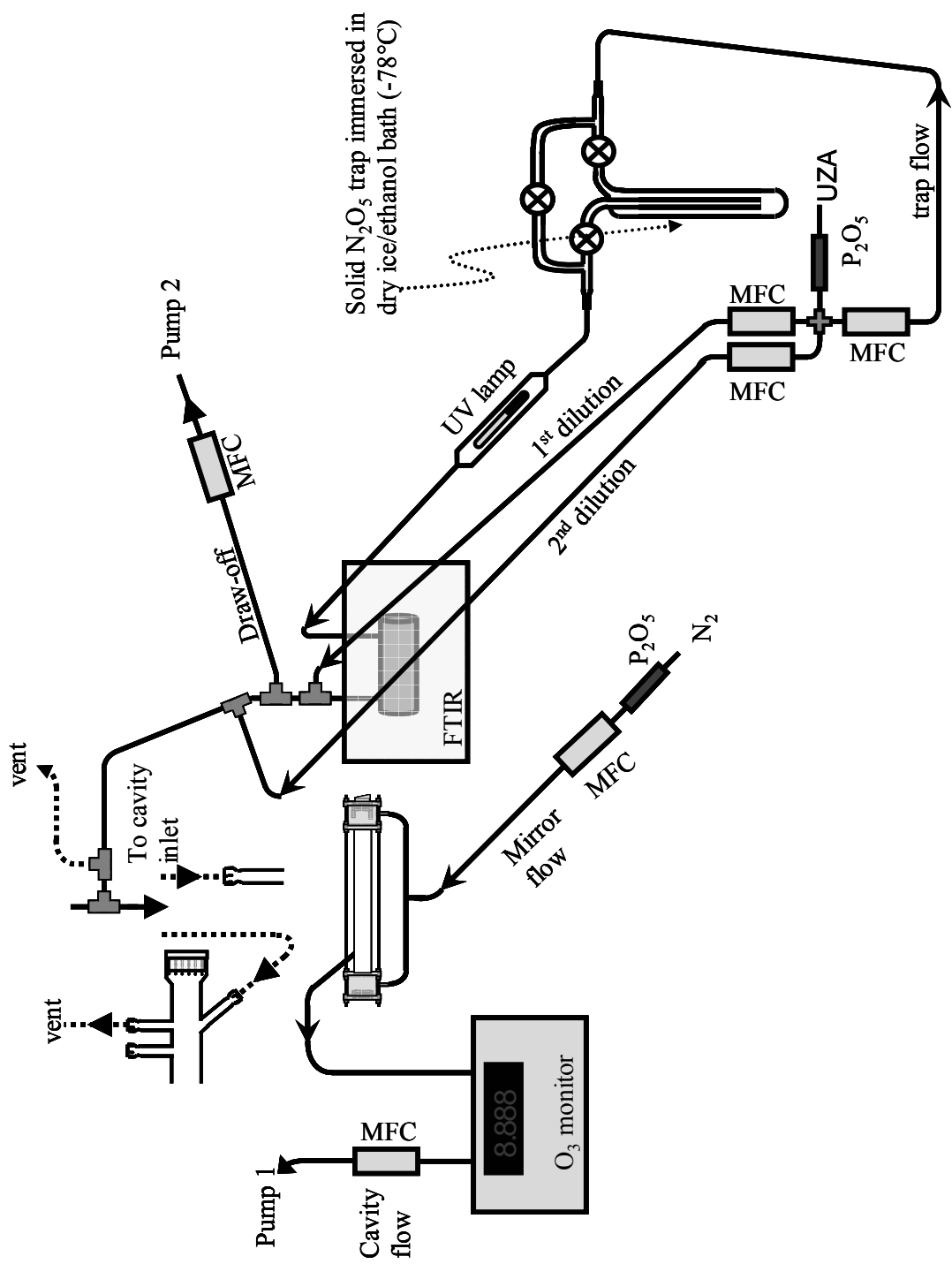


Figure 2-32 Double dilution flow arrangement for CEA and CRD for N_2O_5 and NO_3 in the visible region

diluted further with the addition of another large flow of air (10 slpm MFC). The cavity drew off approximately 2 slpm of this double diluted flow with the excess flowing through the vent at atmospheric pressure. The flow rates were adjusted to generate the desired mixing ratios for introduction to the cavity.

Backgrounds for ambient measurements were obtained via the titration of NO_3 with NO (R1.4). To ensure adequate mixing of the small NO flow (0 – 100 sccm) into the larger flow, the stainless steel tee was machined so that the tube containing the NO flow protruded to the centre of the main flow. Control of the NO flow was provided from a computer-controlled 3-way solenoid valve.

2.2.7 Visible Cavity Effects as a Diagnostic Tool

The visualization of the light in the cavity and the cavity output was important in understanding the cavity enhancement effects. When air was added to the cavity, significant observable Rayleigh scattering within the cavity gave an idea of the intensity of the enhanced radiation. Rayleigh scattering from the laser beam was not observable when viewing transverse to the beam axis before the cavity. The beam profile as a function of off-axis alignment could also be visualized within the cavity. Leaks or inadequate filtering resulted in scattering from particles, which was visible to the naked eye.

The sensitivity and stability of the cavity were dependent on the alignment. The output pattern from the cavity was also a function of the alignment. It was often easier to

align the cavity based on the visible cavity output rather than the detected signal viewed on an oscilloscope. By adjusting the alignment of the cavity and by aligning the cavity off-axis, various output patterns were obtained, a few of which are shown in Figure 2-33. The photographs (1a – 1c) show the characteristic TEM_{mn} modes. TEM_{mn} modes of nearly any configuration could be achieved by adjustment of the cavity alignment and the off-axis alignment. Also occasionally observed (not shown in the figure) were cavity output patterns corresponding to the Lissajous patterns created by off-axis alignment with astigmatic mirrors (McManus *et al.*, 1995). Typically, the single cavity mode output depicted by photo 1a provided the optimum combination of high cavity output and signal stability.

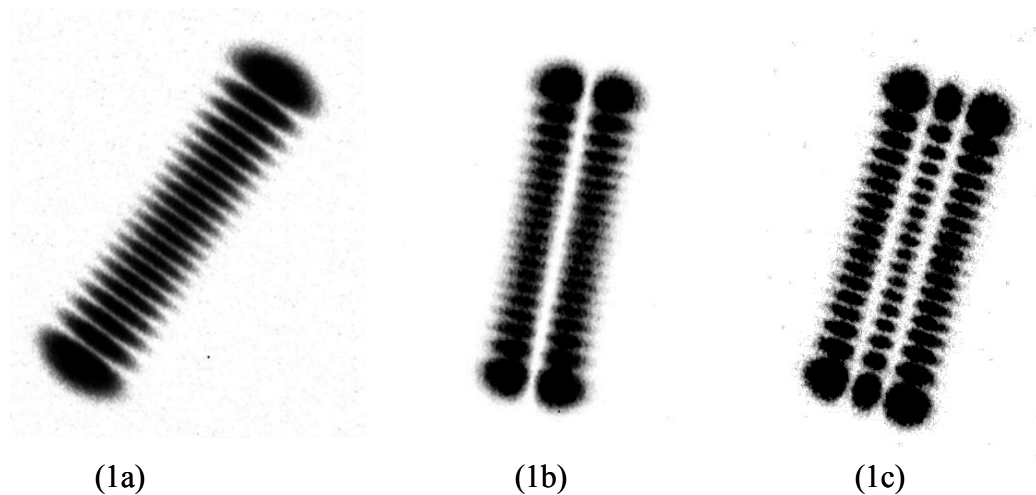


Figure 2-33 Photographs of off-axis cavity output as viewed on a white card approximately 1 to 2 m from the cavity output mirror. Photographs 1a to 1c show the typical TEM_{mn} modes obtained from off-axis alignment

2.2.8 CEA Tests in the Visible Region

2.2.8.1 Pathlength and Sensitivity Determination

The first experiments in the visible region were to gain insight on the characteristics of the CEA technique with the new setup. The nitrate radical is notoriously difficult to use due to its high reactivity. NO_2 and O_3 are much easier to handle and quantify and were used for preliminary tests and calibration. These preliminary tests included optimization of parameters such as, PZT amplitude/frequency, laser modulation, and flow rates.

Determination of the pathlength and linearity of the absorbance were obtained by varying the mixing ratio of NO_2 within the cavity. NO_2 from a standardized cylinder (4.6 ppm NO_2 in N_2 , BOC) was mixed with a larger flow of ultrazero air from a cylinder to produce mixing ratios ranging from 200 to 1500 ppb. The integrated cavity output signal as function of NO_2 mixing ratios is shown in Figure 2-34. Each data point is 2 seconds and consists of 128 signal integration points. 5-minute segments consisting of 19 200 data points (128×150) were averaged to obtain the absorption as a function of NO_2 mixing ratio (Figure 2-35). From Figure 2-35, the fit of the calibration curve has a slightly negative intercept. As will be discussed, this non-zero intercept is likely due to the variation in cavity output signal that were observed upon addition of the NO_2 flow to the main carrier flow.

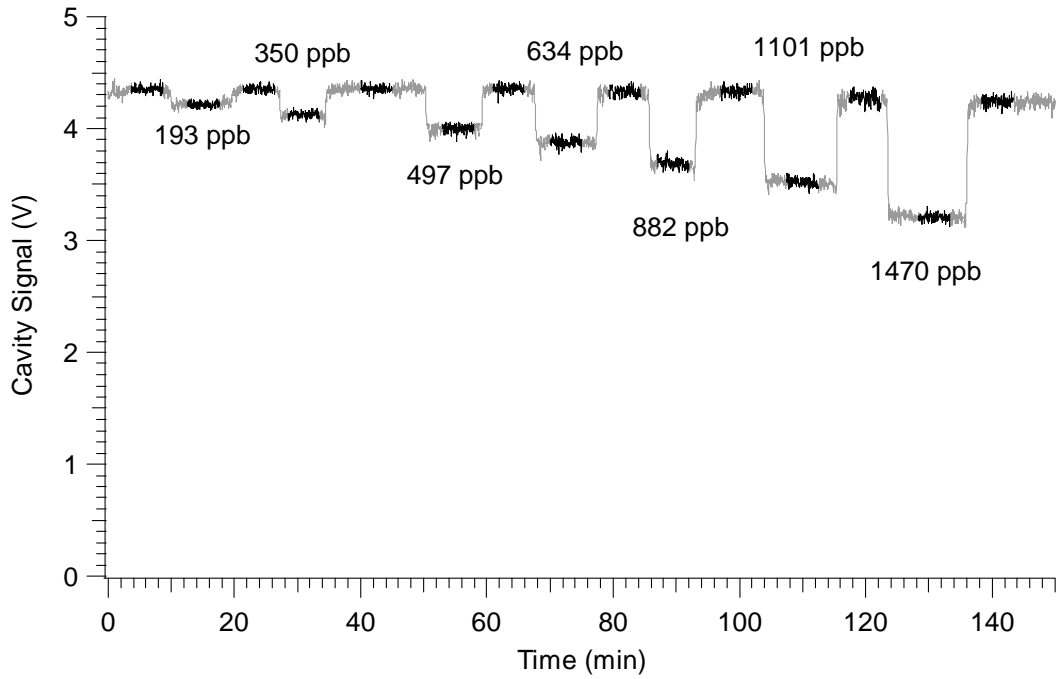


Figure 2-34 2 second averages (grey curve) of integrated cavity signal over time showing decrease in signal with addition of NO_2 ; the black portions are the sections used in the 5 minute average

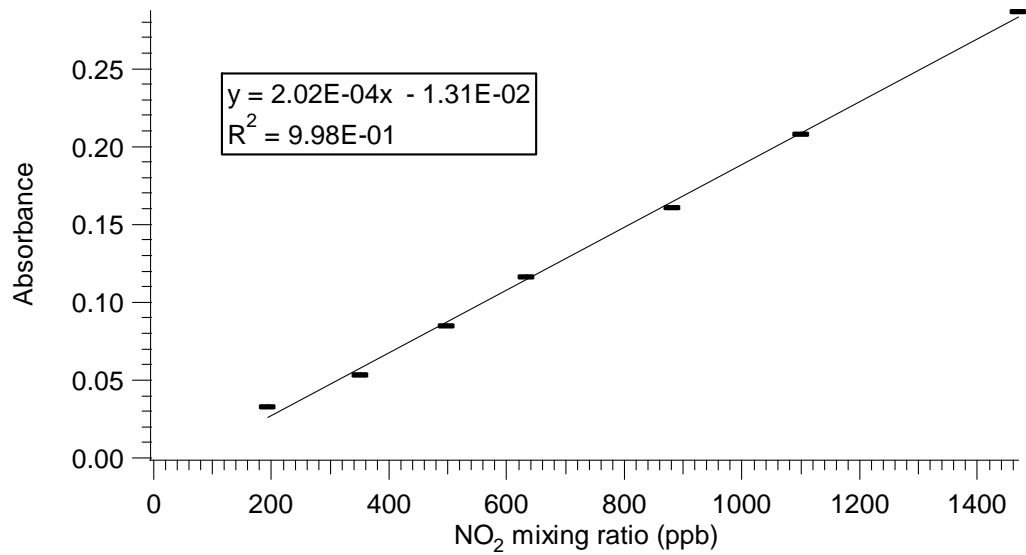


Figure 2-35 Calibration curve of cavity enhanced absorbance for various mixing ratios of NO_2

The effective pathlength of the cavity can be obtained from the Beer-Lambert law (E1.1) using the known absorption cross-section for NO₂ at this wavelength ($\sigma = 4 \times 10^{-21} \text{ cm}^2 \text{ molecule}^{-1}$) and the slope of the absorbance as a function of NO₂. The average effective pathlength based on the above data was $18.0 \pm 1.5 \text{ km}$.

The detection limit can be determined by the standard deviation of the 5 minute average for the background signal. For the 5 minute data the standard deviation of the average signal was approximately 0.001 V (0.02%). This corresponds to a 3σ detection limit for NO₂ of 6 ppb. Considering that the absorption cross-section for NO₃ is roughly 5000 times higher than that of NO₂, the equivalent detection limit for NO₃ is 1.2 ppt neglecting any sampling losses and other sources of uncertainty, such as drift.

A similar analysis was performed using O₃ as the test gas. Ozone is produced in the air stream by photolysis of O₂ with a UV lamp. Variable O₃ mixing ratios can be produced by varying the amount of radiation reaching the flow or by varying the flow rate through the photolysis section. The integrated cavity output signal as function of O₃ mixing ratio is shown in Figure 2-36. The upper portion of the figure is the baseline signal with no O₃ added and the absorbance for 5 minute segments were plotted as a function of the O₃ mixing ratio (Figure 2-37).

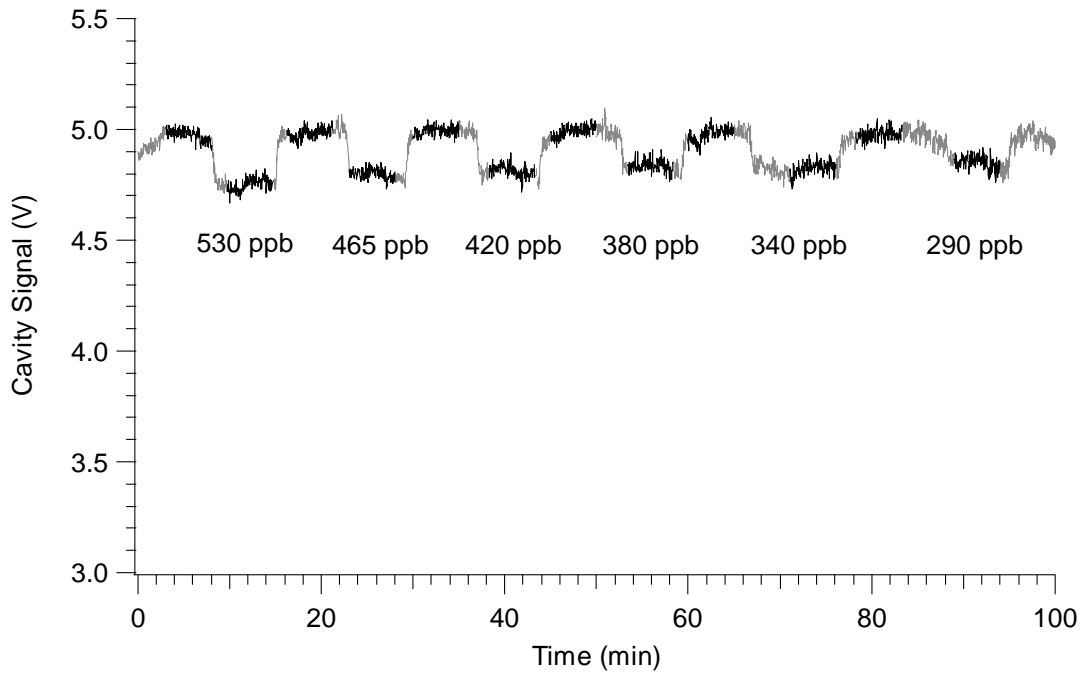


Figure 2-36 2 second averages (grey data) of integrated cavity signal over time showing decrease in signal with addition of O₃; the black portions are the sections used in the 5 minute average

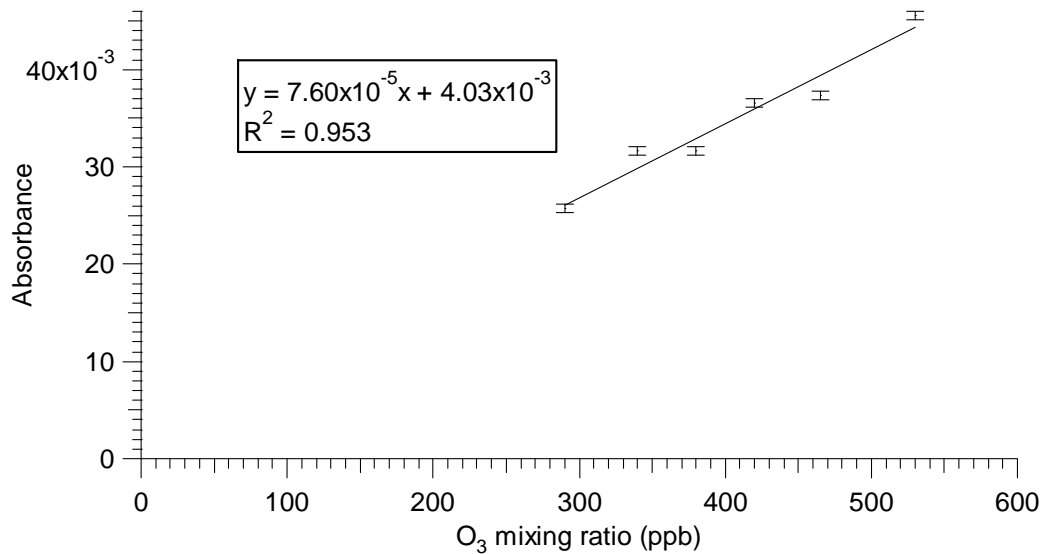


Figure 2-37 Calibration curve for cavity enhanced absorbance of various mixing ratios of O₃

Following a similar statistical analysis as for NO₂, the average effective pathlength was 17.6 ± 0.9 km, a value consistent with that determined from the NO₂ experiments. The typical standard deviation of the 5 minute average for the baseline signals was 0.001 V (0.02%) resulting in a 3σ detection limit for O₃ of 6 ppb. Considering that the absorption cross-section for NO₃ is 10 000 times higher than that of O₃ ($\sigma = 2 \times 10^{-21}$ cm² molecule⁻¹), the equivalent detection limit for NO₃ is 0.6 ppt neglecting any sampling losses. The slightly higher detection limit from the NO₂ calibration was likely due to the change in stability observed when the NO₂ gas source was added to the air carrier flow (pressure pulses), and uncertainty in the absorption cross-section near in this region.

2.2.8.2 Parameter Optimization of CEA in the Visible Region

The various applied modulations for ensuring a constant cavity throughput were qualitatively investigated. Modulation of the laser wavelength did not aid in maintaining a steady signal. As the frequency and amplitude increased, the cavity output signal became increasingly unstable. The optimum conditions for ensuring a high, steady cavity output signal were with the applied modulation to the PZT only, with a frequency of 100 Hz and a displacement of 7 μ m, with no laser modulation applied.

2.2.8.3 Temperature and Pressure Effects on Cavity Output

Since the cavity output is very dependent on the mirror separation due to the resonant effects, a temperature dependence was expected. Changes in the cavity

temperature caused thermal expansion of the glass resulting in changes of the mirror separation and alignment. When the cavity temperature was stable, the cavity alignment remained stable, although long-term drifts were occasionally observed. Rapid changes in temperature resulted in the complete loss of alignment. To increase the stability the cavity configuration of Figure 2-25 was designed and built. This produced a setup where the mirror separation was independent of the glass cavity tube.

Pressure pulses were often observed upon introduction of additional gases to the main flow, such as addition of NO₂. Since O₃ can be produced *in situ*, pressure pulses were never an issue and thus O₃ was preferred as the calibration source.

2.2.9 *In Situ* Production of NO₃

Initial experiments were performed using an NO₂ and O₃ flow system to produce NO₃. Ozone (<2 ppm) reacted with NO₂ (<600 ppb) in a 2 l mixing bulb with a residence time of approximately 90 seconds. The sample inlet and cavity were heated to 90°C to drive the N₂O₅ / NO₃ + NO₂ equilibrium to NO₃. With this *in situ* production method of N₂O₅ and NO₃, when the cavity and sample inlet were at room temperature, the only cavity absorption signal was due to NO₂ and O₃; no NO₃ absorption was detected. Figure 2-38 shows the heated cavity signal as a function of time. The figures show the decrease in cavity signal due to a single component (O₃ or NO₂) and the effect of the cavity signal when O₃ and NO₂ are mixed. Based on the absorption strengths of NO₂ and O₃, the decrease in signal is too high to be due to only NO₂ and O₃. From the calculated

contributions of NO_2 and O_3 to the detected signal, the contribution of NO_3 was calculated to be 70 and 262 ppt, for mix 1 and mix 2 of the figure, respectively.

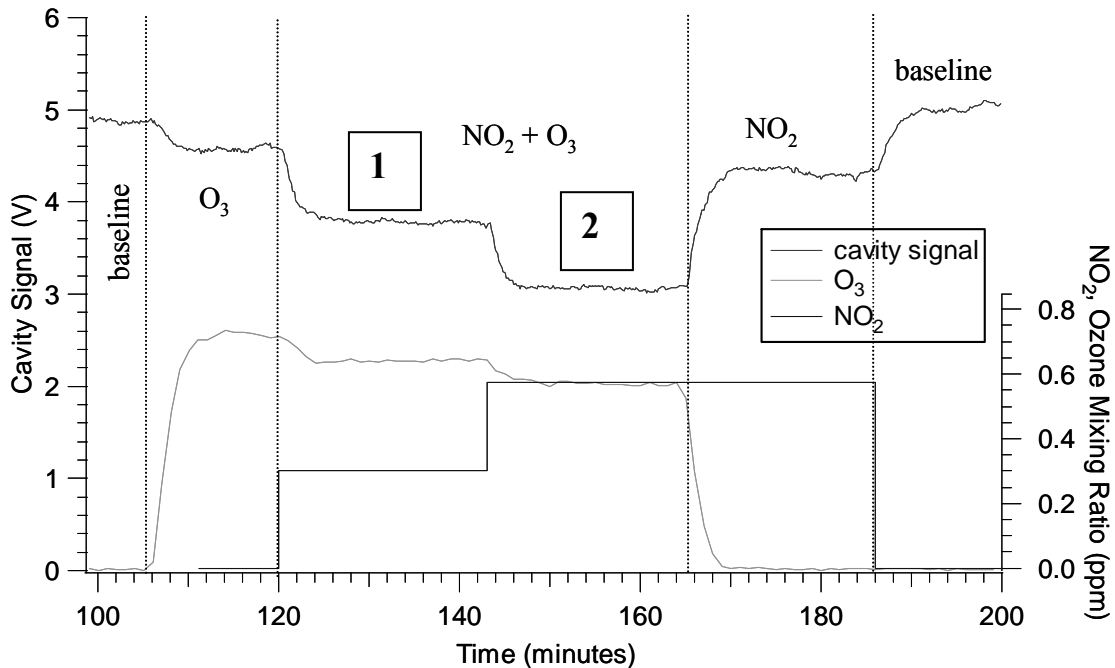


Figure 2-38 Examples of the integrated cavity enhanced absorption signal as NO_2 and O_3 are added producing NO_3 for the inlet and cavity heated to 90°C

Using the initial conditions of O_3 and NO_2 , the expected concentration of NO_3 was modeled using Accuchem (Braun *et al.*, 1988) for the various residence times based on the NO_3 formation reaction and the $\text{N}_2\text{O}_5 / \text{NO}_3 + \text{NO}_2$ equilibrium. The results of the model are shown in Figure 2-39. After reacting for 84 seconds, the sample is heated to 90°C causing the N_2O_5 equilibrium to shift rapidly towards $\text{NO}_3 + \text{NO}_2$. The extent of dissociation depends on the temperature and the concentration of NO_2 , therefore the N_2O_5 does not fully dissociate due to the presence of high amounts of NO_2 . The shaded section

of the graph is the residence time within the optical cavity. Within the cavity, the modeled concentrations are approximately 2 orders of magnitude higher than those observed experimentally. This simplified model does not take into account any loss mechanisms, such as wall losses or the potential thermal dissociation of NO_3 .

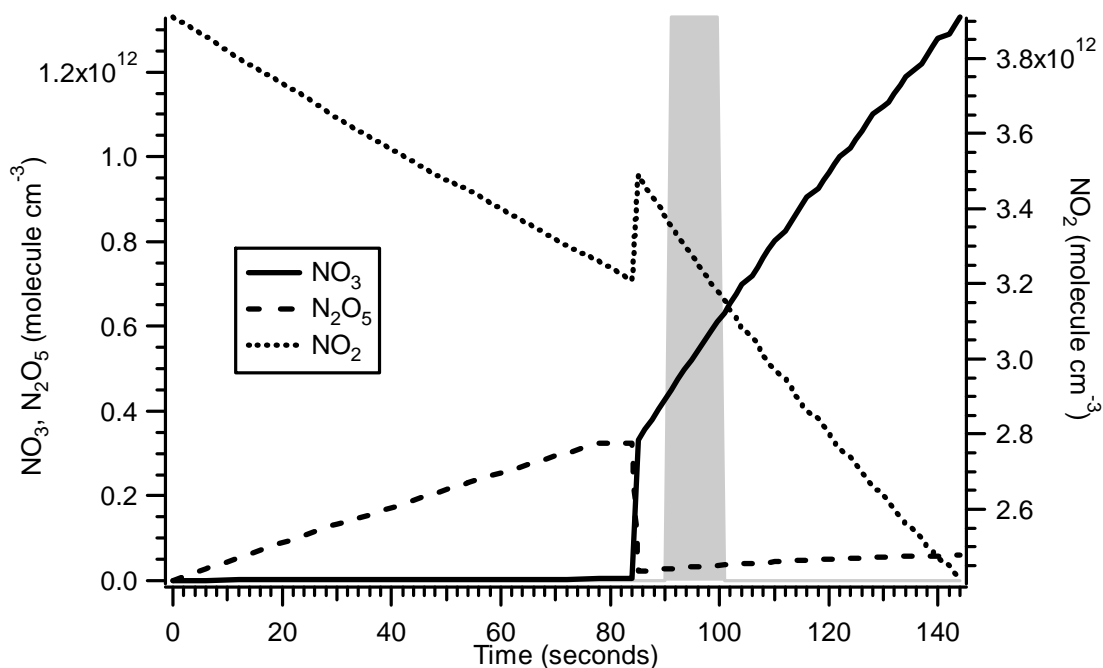


Figure 2-39 Simple AccuChem model for in situ production of N_2O_5 and NO_3 showing mixing at room temperature for the first 84 seconds, followed by heating at 90°C . The cavity residence time is shown by the grey section

In this *in situ* production of NO_3 , the strong absorption signals of the reactants O_3 and NO_2 make this method less than ideal and difficult to quantify. The integrated cavity output often decreased upwards of 50% when the reactants were mixed. Since the Beer-Lambert relationship is non-linear for high optical densities, quantification of the results would be inaccurate. The presence of the additional absorption due to NO_3 when these

two reactants were mixed and sampled in the cavity at higher temperatures was encouraging though as it provides evidence of NO_3 absorbance. It was at this point that research into the synthesis of solid N_2O_5 as a source of NO_3 was investigated.

2.2.10 Cavity Enhanced Absorption Using Solid N_2O_5 as the NO_3 Source

As a stable source of NO_3 , solid N_2O_5 produced from the second method of section 2.2.4 was used. The N_2O_5 trap was stored in an ethanol/dry ice bath at -78.5°C since this bath was the easiest to maintain the temperature, and N_2O_5 has a significant vapour pressure at this temperature. Dried ultrazero air (0.5 – 1 slpm) flowed through the trap (or the trap bypass) directly to the 21 cm cell in the FTIR for quantification. The mixing ratio of the N_2O_5 in the trap flow was typically <1 ppm, which is nearly ten times lower than expected based on the vapour pressure curve from Figure 2-29. Due to the small contact surface area of the N_2O_5 solid, air flowing over the sample may not have adequate time for the solid-vapour equilibrium to be established.

The double dilution system (section 2.2.6) was implemented to dilute the N_2O_5 to the required range for the cavity experiments. The FTIR was used to quantify the N_2O_5 from the trap prior to the first dilution step. Dried ultrazero air was used to double dilute the N_2O_5 flow from the FTIR cell to generate mixing ratios ranging from a few ppb to tens of ppb of NO_3 in the cavity at various cavity temperatures.

Figure 2-40 shows a 40-minute portion of one CEA experiment on Aug. 29, 2006. Several such runs of this nature at various inlet and cavity temperatures (ranging from

room temperature to 100°C) were performed. Each 1 second cavity data point consisted of the average of 64 individual integration points. For each addition of N_2O_5 , an O_3 run (green line) was performed inline to determine the effective pathlength, in the case of Figure 2-40, 24.8 km. The NO_3 mixing ratio (purple line) was calculated using the Beer-Lambert Law with the previously acquired pathlength, and the temperature dependent absorption cross-section of NO_3 . The blue triangles represent the FACSIMILE modeled (Curtis and Sweetenham, 1987) mixing ratio of NO_3 in the cavity based on the quantified N_2O_5 in the FTIR and the dilution factors. The experimentally determined and modeled NO_3 values were both corrected for the temperature dependence of the air density. The model used was a simple model considering only the equilibrium reaction, (R1.6).

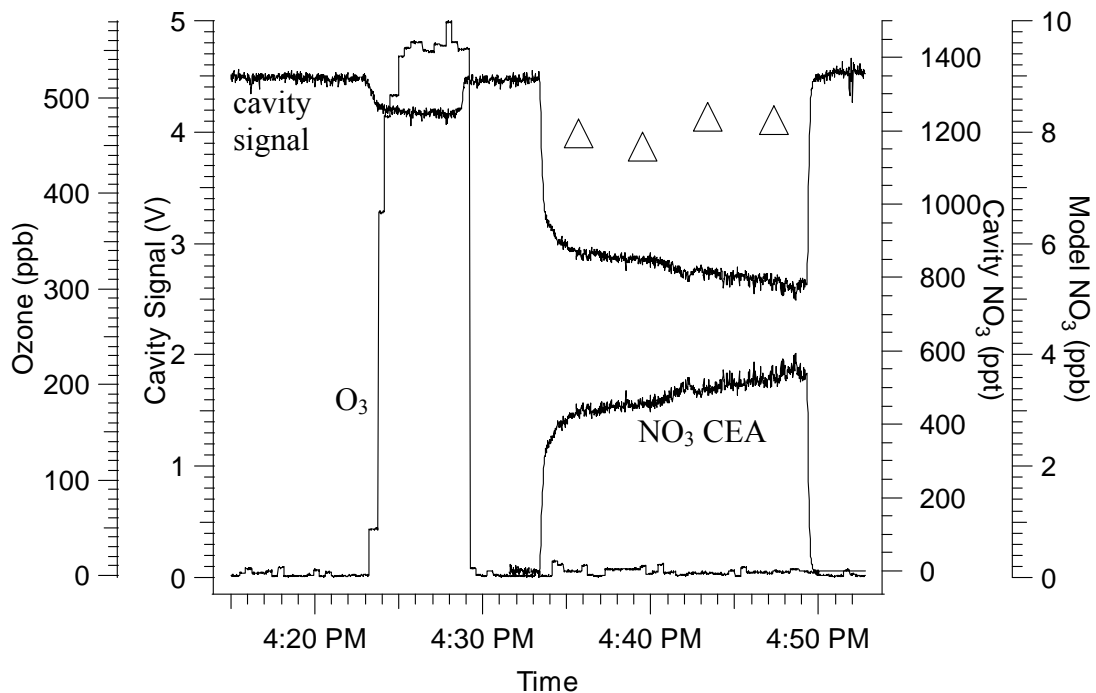


Figure 2-40 Cavity enhanced absorption results for addition of O_3 and solid N_2O_5 sample from Aug. 29, 2006 for a cavity and inlet temperature of 70°C; modeled NO_3 mixing ratio shown as triangles

In order to estimate the NO_3 concentration in the cavity, a series of steps was modeled. The first step involved determination of the NO_3 concentration based on the N_2O_5 thermal equilibrium at room temperature in the FTIR (Figure 2-41). The equilibrium between N_2O_5 and NO_3 and NO_2 is established quickly, well within the residence time of the FTIR. Following this, double dilution resulted in a shift in the $\text{N}_2\text{O}_5/\text{NO}_3$ equilibrium as shown in Figure 2-42. Under these conditions, the time for the sample to reach equilibrium takes about 10 seconds. Although equilibrium was not reached in this step, upon heating of the sample in the last step, the thermal equilibrium dissociates the N_2O_5 nearly completely to NO_3 (Figure 2-43). In the heated cavity, the equilibrium entirely favours NO_3 .

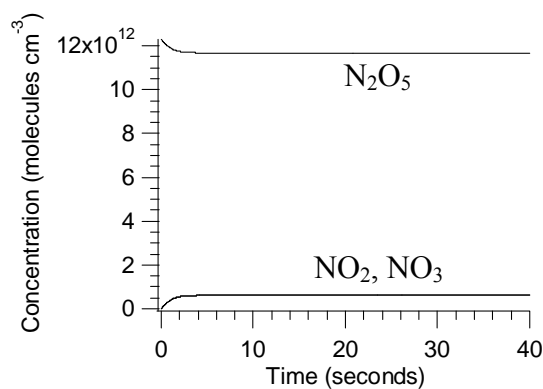


Figure 2-41 Modeled room temperature concentrations of NO_3 , N_2O_5 and NO_2 in the FTIR cell from the N_2O_5 sample. In this case, $\text{NO}_2 = \text{NO}_3$

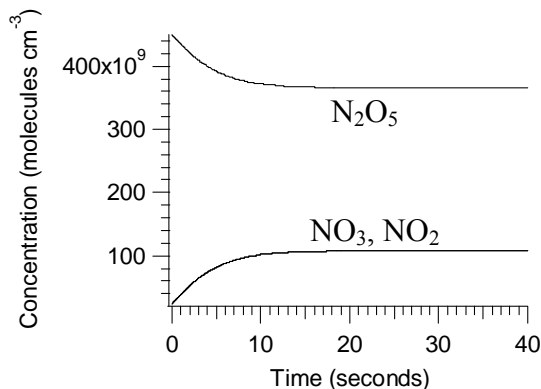


Figure 2-42 Modeled room temperature results after double dilution of N_2O_5 , NO_3 and NO_2 from the solid N_2O_5 source. In this case, $NO_2 = NO_3$

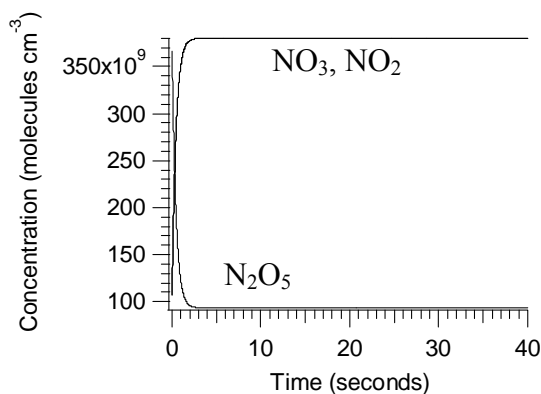


Figure 2-43 Modeled results of N_2O_5 , NO_3 and NO_2 after double dilution and heating to a cavity and inlet temperature of $80^\circ C$ ($NO_3 = NO_2$)

Table 2-2 shows the expected NO_3 mixing ratio based on the model results of the quantified N_2O_5 , and also the calculated NO_3 mixing ratio based on the cavity results for the various runs. From these results the CEA experimentally determined mixing ratios are typically 10 to 100 times too low. There are many possible reasons for this discrepancy. Uncertainty in the laser output wavelength would lead to uncertainty in the absorption cross-section. The laser wavelength was calibrated several times to produce

Date	Cavity Temp. (°C)	Pathlength (km)	Calculated NO ₃ mixing ratio in cavity (ppb)	CEA NO ₃ mixing ratio (ppb)	Ratio of modeled to experimental NO ₃
08/29/06	70	22			
	70	28			
	70	25.2			
	70	24.8	8.1	0.522	16
08/30/06	70	21.7			
	70	28.6	17.5	0.355	49
	70	30.3	10.1	0.210	48
09/01/06	80	33	30	0.753	40
09/06/06	80	36			
	80	24.5	16.3	0.152	107
	80	39.9	22	0.399	55
	80		17.4	0.319	55
	80		13.9	0.194	72
	60	50.7	15.4	0.253	61
	60	30.2	10.2	0.192	53
09/08/06	60	28	26	0.793	33
	60	26.7	15.4	0.547	28
09/13/06	60	35	18.5	0.304	61
	60	32			
	60	30.8			
	60	26.4			
	60	28.7			
09/14/06	60	32.2	19	0.300	63

Table 2-2 Comparison of CEA experiments of heated cavity with model results using N₂O₅ as the NO₃ source

output at the centre of the absorption feature (662 nm). Even considering small fluctuations in the laser wavelength the uncertainty in the absorption cross-section would be small since the absorption feature is very broad (80 cm^{-1}). There may also be other reactions contributing to a loss of NO_3 that were not accounted for in the model. The most likely reaction is reaction of N_2O_5 with H_2O either in the vapour phase or on wet surfaces. P_2O_5 traps were used to remove all water vapour although the vent prior to the cavity was open to the atmosphere and water may have entered the sample lines from there. Due to the potential exposure of the inner walls to atmospheric air, the system was flushed well prior to any NO_3 addition. The slow increase in detected NO_3 as observed in Figure 2-40 may be indicative of a conditioning effect on the walls of the sample inlet and cavity via the conversion of N_2O_5 to HNO_3 with any moisture present on the walls.

Another source for this discrepancy may be due to insufficient mixing in the double dilution setup (Figure 2-32). The first dilution step of the N_2O_5 from the FTIR has a mixing length of less than 10 cm before the draw-off step. Insufficient mixing of the N_2O_5 after the first dilution may result in an overestimation of the modeled NO_3 at the cavity.

As a highly reactive free radical, there is likely significant wall loss in this system (Wayne *et al*, 1991) especially with the long residence times of the sample inlet and the cavity in this configuration. Attempts were made to reduce the residence time in the inlet and cavity sections by increasing the flow rate. Unfortunately, with all tests the cavity output signal became unstable and extremely noisy at higher flow rates. This instability

is possibly due to the onset of turbulence at higher flow rates or vibration of the mirrors. The maximum flow rate through the cavity providing a stable output was 2 - 3 slpm, much lower than the flow rates used by Brown *et al.* (2002a) of approximately 12 slpm.

The table also shows the effective pathlengths based on O₃ absorption. These effective pathlengths are highly variable and often change unpredictably. Since the cavity results depend on the effective pathlength, this calibration must be performed frequently, thereby reducing the time available for sample measurements. The cavity output signal was also prone to occasional drift as was observed in the near-IR (Figure 2-17).

2.2.11 Summary of Results of CEA in the Visible Region

The CEA technique was extended to the visible region for detection of NO₃. The fact that the beam was visible and the cavity output effects could be seen with the naked eye proved to be a valuable diagnostic tool, particularly for alignment purposes. The off-axis alignment procedure did not normally produce the elliptical output pattern or Lissajous figure for astigmatic mirrors as expected. The output patterns were typically characteristic of the TEM_{mn} modes which are also produced from off-axis alignment (Anderson, 1984). Different TEM_{mn} modes have different mirror losses due to diffraction and any inconsistencies of the mirror reflectivity over the mirror surface, leading to a dependence of the pathlength on the alignment as seen in Table 2-2. Because of the dependence on alignment, the system required frequent pathlength calibration.

Regardless, the integrated cavity output did yield stable detected signals, free of any apparent residual mode structure, as the laser wavelength was held constant.

The calibration of the CEA system using NO₂ and O₃ (Figure 2-35 and Figure 2-37, respectively) yielded promising potential detection limits for NO₃ (1.2 ppt ($\alpha = 6 \times 10^{-10} \text{ cm}^{-1}$) and 0.6 ppt ($\alpha = 3 \times 10^{-10} \text{ cm}^{-1}$), respectively) in the absence of sampling losses. One drawback of the CEA technique is that it is not an absolute absorption measurement, and since for a typical measurement there are two unknowns, the concentration and the pathlength, frequent calibration must be performed for determination of the pathlength. This will have an impact on the data acquisition rate.

From the results of the CEA technique using the solid N₂O₅, the experimentally determined NO₃ concentration is much lower than the expected modeled values, indicating a significant loss of NO₃ within the system. As the cavity was unstable at high flow rates, the residence time in the sample inlet and cavity were long, yielding higher sampling losses. To reduce these losses, the inlet and cavity volumes were redesigned as described in the next section, to decrease the residence times at the flow rates required to maintain stability (<2.5 slpm).

3 CAVITY RINGDOWN SPECTROSCOPY FOR NO₃ DETECTION

In order to reduce the dependence on the pathlength calibration required for the CEA measurements, cavity ringdown spectroscopy was applied to the existing instrumentation for the detection of NO₃ using the same continuous wave laser source. One key modification was the addition of the new glass sample inlet and cavity. This new cavity (Figure 3-1), with a single center inlet and dual outlet at the ends allowed for a reduced residence time in the inlet and cavity, although the mirror separation is slightly shorter. In CEA, a steady baseline is critical for obtaining high sensitivity for the NO₃ measurements. Since the ringdown time is independent of fluctuations of the signal intensity through the cavity, the CRD technique has the advantage over traditional absorption techniques.

3.1 Instrument Design

For the NO₃ cavity ringdown experiments, the cavity used in CEA (Figure 2-25) was modified to use a shorter cavity (mirror separation = 43 cm) and a smaller diameter inlet (diameter = 1/2", length = 30 cm) as in Figure 3-1. The volume of the inlet was 14.3 cm³ and the volume of the sample section of the cavity was roughly 172 cm³, giving a residence time of approximately 0.5 and 5.2 seconds, respectively, at 2 slpm. The glassware was coated internally with a fluoropolymer coating (Dupont, Teflon FEP 121A) to reduce wall losses. Laboratory experiments were performed using N₂O₅ as the

NO_3 source in a method similar to that of the CEA double dilution experiments. The length of the $\frac{1}{4}$ " stainless steel tubing from the FTIR to the cavity inlet was minimized and coated with the Teflon coating (Dupont, Teflon FEP 121A) to help minimize losses.

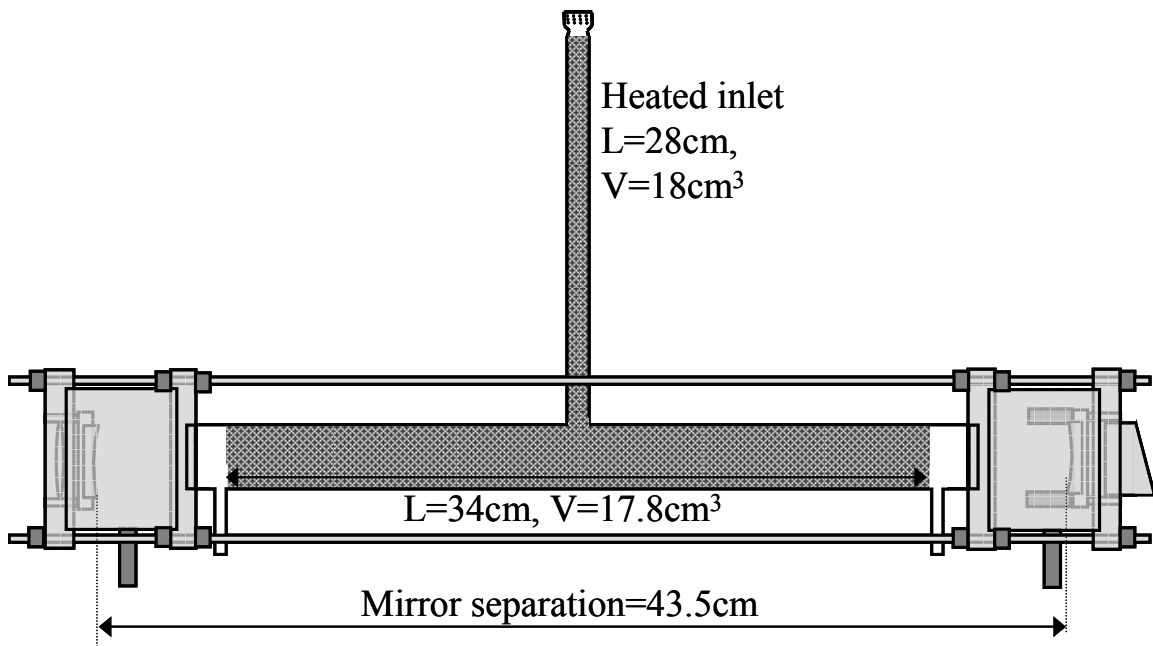


Figure 3-1 *Cavity setup for cavity ringdown experiments. The shaded area is the heated section*

The optical setup for the cavity ringdown experiments was similar to that of the CEA in the visible region, with the addition of a two-lens telescope to achieve mode-matching of the laser to the cavity. Ringdown signals were generated by applying a square-wave modulation from a function generator (Hameg, HM 8030) to the modulation input of the laser controller. The amplitude of the modulation was chosen such that the current applied to the laser was below the laser threshold at the minimum and at the

desired operating current at the maximum, effectively rapidly turning the laser on and off. Unlike the CEA experiments, no other modulation was applied to the laser or to the piezo-electric transducers. A faster detector (Thorlabs, PDA36A) was required to capture the ringdown profiles.

For the data acquisition, a new Labview program was created. The digital trigger from the function generator was sent to the data acquisition card. The falling edge of this signal, coinciding with the immediate shut-off of the laser, triggered the data acquisition of the ringdown signal. The ringdown signal was acquired at 200 kHz (5 μ s per point) for 100 data points. Each ringdown was stored in a buffer and were saved every second at a typical rate of 30 to 100 ringdowns per second. For display purposes, a rough fitting of each ringdown curve to a single exponential was performed and the resulting ringdown time was calculated.

The individual ringdown signals were analyzed offline with another Labview program. To account for the DC offset of the detector, a small DC offset was applied to each point of each ringdown. The first 10 μ s were removed from each ringdown to account for any lag in the triggering. The single exponential fit was calculated from this new initial signal, V_0 , to V_0/e of the ringdown curve to extract the ringdown time, τ , and can be expressed as:

$$V(t) = V_0 \exp\left(-\frac{t}{\tau}\right) + C \quad (\text{E3.1})$$

where $V(t)$ is the signal, in volts, at time, t , V_0 is the initial signal after removal of the first 10 μ s, and C is the DC offset. Additional filtering of each ringdown was applied to

remove any bad events. Ringdown events with very high or very low initial signals were removed to account for possible saturation of the DAQ, or to account for low buildup levels within the cavity. No filtering was applied based on the ringdown times, only the initial signal voltage.

The ringdown times were averaged for one second, and this average and standard deviation, as well as the number of ringdown events were stored as a function of time.

3.2 Laboratory Tests of CRD Applied to NO₃ Detection

3.2.1 Generation and Analysis of Ringdown Signals

To confirm that the ringdowns observed through the cavity were real and not just a function of detection and amplification bandwidth, the ringdown was detected in the absence of the cavity. This detected ringdown time was less than 5 μ s, within the resolution of the data acquisition rate. The detection electronics are thus fast enough for these ringdown measurements.

The cavity was initially aligned by adjustment of the steering mirror such that there was an intense buildup of light within the cavity for each ringdown event and that the initial signal of the ringdown curve was roughly reproducible for each ringdown event, as shown in Figure 3-2. This figure shows the detected cavity output (no longer integrated) from the oscilloscope, for a laser chop rate of 20 Hz. Once the alignment is optimized, there is significant intensity buildup with each chop cycle, and the variability

in the built-up intensity is relatively low. For a situation such as this, the signal immediately following the end of each laser-on cycle resulted in a ringdown decay.

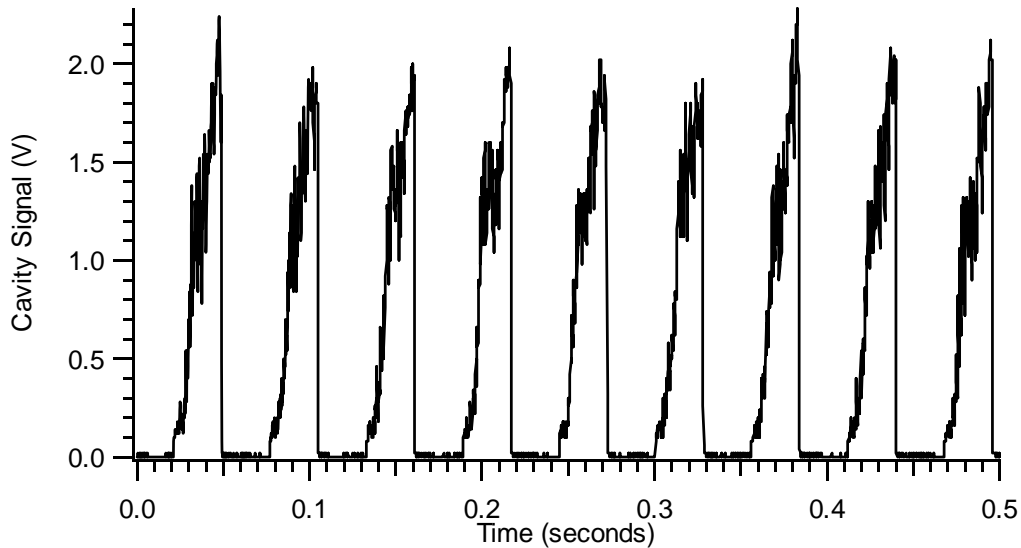


Figure 3-2 Actual detected cavity output signal with laser chop rate of 20 Hz (generating 20 ringdown decays per second)

To achieve reproducible ringdown times and long pathlengths, the alignment was adjusted so that the ringdown time (pathlength) was maximized and its standard deviation minimized. Typically, the standard deviation was the more important parameter since it meant better reproducibility of the ringdown and cavity output. To increase the signal to noise ratio, the frequency of the laser chop rate was maximized without sacrificing the reproducibility so that more ringdown events could be averaged.

Figure 3-3 shows an example of the individual detected cavity ringdown curves for 1 second at a chop rate of 50 Hz (50 ringdowns per second). To account for any

inconsistencies near the beginning and end of the ringdown curves, the curves were fitted from $t=10$ ms to $t=V_{(10ms)}/e$ and is shown by the black section. Each curve was fitted to a single exponential function as defined by equation (E3.1). In this case, additional filtering was applied for ringdown signals with a V_0 below 0.50 V to account for any low detected signals or above 4.8 V, a value just below the saturation voltage of the data acquisition card.

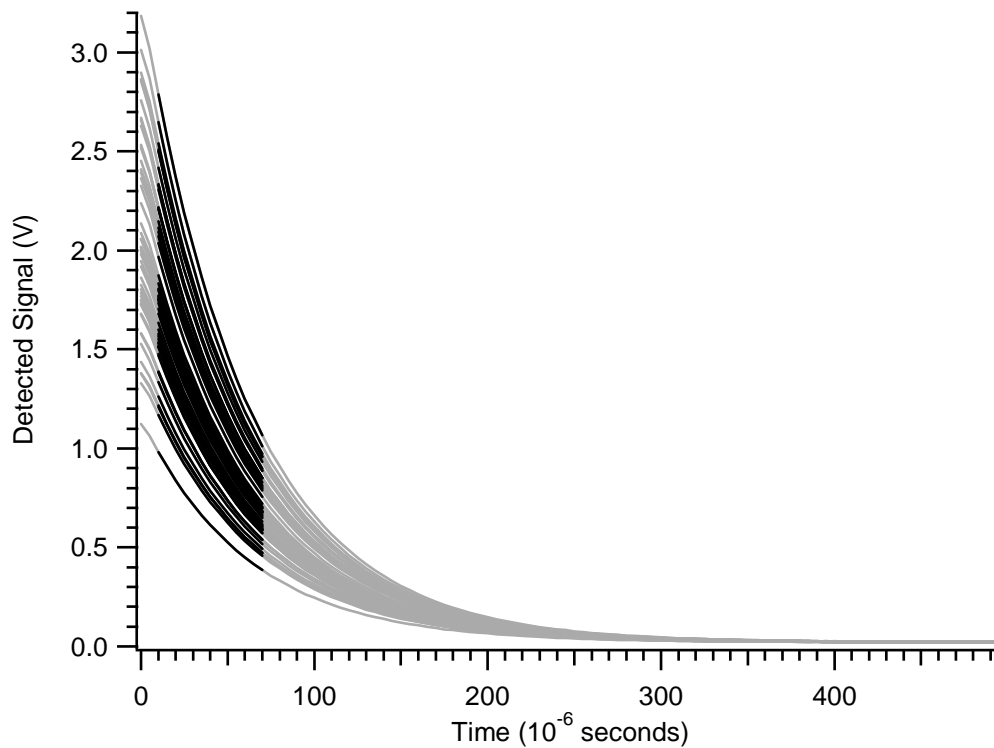


Figure 3-3 Actual detected ringdown signals for 1 second at 50 Hz (50 ringdowns in one second) showing fitted region in black

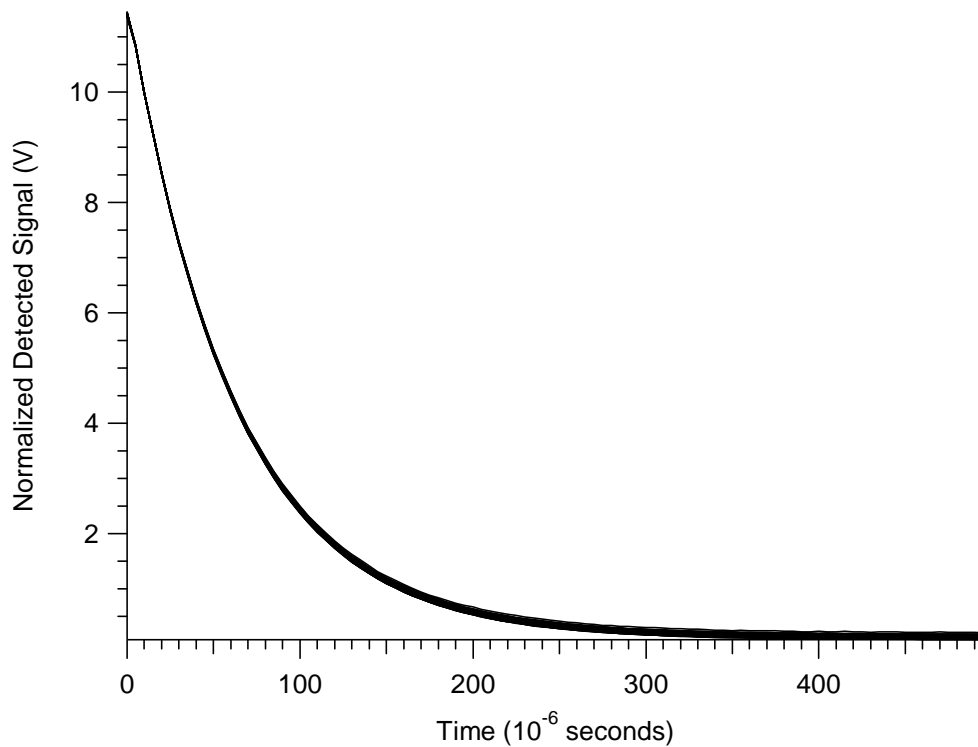


Figure 3-4 Normalized ringdown signals of Figure 3-3 showing independence of ringdown on initial intensity – all ringdowns are nearly identical

3.2.2 Determination of the L/d Factor

Using O₃ as the test gas, the ratio of the mirror separation distance to the effective sample length, L/d, was determined. The mirror cushion gas was considered as a plug flow and thus did not contribute to dilution of the incoming sample. The actual O₃ mixing ratio at the cavity inlet was calculated from the measured O₃ using an O₃ monitor (Dasibi 1003-AH) after the cavity and corrected for dilution. The O₃ mixing ratio was calculated from the ringdown times as in (E1.12) neglecting the L/d factor. The L/d factor was calculated from the ratio of the known mixing ratio of O₃ entering the cavity to

the O₃ mixing ratio determined from analysis of the ringdown times with and without O₃. Several days worth of O₃ experiments were analyzed (more than 60 O₃ additions). The average L/d factor was 1.28, which is consistent with the ratio of the mirror separation distance to the cavity sample dual outlet distance, 1.27 (43 cm/ 33 cm) shown in Figure 3-1.

3.2.3 Comparison of Simultaneous Cavity Ringdown and Integrated Cavity Output

The CRD and CEA techniques were simultaneously compared using O₃ as the test species. The laser was chopped using a function generator and the digital trigger output of the function generator was used as the reference frequency for a lock-in amplifier as well as the trigger for data acquisition. The signal from the detector was split to the acquisition system and the input of the lock-in amplifier (EG & G, 5210). In this manner, the lock-in amplifier is acting in a similar way to the integrator circuit.

Figure 3-5 shows the results of a typical simultaneous CEA and CRD experiment. The 10 second and 5 minute averages of both the ringdown time and lock-in signal are shown as well as the ozone mixing ratio as a function of time. The laser was chopped at 40 Hz. Optimization of the integrated signal for a 1 Hz data acquisition rate required a 300 ms lock-in amplifier time constant. The lock-in data shows the average of 10 data points. It is readily apparent from the figure that the signal-to-noise of the 10 second ringdown signal is much better than that of the lock-in signal. The standard deviation of the 5 minute average ringdown time, s/\sqrt{N} , is approximately 0.01 μ s.

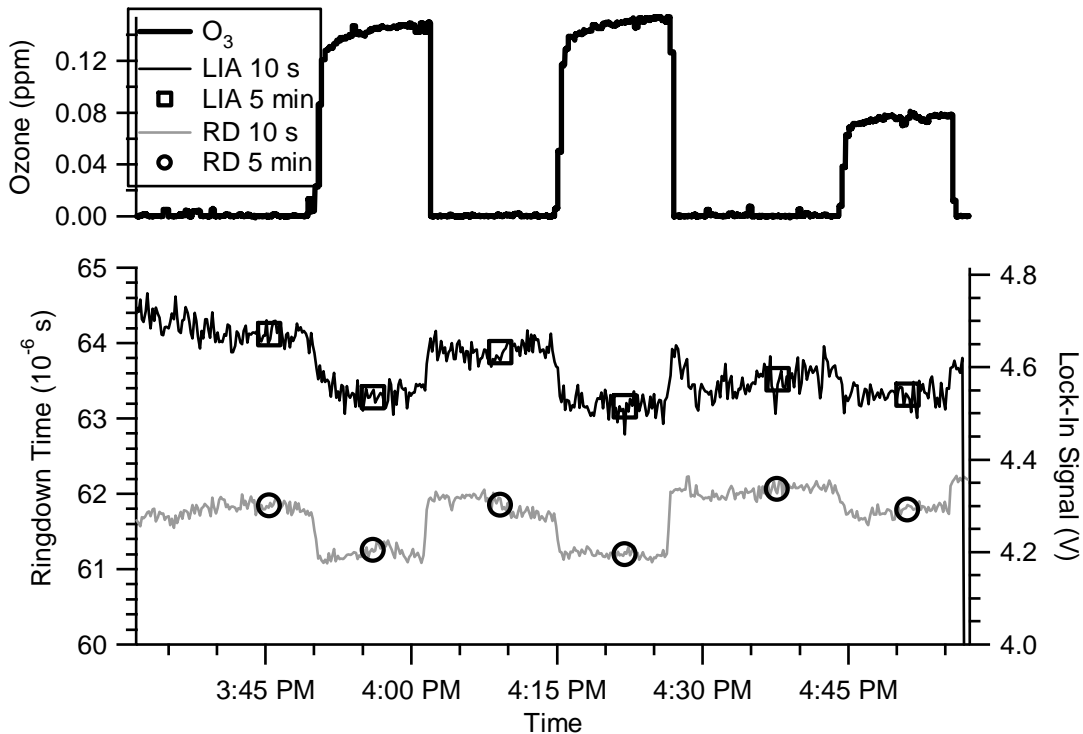


Figure 3-5 Comparison of simultaneous integrated cavity output lock-in detection and cavity ringdown signals for O_3 absorption

For the cavity ringdown experiment, the 1σ detection limit of species X , is given as (Brown *et al.*, 2002b):

$$[X]_{\min} = \frac{1}{c\sigma d} \frac{L \Delta\tau_{\min}}{\tau_0^2} \quad (\text{E3.2})$$

where $\Delta\tau_{\min}$ is the minimum detectable change in ringdown time. For equal averaging times of τ and τ_0 , $\Delta\tau_{\min}$ is determined from the standard deviation of the average multiplied by $\sqrt{2}$. Equation (E3.2) represents a best-case scenario, based on the statistical detection limit, where the uncertainty of the ringdown time in the absence of

absorbers (τ_0) is the largest source of uncertainty. This is analogous to the noise in the background signal. Using (E3.1) with the value of L/d of 1.28, the detection limit for O_3 is 3 ppb, and a minimum detectable absorption coefficient of $1.6 \times 10^{-10} \text{ cm}^{-1}$ for a 5-minute average. This is equivalent to an NO_3 detection limit of 0.3 ppt. Potential sampling losses and other interferences, such as drift and noise created by turbulence, will increase the actual detection limit.

For determination of the detection limit of the lock-in CEA method, since the effective pathlength is not implicitly known, comparison of the signal in the presence of the absorber is compared with the baseline signal without the absorbing species. The 1σ detection limit for O_3 is:

$$O_3(ppb)_{\min} = \frac{O_3(ppb)_{cal}}{-\ln\left(\frac{V}{V_0}\right)_{cal}} \times \frac{L}{d} \times \frac{\sqrt{2}(\sigma(V_0 \text{ mean}))}{V_0} \quad (E3.3)$$

where $O_3(ppb)_{cal}$ is the actual O_3 mixing ratio measured by the O_3 monitor. The first term in the above equation represents the calibration of the CEA technique since the pathlength is not known. The detection limit in this case, for the first O_3 addition in the above figure, is 5.8 ppb. The equivalent detection limit for NO_3 is 0.58 ppt in the absence of sampling losses.

From the above data, the cavity ringdown analysis results in a detection limit better than that for the lock-in CEA results by roughly a factor of 2. Subsequent cavity ringdown experiments resulted in much better detection limits as the reproducibility of the cavity ringdown time increased. Figure 3-6 shows one such experiment with much

better 5 minute standard deviation. In this case, the standard deviation of the 5 minute average is roughly 2×10^{-9} seconds, yielding an O_3 detection limit of 0.6 ppb, approximately 10 times better than that from the CEA method. One factor for the better sensitivity of the ringdown technique is the high data acquisition rate. In CEA, the 5-minute average of the lock-in signal consisted of approximately 270 data points, whereas the 5-minute average of the ringdown signal consisted of roughly $270 \times 40 = 10\,800$ ringdown events. Since the signal-to-noise ratio has a \sqrt{N} dependence, the faster acquisition times associated with CRD resulted in much better detection limits.

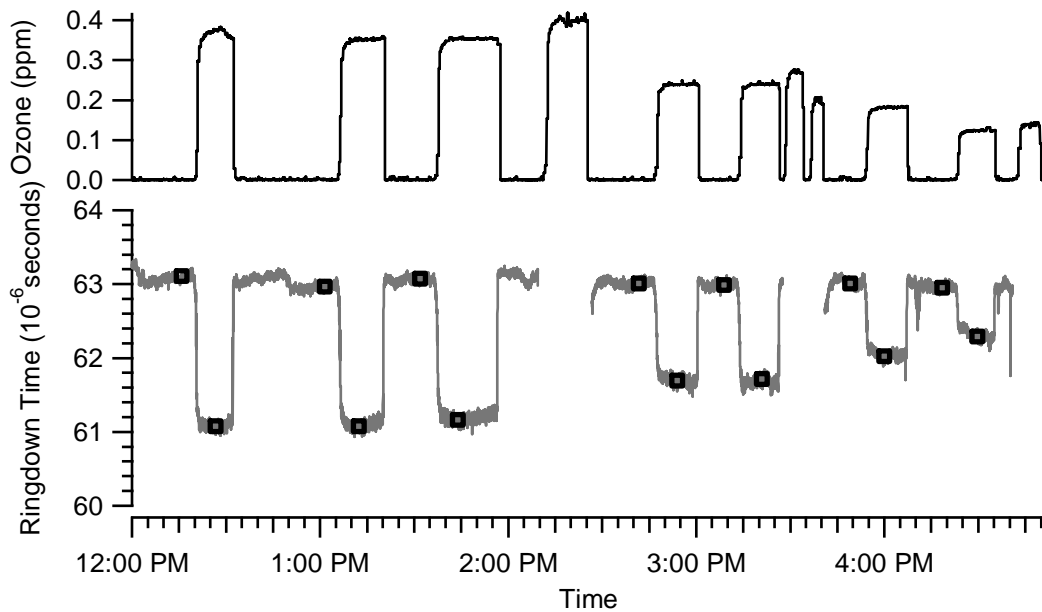


Figure 3-6 Improved cavity ringdown signal for various O_3 additions

As mentioned before, one main drawback of the CEA method is the requirement for frequent effective pathlength calibration, and the uncertainty associated with it. For

the cavity ringdown technique, the pathlength can be calculated from the ringdown time from the empty cavity. For the data from Figure 3-5 the 62 μs ringdown time corresponds to an effective pathlength of 18.6 km. Cavity ringdown can be used in conjunction with the CEA technique for pathlength determination, without the use of a calibration gas (Mazurenka *et al.*, 2005).

3.2.4 Cavity Ringdown Experiments of NO_3

3.2.4.1 Determination of the Wall Loss Constant for NO_3

As seen in Table 2-2, the detected NO_3 mixing ratios were considerably lower than those predicted by the model. This result suggested the possibility of a significant loss mechanism for NO_3 . Considering this loss a first-order wall loss mechanism, the wall loss was estimated by the fitting of modeled data to the experimental CRD data.

The result for an experiment with the cavity and inlet at room temperature is shown in Figure 3-7. The previously described double dilution setup for $\text{N}_2\text{O}_5/\text{NO}_3$ was used to vary the concentrations to the cavity. Using the quantified N_2O_5 from the FTIR cell, the sampling scheme was carefully modeled using Facsimile (Curtis and Sweetenham, 1987) taking into account residence times of the various sections, and dilution factors. The blue diamonds from the figure are the modeled NO_3 concentrations without a wall loss mechanism included. The green diamonds are the modeled results with an average wall loss constant, k_{wall} , of 0.47 s^{-1} . The Gormley-Kennedy equation (Murphy and Fahey, 1987) was applied to determine the diffusion limited wall loss

constant using typical values for the diffusion coefficient ($0.1 \text{ cm}^2 \text{ s}^{-1}$), cross-sectional area of the glass sampling inlet and cavity and flow rates, the diffusion limited wall loss constant is approximately 0.25 s^{-1} . The fact that the experimentally determined wall loss constant of 0.47 s^{-1} is higher than the diffusion limit implies that the wall loss may be increased by turbulence.

The k_{wall} value of 0.47 s^{-1} is significantly higher than that of Brown *et al.* (2002b) and Simpson (2003), who determined wall loss constants of $0.03 \pm 0.02 \text{ s}^{-1}$ and $0.006 \pm 0.004 \text{ s}^{-1}$, respectively. The wall loss constant was determined in Brown *et al.* (2002b) and Simpson (2003) using a movable injector. Brown *et al.* (2002b) varied the injector position along a small initial portion of the inlet and not the whole inlet and cavity, while Simpson (2003) used a separate similarly sized and coated tube prior to the cavity inlet. Since the injector position was varied along only a straight, short initial portion of the inlet and not the whole inlet and cavity it is possible that the effective wall loss constant was underestimated since the various bends in the tubing would not be considered. From a review of various nitrate radical kinetic experiments using flow tubes of similar dimensions but at reduced pressures (Wayne *et al.*, 1991), the value for k_w was generally accepted to be small, $<0.5 \text{ s}^{-1}$. Under these conditions of low pressure, diffusion will be higher. Although the value for k_{wall} from Wayne *et al.* (1991) is consistent with that determined experimentally in this research, due to the lower diffusion in this setup at atmospheric pressure, the wall loss constant could be improved

dramatically. Regardless, this wall loss constant is much smaller than that for the hydroxyl radical, OH, with a k_w of $10 - 30 \text{ s}^{-1}$ (Wayne *et al.*, 1991).

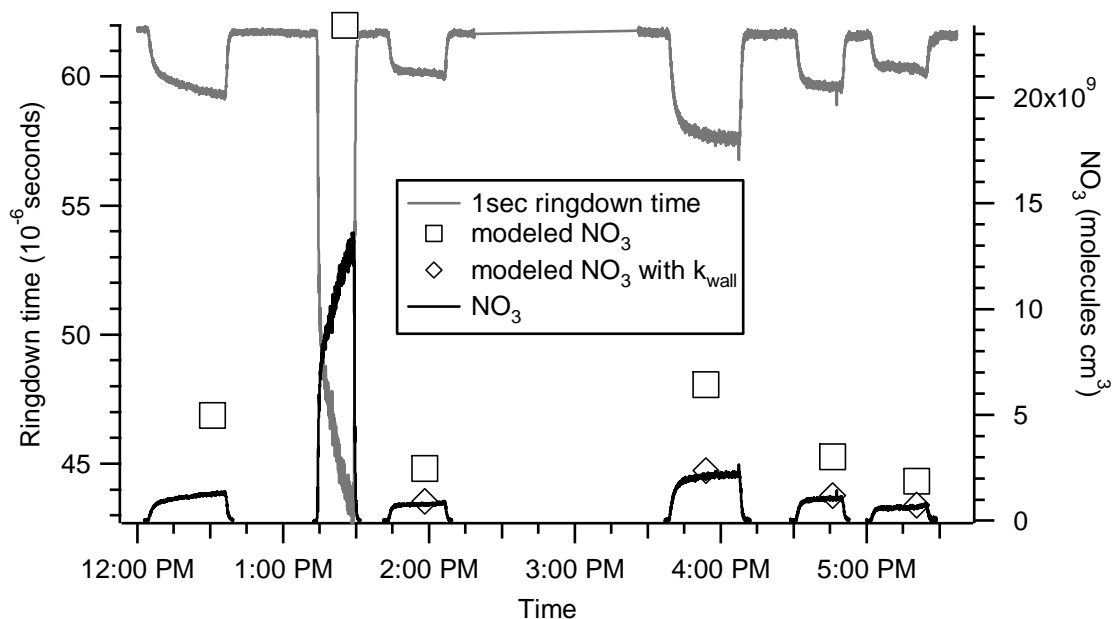


Figure 3-7 Ringdown results of various additions of NO_3 from solid N_2O_5 source over time with sample inlet and cavity at room temperature – comparison of experimental and modeled NO_3 concentrations for determination of wall loss constant

There are several possible reasons for this discrepancy. These calculations are based on the N_2O_5 concentrations in the FTIR. Although the tubing length was minimized, there may be more losses within the stainless steel section from the FTIR cell to the cavity inlet. Therefore, the concentrations reaching the cavity may have been lower than that used in the model. Although a fluoropolymer coating was applied to reduce wall losses, the coating may not have been applied evenly. For sections that may not have been coated iron oxides may have been produced such as those observed on the inlet and outlet connectors of the stainless steel FTIR cell. In addition, the flow dynamics

may have influenced the wall loss constant. The flows may have been turbulent, particularly at the inlet to cavity 90° connection. Considering these possible loss mechanisms, the determined wall loss constant is overestimated and thus can be considered an upper limit. Compared to the previous results of the CEA experiment with the previous sampling scheme the total NO₃ loss decreased dramatically from a factor of roughly 10 – 50 times for the CEA experiments (Table 2-2) to roughly 2 – 3 times for the ringdown setup, due to the reduced residence time in the inlet and cavity.

3.2.4.2 Temperature Dependence on the NO₃ Losses

The cavity ringdown experiments of the N₂O₅ sample were repeated at various inlet and cavity temperatures to investigate the temperature dependence of the NO₃ wall loss. For the various runs at different temperatures, similar dilution factors were used to allow comparison at different temperatures with similar initial concentrations. The results of the heated cavity experiments for 60°C, 90°C, and 105°C are shown in Figure 3-8, Figure 3-9 and Figure 3-10, respectively. The figures show the resulting NO₃ concentration based on the ringdown times obtained using the temperature-dependent absorption cross-section as described previously.

From these figures, there appears to be a conditioning effect that requires long times for the NO₃ to reach a maximum in the cavity. This is evident in the first two N₂O₅ additions of Figure 3-8 and Figure 3-9. These two additions were performed using the same flow conditions, with the N₂O₅ bypass opened and the trap closed for several

minutes and then reopened. The cavity signal continues where it left off which suggests a potential conditioning effect.

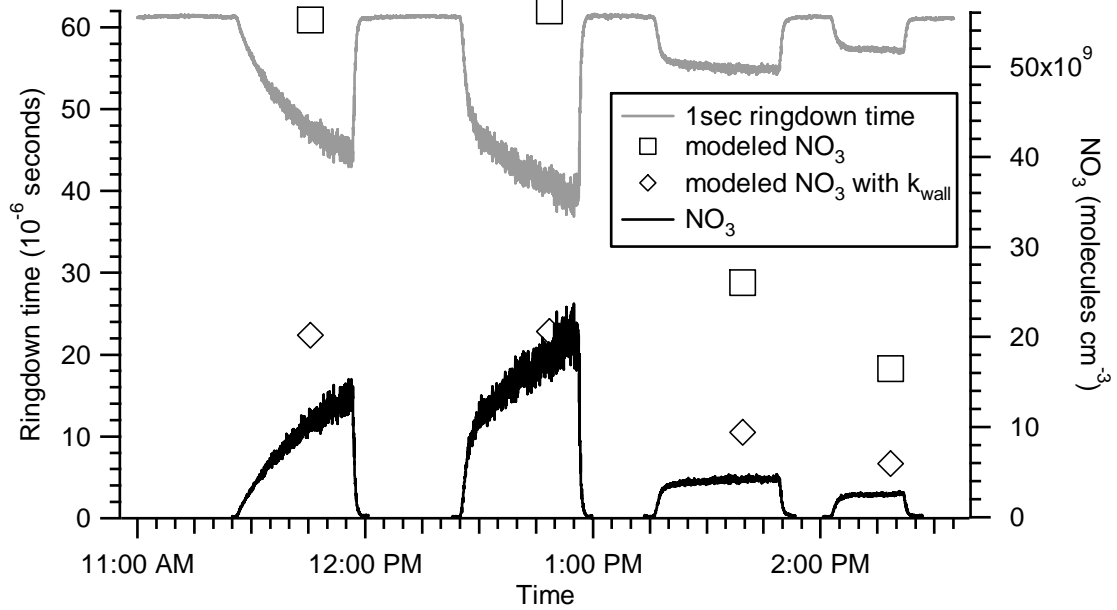


Figure 3-8 CRD experiment of variable additions of N_2O_5 as NO_3 source over time at an inlet and cavity temperature of $70^\circ C$ – comparison of experimental and modeled NO_3 concentrations

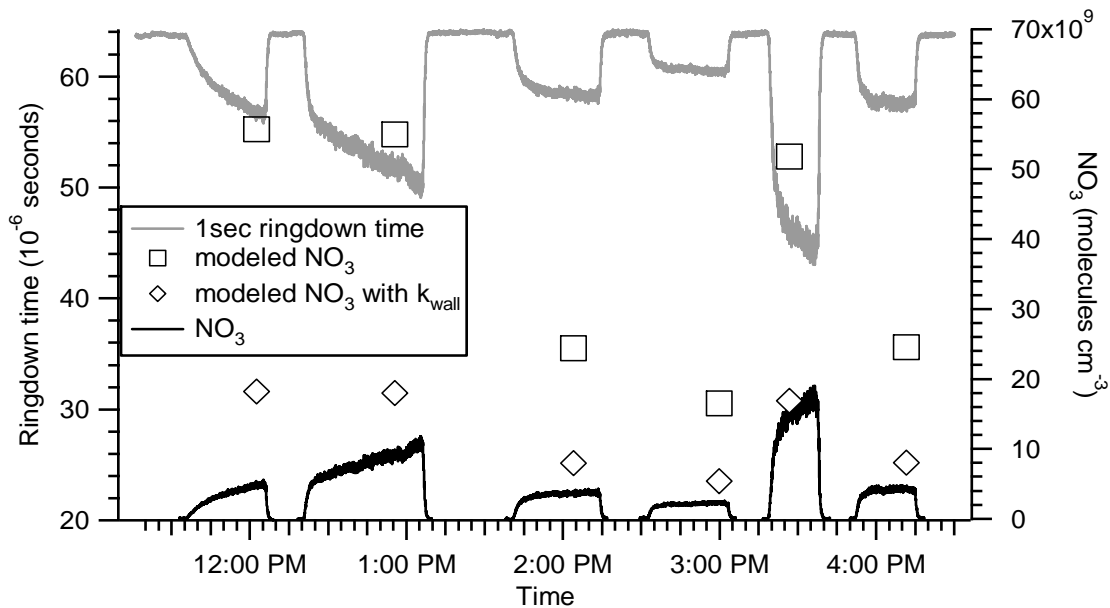


Figure 3-9 CRD experiment of variable additions of N_2O_5 as NO_3 source over time at inlet and cavity temperature of $90^\circ C$ – comparison of experimental and modeled NO_3 concentrations

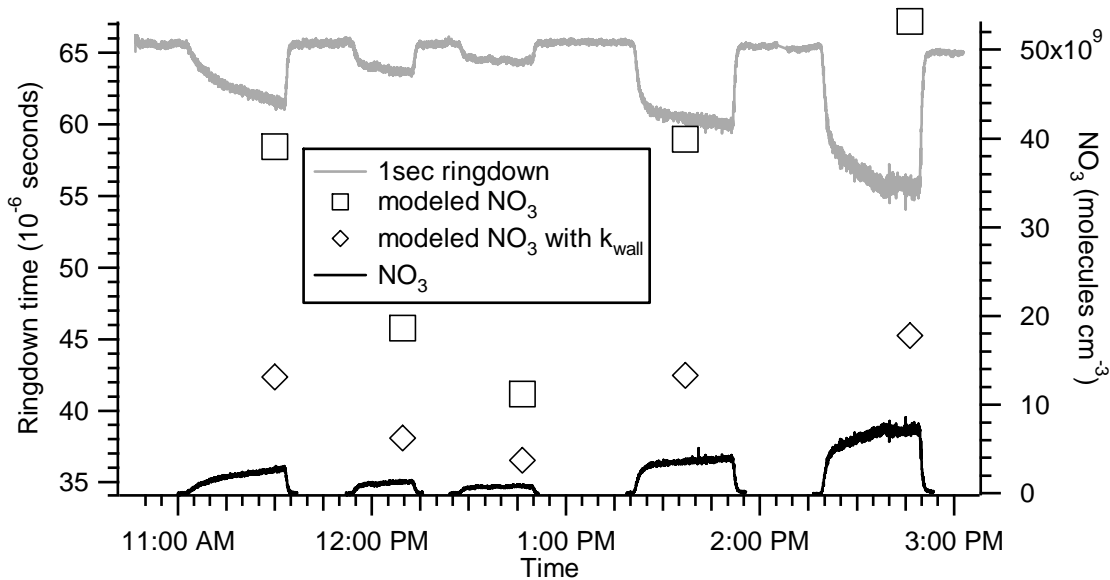


Figure 3-10 CRD experiment of variable additions of N_2O_5 as NO_3 source over time at inlet and cavity temperature of $105^\circ C$ – comparison of experimental and modeled NO_3 concentrations

The modeled results are based on the quantified N_2O_5 from the FTIR, and the various dilution factors shown both with and without the wall loss constant determined previously. The residence times for the various sections have been corrected for the temperature dependence of the density of air. From these figures, it is also apparent that the experimental results are consistently lower than the modeled results for elevated temperatures. As the temperature increases, this effect also increases. The correlation between the experimentally determined NO_3 and the modeled NO_3 using the room temperature wall loss constant is shown in Figure 3-11. Even with the large room temperature wall loss constant (0.47 s^{-1}), the losses are still underestimated for elevated temperatures.

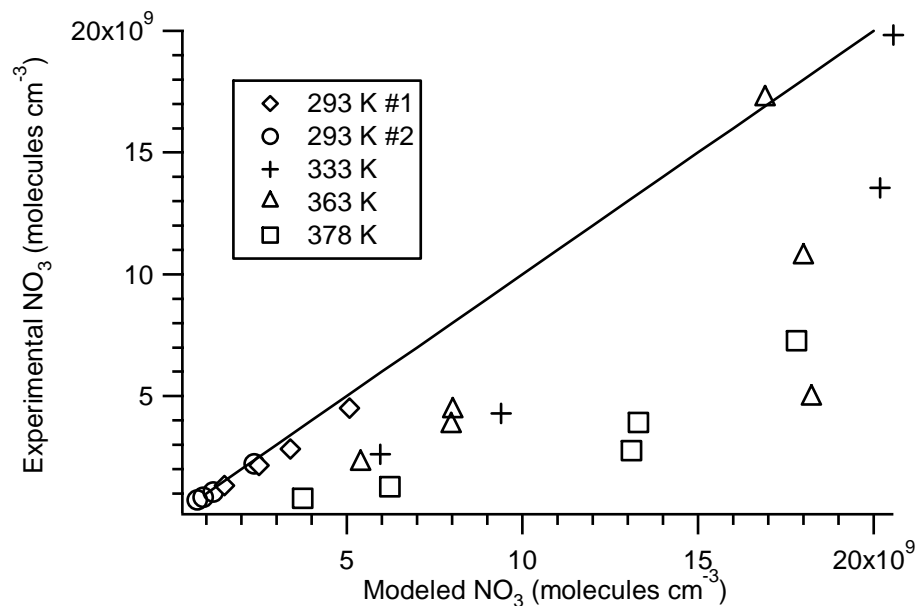


Figure 3-11 Comparison of experimentally determined NO_3 concentration with modeled NO_3 for various cavity temperatures; 1:1 ratio shown by the diagonal line (note the error bars, determined from (E3.2), are not shown here as they are within the size of the points)

This consistent overestimation of the modeled NO_3 compared to the experimentally determined NO_3 suggests another loss mechanism at higher temperatures. Johnston *et al.* (1986) have suggested a thermal decomposition mechanism of NO_3 to produce NO and O_2 (R1.10). The formation of NO from this proposed mechanism increases the availability of NO for the titration of NO_3 by reaction (R1.4). There has been some dispute over the relevancy of this mechanism. Russell *et al.* (1986) applied this thermal decomposition mechanism to NO_3 DOAS measurements in a hot, dry desert environment (Platt *et al.*, 1984). In this environment, the thermal decomposition reaction would provide the main loss mechanism. From their analysis, modeled NO_3 mixing ratios including the thermal loss mechanism consistently predicted results that were substantially lower than measured except under conditions of high relative humidity. Russell *et al.* (1986) suggested that the NO_3 loss was likely due to hydrolysis of NO_3 or N_2O_5 .

In addition, in recent cavity ringdown experiments for the detection of NO_3 and N_2O_5 detection, this thermal decomposition mechanism is not considered. Figure 3-12 shows the effect of experimentally determined NO_3 concentration as a function of temperature (Brown *et al.*, 2002a). For their laboratory experiments of N_2O_5 they normalized the NO_3 concentration to the maximum observed as they did not quantify the N_2O_5 prior to introduction to the cavity. From this figure, it appears that there may be a small additional loss at temperatures above 70°C . Brown *et al.* (2002a) described this loss as a temperature dependent surface loss.

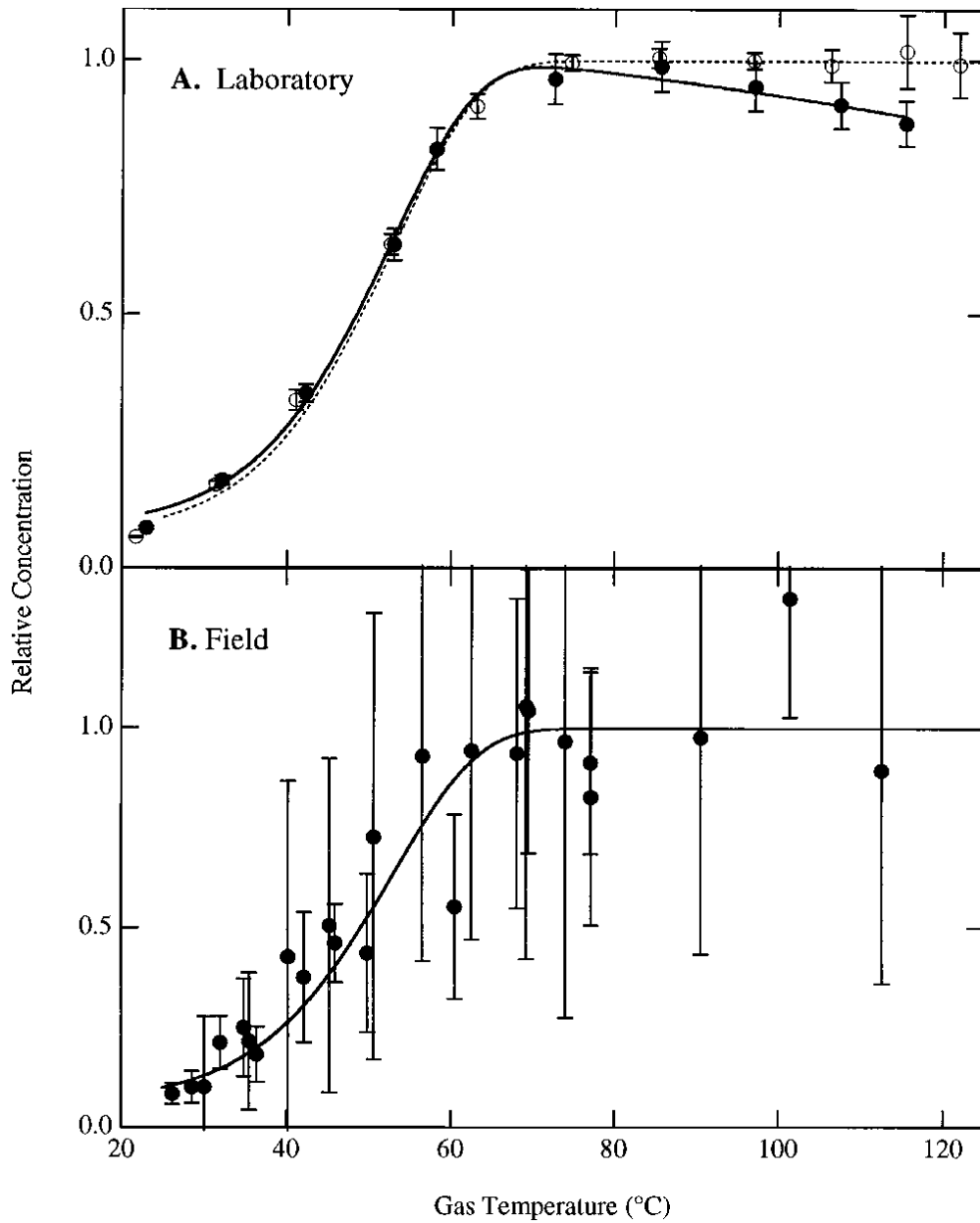


Figure 3-12 *Normalized NO₃ concentration as a function of temperature from Brown et al. (2002a)*

The unimolecular decomposition of NO₃ reaction was added to the model and compared to the experimental results at elevated temperatures in Figure 3-13.

Comparison of this figure with the correlation plot of Figure 3-11 in the absence of thermal decomposition shows that the thermal decomposition mechanism yields values closer to the measured values. However, additional loss mechanisms are still unaccounted for. The additional losses can be explained by a temperature dependent surface loss. As shown in the previous section, k_{wall} was roughly 2 times higher than the diffusion limited wall loss constant. Since this implies that the wall loss is increased by turbulence, the wall loss constant would be higher at higher temperatures as turbulence increases with higher temperatures. At higher temperatures, the rate of diffusion increases, increasing the interaction with the walls. The diffusion coefficient varies with temperature as $T^{1.5}$ (Atkins, 1982). The magnitude of the wall loss effect will be partially compensated at higher temperatures since the residence time decreases at higher temperatures. Since a mass flow controller was used and the mass flow rate was held constant, the volume flow rate increases at higher temperatures since the density of the gas is inversely proportional to T .

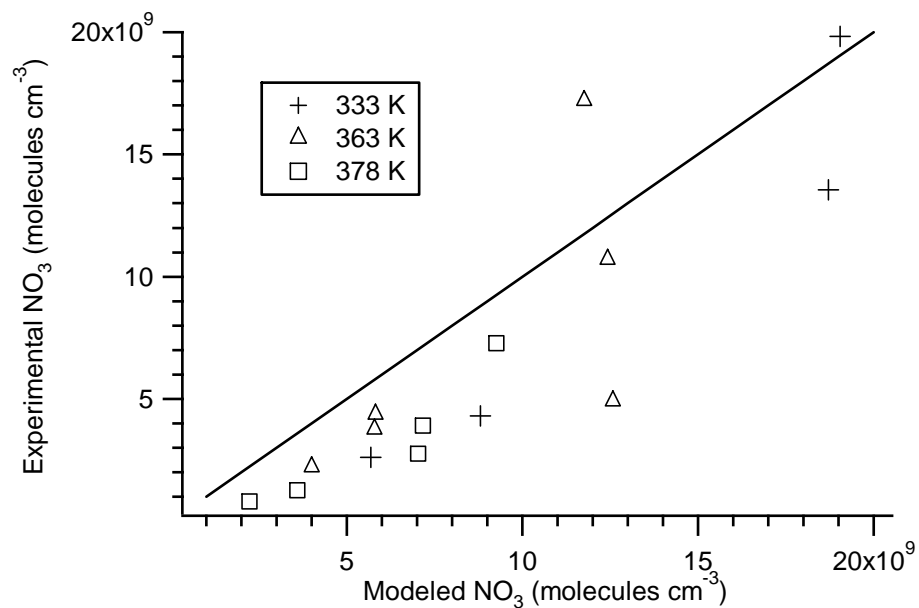


Figure 3-13 Comparison of experimentally determined NO₃ concentration with modeled NO₃ including thermal decomposition for various cavity temperatures; 1:1 ratio shown by the diagonal line (note the error bars, determined from (E3.2, are not shown here as they are within the size of the data points)

Figure 3-14 shows the experimentally determined NO₃ concentrations as a function of inlet and cavity temperature for identical initial N₂O₅ concentrations, a plot similar to Figure 3-12. From the Figure 3-14, the experimentally determined NO₃ is at a maximum at an inlet and cavity temperature of 333 K (60°C). As the temperature increases, the experimentally determined NO₃ decreases. From this plot, the optimum temperature for conversion of N₂O₅ to NO₃ with minimal losses is around 60°C to 80°C.

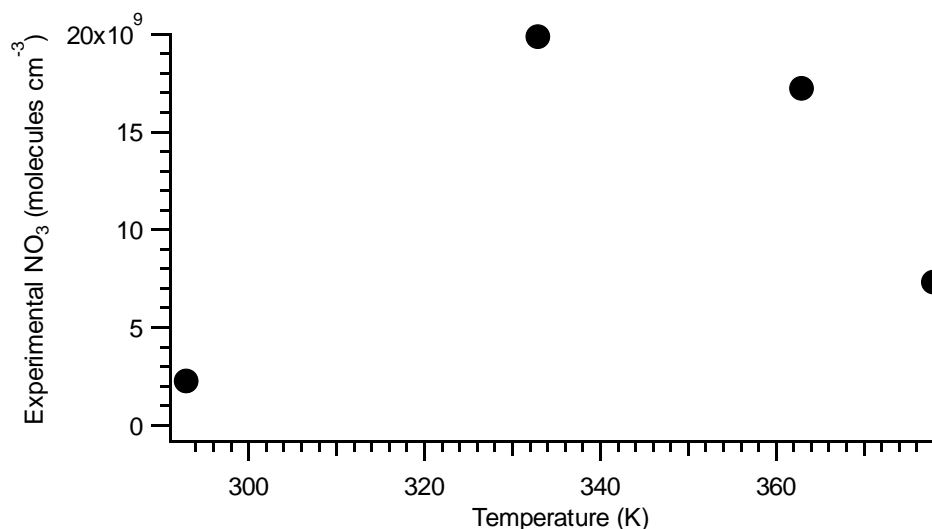


Figure 3-14 *Effect of inlet and cavity temperature on experimentally determined NO₃ for similar initial N₂O₅ conditions*

3.2.4.3 NO Titration of NO₃

In cavity ringdown spectroscopy, the ringdown times in the presence (τ) and absence (τ_0) of the absorber, are required for determination of the concentration of the desired species. Traditionally, the sample air is replaced with zero air to determine τ_0 . In addition to the removal of the species of interest, this method generally removes all possible species contributing to the absorbance. A better method for obtaining the background signal is through the selective removal of the species of interest. In the case of NO₃, titration reaction with NO (R1.4) to form two molecules of NO₂ presents an excellent method for the determination of τ_0 .

For a chemical titration background determination to be of use, fast reaction times are required and it must be selective towards the species of interest. The rate constant for

the titration of NO₃ with NO, $2.6 \times 10^{-11} \text{ cm}^3 \text{ molecule}^{-1} \text{ s}^{-1}$ at 298 K, yields very fast reaction times. For example, for 50 ppt NO₃ and 40 ppb NO, the NO₃ is completely removed (>99%) in roughly 0.2 seconds, well within the inlet residence time of 0.5 seconds. For high O₃, the reaction of NO and O₃ to produce NO₂ (R1.5) with a rate constant of $1.9 \times 10^{-14} \text{ cm}^3 \text{ molecule}^{-1} \text{ s}^{-1}$ at 298 K can contribute an absorption to the baseline signal due to the production of NO₂, which has an absorption cross-section roughly double that of O₃. If the O₃ mixing ratio is known, this small effect can be corrected for if necessary.

Laboratory tests of the addition of NO to the NO₃ sample were performed to ensure that 1) the absorption signal observed in the cavity experiments was indeed due to NO₃, and 2) the NO₃ titration with NO is an effective method for determining the baseline signal. An example of the addition of NO to the cavity ringdown signal for addition of the NO₃ sample to the room temperature cavity and inlet is shown in Figure 3-15.

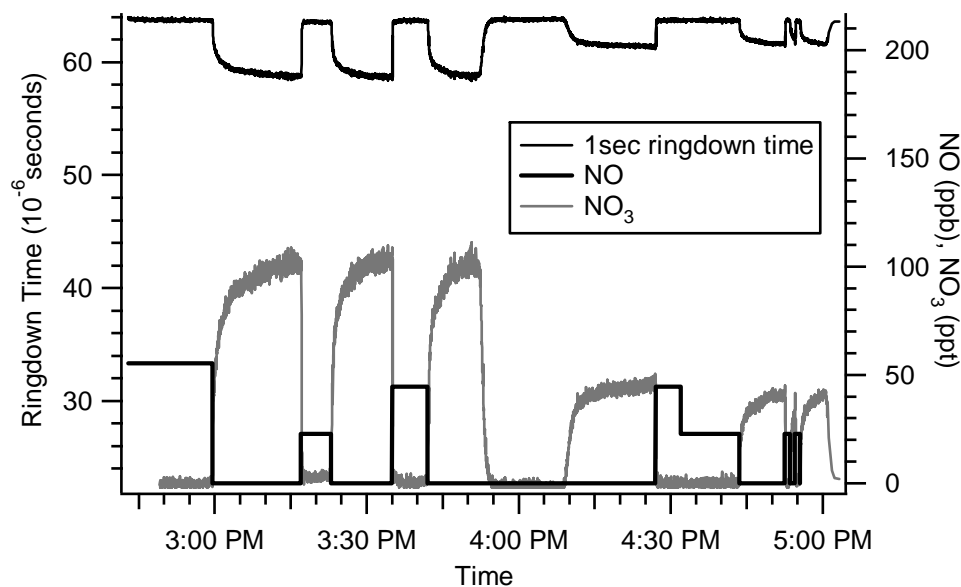


Figure 3-15 Ringdown experiment with addition of NO to room temperature inlet and cavity to effectively titrate NO₃ from the N₂O₅ solid source

From the figure, it is evident that the cavity absorption is due to NO₃ by the effect of addition of NO. The NO₃ is essentially titrated immediately upon addition of NO even for these small amounts of NO added. There is some variation around zero of the NO₃ mixing ratio when the NO is added. This variation is attributed to the slight drifts observed in the cavity over time. The slight dilution of the sample as NO is added does not affect the experimentally determined NO₃ since sufficient NO is added to fully titrate the NO₃. The NO₃ mixing ratio was determined using the average τ_0 for the 5 minute period prior to the experiment. In a typical experiment, τ_0 would be obtained more frequently, and for each NO addition.

To assess the validity of the NO titration background determination, the effect of NO addition to NO₃ was modeled using typical ambient mixing ratios. Figure 3-15 shows the result of addition of 50 ppb NO to 10 ppt NO₃ at room temperature. The NO₃ is essentially removed (~95%) in less than 0.3 seconds, well within the typical inlet residence time (~0.5 seconds at 2 slpm).

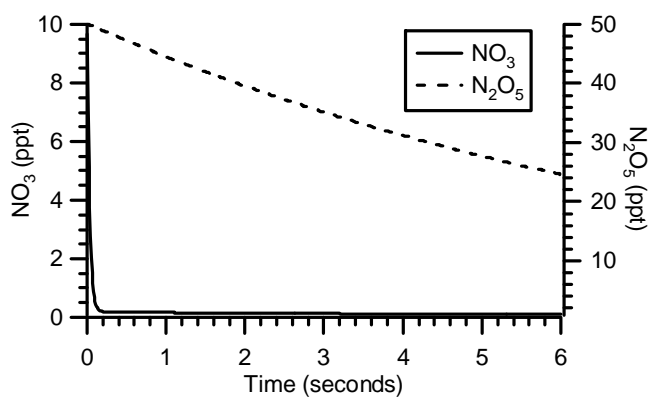
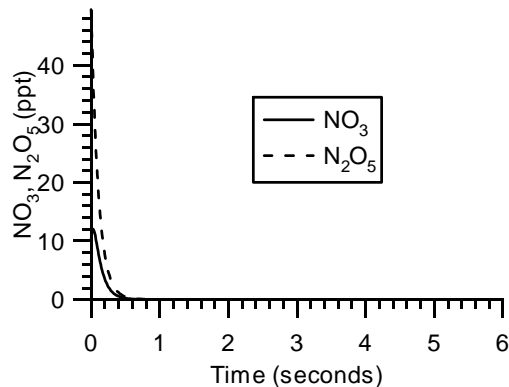


Figure 3-16 Simulation of addition of 50 ppb NO to ambient room temperature air ($NO_3 = 10$ ppt, $N_2O_5 = 50$ ppt)

Figure 3-17 shows the effect of NO titration for measurements of N₂O₅ + NO₃ at 353 K. Under these conditions, both the NO₃ and N₂O₅ are removed completely (>99%) within 0.4 seconds. Based on these simulations, as well as the laboratory experiments, titration of NO₃ with NO is a valid method for background determination.



**Figure 3-17 Simulation of addition of 50 ppb NO to heated air at 353 K
(NO₃ = 10 ppt, N₂O₅ = 50 ppt)**

3.2.4.4 Characterization of Potential Spectroscopic Interferences

Although the chemical titration method of NO₃ with NO is fairly selective towards NO₃, there are potential interferences in an ambient setting if either the sampled O₃ or NO₂ mixing ratios are different for the background and ambient determinations. Potential sources of interference arise from the possibility of the presence of NO₂ in the NO addition source and reactions to either form or destroy the interfering species, NO₂ and O₃.

The NO cylinder was tested for the presence of NO₂ using an LMA3 (Scintrex Unisearch) chemiluminescence detector. The mixing ratio of NO₂ in the NO cylinder was found to be 2.5 ppb. Since the NO cylinder is diluted by a factor of 100-1000 times to produce the desired NO mixing ratios, the equivalent NO₂ added with the NO would be small (<30 ppt) and thus does not require correction.

Under ambient conditions, the reaction of $\text{NO} + \text{O}_3 \rightarrow \text{NO}_2 + \text{O}_2$ (R1.5) can contribute to a small absorbance from NO_2 during the NO addition τ_0 determination. The magnitude of this interference in the background measurement is dependent on the ambient O_3 mixing ratio, the NO titration mixing ratio, and the residence time. This results in a negative interference of the measured NO_3 mixing ratio yielding lower detected NO_3 mixing ratios than are actually present. The measured NO_3 data was corrected using the rate constant, the known NO titration mixing ratio and ambient O_3 . Since the O_3 lost is equal to the NO_2 produced by this reaction, and both species absorb at 662 nm, the interference depends on the ratio of their respective absorption cross-sections with respect to NO_3 . The equivalent NO_3 mixing ratio, $\text{NO}_{3\text{eq}}$ from the formation of NO_2 is:

$$[\text{NO}]_{3\text{eq}} = \frac{\sigma_{\text{NO}_2} [\text{NO}_2]_{\text{prod}}}{\sigma_{\text{NO}_3}} - \frac{\sigma_{\text{O}_3} [\text{NO}_2]_{\text{prod}}}{\sigma_{\text{NO}_3}} \quad (\text{E3.4})$$

Due to the approximately 5 second residence time within the cavity, this correction will be significant under conditions of high ozone, and with the addition of high concentrations of NO as the titrant. For example, the equivalent NO_3 interference for the addition of 40 ppb NO to 35 ppb ambient O_3 is 0.3 ppt.

The reaction of NO with O_2 to produce NO_2 is another possible source of background interference. However, with a rate constant of $2 \times 10^{-38} \text{ cm}^6 \text{ molecule}^{-2} \text{ s}^{-1}$ (Tsukahara *et al.*, 1999) at 298 K, the reaction is typically too slow to be of significance, unless air contamination of the NO lines occurred. The NO in N_2 line was flushed at high flow rates (several lpm) prior to use so this reaction is unlikely to cause an interference.

4 CONTINUOUS-WAVE CAVITY RINGDOWN AMBIENT STUDY OF NO₃

The laboratory tests of the CW-CRD setup resulted in an optical detection limit of <0.5 ppt, showing potentially sufficient sensitivity for ambient measurements of NO₃. The instrument was adapted for portability for ambient measurements of NO₃ and N₂O₅. The first tests occurred on the rooftop of Parking Structure 2 at York University during July and August of the summer of 2007. The scheduling of nighttime measurements was dependent on meteorological conditions. Since the instrument was placed outside and sampled directly from the air, measurements did not take place on nights with precipitation, as the instrumental components would be affected by moisture. In addition, it was expected that during precipitation, NO₃ would be negligible due to the heterogeneous reaction of N₂O₅ with water, (R1.8).

4.1.1 Portable Cavity Ringdown Setup for Ambient NO₃ and N₂O₅ Measurements

For the measurements in the field the laser and optical components were mounted on a 4' × 1' × ½" aluminum breadboard. The optical layout is shown in Figure 4-1.

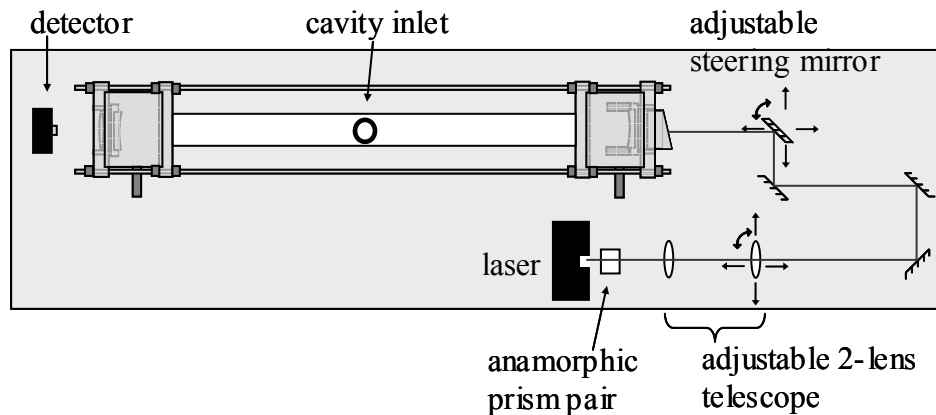


Figure 4-1 Compact optical setup on breadboard for ambient measurements

The breadboard was placed on a 4' × 2' plywood board attached to a wheeled wooden shelving unit. To provide some vibrational isolation, 1" thick foam discs were placed between the tabletop and the breadboard for stabilization. All electronic components were mounted in the shelving unit. The optical breadboard was covered by removable wooden panels to prevent turbulence due to wind, provide protection from the elements, limit the amount of ambient light on the detector, and block any scatter from the laser. The cavity inlet extended approximately 2" above the top cover.

The gas handling setup is shown in Figure 4-2. The cavity total flow rate was 2 slpm, with the mirror cushion gas at 100 sccm so the ambient air was sampled at roughly 1900 sccm. The air was filtered through a 47 mm diameter Zefluor disk filter with a 1 μm pore size (Pall). Variable flows of NO (0 – 20 sccm) were added to the ambient flow prior to the filter to remove the NO₃ and provide the background signal. To reduce the residence time for low NO flows, a short length of 1/8" tubing was used and extended

into the center of the ambient flow to ensure proper mixing of the NO flow with the sample air. Typical NO mixing ratios ranged from 40 to 200 ppb after mixing. To reduce pressure buildup in the NO line, the flow was diverted to a long exhaust line when not being added to the cavity. For some experiments, a small flow of N₂ was added to the NO addition line. This N₂ flow was used to reduce the residence time of the NO addition and to ensure the NO is flushed before the ambient measurement phase. The solenoid valve and flow controllers for the NO and N₂ dilution addition were placed as close to the inlet as possible to minimize flush times.

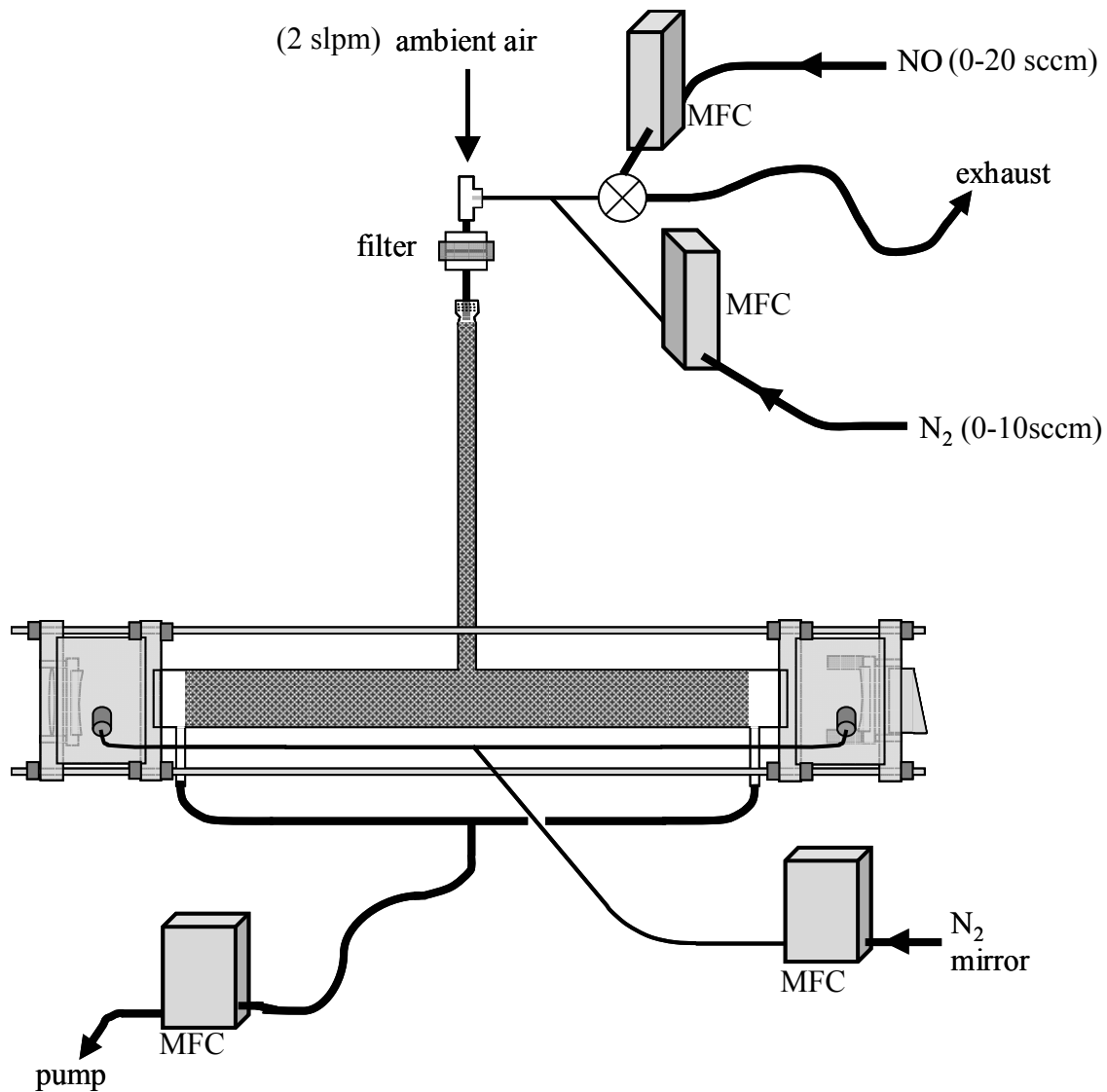


Figure 4-2 Flow system for ambient CRD measurements of NO_3

The system was aligned and the signal optimized as discussed in section 3.2.1 and allowed to run automatically, with a typical NO on/off time of 2/2 minutes. The ringdown events were stored and analyzed offline. The ringdown time for each valve cycle was averaged for 90 seconds, excluding the first 30 seconds of the 2 minute cycle

to account for flushing. For each ambient measurement (NO off, τ), the averaged ringdown time for the backgrounds (NO on, τ_0) before and after each ambient measurement were calculated. The NO_3 concentration for each ambient measurement was then determined from (E1.12):

$$[\text{NO}_3] = \frac{1}{c\sigma} \frac{L}{d} \left(\frac{1}{\tau} - \frac{1}{\tau_0} \right) \quad (\text{E4.1})$$

4.1.2 Thermal Conversion of N_2O_5 in the Cavity under Ambient Conditions

As discussed in section 2.2.10, the thermal conversion of N_2O_5 to NO_3 and NO_2 is rapid at high temperatures. For ambient measurements of N_2O_5 , the expected mixing ratios of N_2O_5 are much less than those used in the laboratory experiments. The effect of thermal conversion of N_2O_5 to NO_3 and NO_2 (R1.6) was modeled under typical ambient conditions. Figure 4-3 and Figure 4-4 show the modeled results for the thermal conversion of N_2O_5 to NO_3 and NO_2 for a typical N_2O_5 ambient measurement. Thermal conversion occurs within 0.5 seconds. The extent of the thermal conversion depends on the ambient NO_3 and NO_2 concentrations. For an ambient NO_2 mixing ratio of 20 ppb, roughly 95% of the N_2O_5 is converted, whereas for 50 ppb NO_2 roughly 87% of the initial N_2O_5 is converted to NO_3 . High NO_2 conditions (>20 ppb) require higher temperatures to ensure maximum conversion of the N_2O_5 to NO_3 , although as seen previously (Section 3.2.4) the tradeoff is additional losses of NO_3 at higher temperatures.

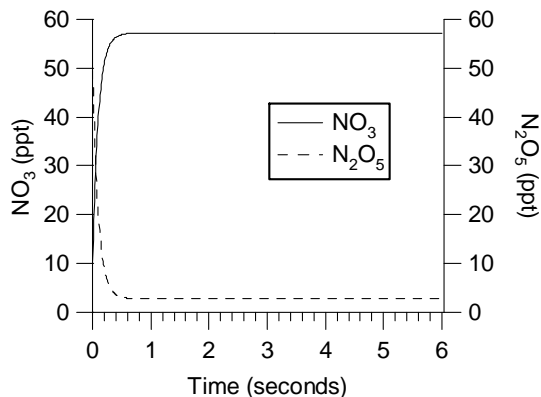


Figure 4-3 Simulation of thermal conversion of N_2O_5 to NO_3 at 353 K with 20 ppb NO_2 initially ($NO_3 = 10$ ppt, $N_2O_5 = 50$ ppt)

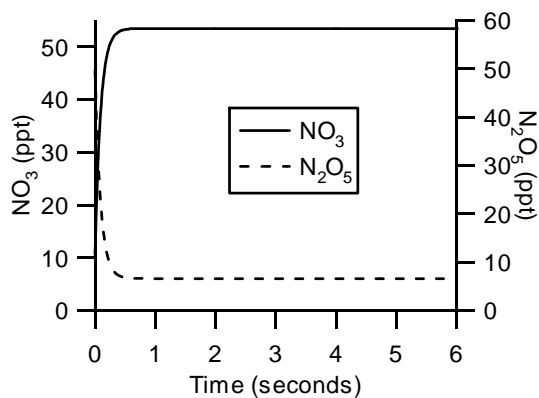


Figure 4-4 Simulation of thermal conversion of N_2O_5 to NO_3 at 353 K with 50 ppb NO_2 initially ($NO_3 = 10$ ppt, $N_2O_5 = 50$ ppt)

4.1.3 NO_3 and N_2O_5 Measurement Site

The ambient study of NO_3 and N_2O_5 was performed in the summer of 2007 for roughly four weeks. The site was located at the southeast corner on the rooftop of a four-storey parking structure (PS2) at York University. York University is located in

north Toronto, a large urban centre, and in close proximity to several major highways (400, 401 and 407) as well as being surrounded by several major streets. The instrument was located outside and the ambient air was sampled directly to the cavity due to the high reactivity of NO_3 to minimize sampling losses. Air could be sampled from all directions free of obstructions, with the exception of east, the location of an adjacent mechanical room.

When not in use, the instrument was stored in the mechanical room and was wheeled outside 1 to 2 hours prior to sunset. The gas cylinders remained in the mechanical room during measurements. Due to the rapid photolysis of NO_3 during the day, measurements began at twilight, when the low ambient light levels did not contribute to the detected signal. In addition, low ambient light levels were required for visibility during adjustments of the cavity. The detected cavity signal was periodically inspected and the alignment re-optimized when necessary.

Ambient O_3 was measured using a commercial O_3 monitor (Dasibi 1003-AH) and sampled from within 5' of the cavity inlet. Data were acquired every 10 seconds and stored.

4.2 Ambient NO_3 and N_2O_5 Measurements at York University

The NO_3 measured during the night of July 30 – 31, 2007 is shown in Figure 4-5 which includes the meteorological (Environment Canada, 2007) and O_3 data. The cavity was maintained at 35°C to reduce thermal drift as the night cooled. Figure 4-5 shows the

NO₃ mixing ratios corrected for the production of NO₂ from the titration of O₃ by the added NO during the background determination step (E3.4), as well as correction for wall and filter losses. To correct for wall and filter losses, positive NO₃ data points were multiplied by the wall and filter loss factor with the error bars equivalent to the standard deviation in τ . Negative NO₃ mixing ratios were not corrected for the wall and filter loss although the positive error bar represents the standard deviation in τ multiplied by the wall and filter loss factor.

At 35°C, the measurement is of NO₃ and includes a contribution from the thermal dissociation of N₂O₅. This contribution can be corrected for with knowledge of the ambient temperature and NO₂ mixing ratio. For example, for an ambient temperature of 298 K, and N₂O₅, NO₃ and NO₂ mixing ratios of 10 ppt, 1 ppt, and 10 ppb, respectively, roughly 1 ppt N₂O₅ (<10%) dissociates to NO₃ and NO₂ during the residence time of the heated section. The resulting measured NO₃ mixing ratio increases, with 50% of the NO₃ from N₂O₅ dissociation.

The O₃ profile from Figure 4-5 shows the typical trend for many of the nights of this study with a moderate buildup during the day and a rapid decrease after sunset. Sunset occurred at 20:43 on this date with twilight until 21:16 as shown in the figure by the grey vertical lines.

The period from 21:25 to 22:30 shows a slight peak in NO₃ concentration which decreases essentially to zero as O₃ decreases. This anti-correlation of observed NO₃ with

O₃ is expected, as the O₃ destruction (and thus NO₃) is predominantly due to reaction with NO from fresh emissions.

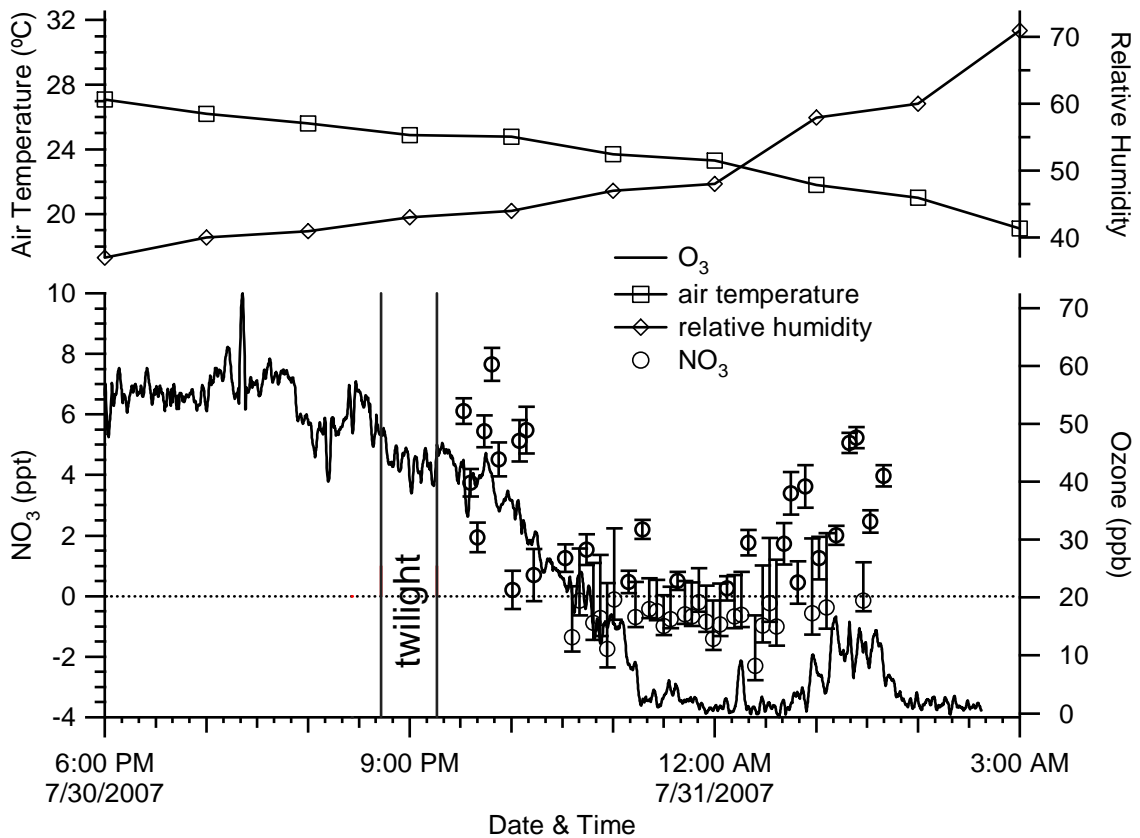


Figure 4-5 July 30 - 31, 2007, Meteorological conditions and NO₃ results of outdoor CRD for unheated inlet and cavity corrected for NO₂ production during background titration with NO and wall and filter losses. Positive data points were multiplied by the wall and filter loss factor with the error bars equivalent to the standard deviation in τ_0 ; Negative data points were not corrected for the wall and filter loss although the positive error bar represents the standard deviation in τ_0 multiplied by the wall and filter loss factor

Also of interest from Figure 4-5 is the potential rise in NO₃ after 1 am coinciding with a small increase in O₃ (up to about 15 ppb). This peak may be indicative of a breakthrough of the well mixed, low NO air from above the nocturnal boundary layer to

the measurement site (McLaren, *et al.*, 2004). As the relative humidity increases, condensation of water vapour onto particles releases heat producing local heating. This heated air rises and may cause air from above the nocturnal boundary layer to impact the measurement site.

From equation (E3.2), the detection limit can be estimated. The laser was modulated on and off at 73 Hz on this night, generating 73 ringdown signals in one second. The standard deviation of this 73 Hz ringdown data was roughly 1 μs yielding a standard deviation of the 90 second mean of 0.013 μs . This yields a 90 second detection limit of 0.51 ppt assuming that the uncertainty in the value for τ_0 is the largest source of error (section 3.2.3). Another method of determining the detection limit is to calculate the standard deviation of the NO_3 measured when the NO_3 mixing ratio is negligible. This can occur under conditions with very low O_3 mixing ratios, implying the presence of significant NO mixing ratios. During the period from 23:15 to 00:36 in Figure 4-5, the ozone is essentially zero. The average NO_3 mixing ratio for these 21 data points is -0.59 ± 0.65 ppt. The standard deviation of this result, 0.65 ppt, is equivalent to the 1σ detection limit. This detection limit is consistent with the 0.51 ppt calculated above using the ringdown times. Taking into account the residence time and the wall loss constant determined experimentally, $k_{\text{wall}} = 0.47 \text{ s}^{-1}$ (section 3.2.4.1), 63% of the NO_3 entering the cavity is lost to the walls. The wall loss contribution was calculated as the average fractional loss due to the first-order wall loss rate over the residence time interval within the cavity, detailed by the following relation (E4.2):

$$\left(\frac{\int_{t_1}^{t_2} e^{-k_{\text{wall}}t} dt}{t_2 - t_1} \right)^{-1} \quad (\text{E4.2})$$

With the wall loss contribution the detection limit for NO₃ becomes 1.77 ppt for a residence time within the cavity of 4.1 seconds.

Although not explicitly determined in this research, there are also losses of NO₃ when sampling through a filter. Using a similar filter, Brown *et al.* (2002b) determined the NO₃ filter loss to be 14 ± 6% for unloaded filters, and no significant loss of N₂O₅. Assuming a filter loss of 14%, the 1σ detection limit of NO₃ becomes 2.0 ppt. The positive NO₃ data points of Figure 4-5 were corrected for this wall and filter loss while for the negative points, the positive error bars were corrected for wall and filter losses. When accounting for the wall and filter losses, the small NO₃ peak following twilight is less than 10 ppt.

To measure N₂O₅, such as on the night of Aug 8 – 9, the cavity was heated to 85°C to thermally dissociate the ambient N₂O₅ to NO₃ and NO₂. The resulting measured signal is thus due to the sum of NO₃ and N₂O₅. The resulting NO₃ + N₂O₅ measured data, corrected for reaction of NO and O₃ is shown in Figure 4-6. The average of the experimentally determined NO₃ + N₂O₅ is -0.58 ± 0.79 ppt for these 20 points during this low ozone night. This results in a 1σ detection limit of 0.79 ppt, very similar to that determined from experiments measuring NO₃ alone. Taking into account a negligible

filter loss for N_2O_5 (Brown *et al.*, 2002b) and the wall loss contribution, the 1σ detection limit becomes 2.1 ppt.

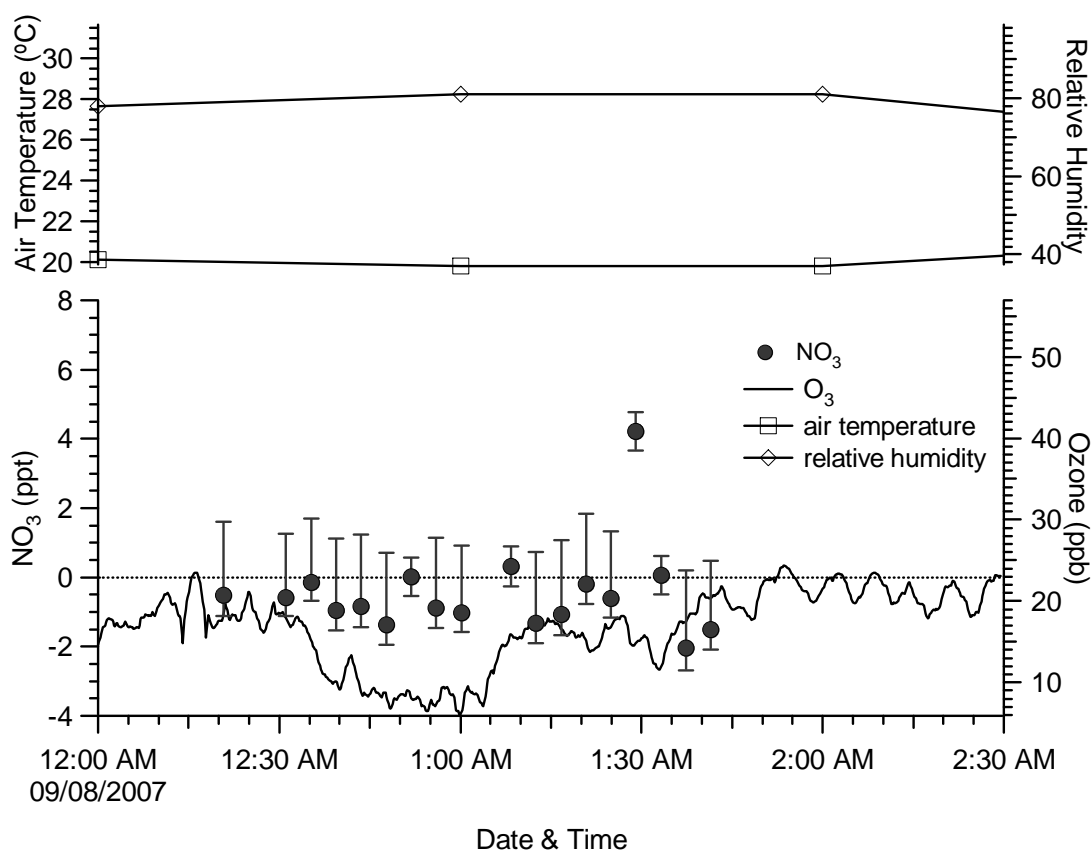


Figure 4-6 Aug 8 – 9, 2007 meteorological data and $N_2O_5 + NO_3$ ambient results of heated cavity corrected for wall loss and for NO_2 production during background titration with NO (as described in Figure 4-5)

4.3 Nitrate Radical Chemistry at York University

With the exception of the possible NO_3 peaks observed immediately after sunset and near midnight on the night of July 30 (Figure 4-5), NO_3 and N_2O_5 were below the

detection limit for all measurements. Table 4-1 shows a summary of the results of the nighttime measurements during the summer of 2007 at the York University location. Although the nighttime average NO₃ mixing ratio is often negative, the scatter of the individual data points is high, making a systematic negative bias inconclusive

Date	Nighttime Average NO ₃ (ppt)	Scatter of Average NO ₃ (1σ) (ppt)	Average Detection Limit (1σ) (ppt)	Ozone Level Prior to Sunset	Nighttime Ozone Profile
July 20 – 21	-4.1	4.1	0.5	20 ppb	Decreased to 15ppb after sunset
July 21 – 22	-0.7	5.2	0.9	33 ppb	Decreased steadily to 10 ppb
July 22 – 23	1.4	3.6	0.6	40 ppb	Decreased rapidly to zero
July 25 – 26	-1.2	4.1	0.6	60 ppb	Decreased to 40 ppb
July 26 – 27	-0.72	4.4	0.7	60 ppb	Decreased to 40 ppb
July 30 – 31	0.22 (see text)	1.2	0.5	See Figure 4-5	
July 31 - Aug. 1	0.70	2.8	0.4	50 ppb	Decreased rapidly to 15 ppb
Aug. 8 – 9	-0.38	2.6	0.6	40 ppb	Decreased to 20 ppb
Aug. 10 – 11	-0.88	1.42	0.4	40 ppb	Decreased to 20 ppb

Table 4-1 Summary of results of nighttime outdoor measurements at York University during the summer of 2007. All nights resulted in observed mixing ratios below the detection limits with the exception of July 30 – 31. Detection limits are based on the statistical detection limit given by equation E3.2. A summary of the ozone characteristics is also shown

During this study, typical ozone mixing ratios ranged from 40 to 60 ppb during the day and often dropped to a few ppb over the course of the night. This decrease in the ozone mixing ratio after sunset is due to dry deposition of O₃ and titration by fresh NO

emissions. After the O₃ reaches low levels, NO₃ production stops and the NO can increase, allowing previously produced NO₃ to be removed. The most likely time for maximum NO₃ mixing ratios for this site is just after sunset when photolysis no longer occurs and there is still significant O₃, allowing the NO₃ to build up.

Little NO is required for the atmospheric reaction of NO₃ and NO to be significant. For example, for 2 ppb ambient NO, the pseudo first-order rate constant for NO₃ loss is 1.3 s⁻¹. The expected NO₃ mixing ratio can be calculated assuming steady-state conditions (Brown *et al.*, 2003). Considering the production of NO₃ to be from reaction of NO₂ and O₃ (R1.1) and the loss to be due to reaction with NO, the steady-state mixing ratio of NO₃ is 0.2 ppt for 30 ppb O₃, 10 ppb NO₂ and 2 ppb NO at 298 K neglecting the contribution from the temperature dependent equilibrium with N₂O₅. Under these conditions the equilibrium N₂O₅ mixing ratio is 1.5 ppt. These steady-state mixing ratios are both below the detection limit of the instrument.

Due to the location of the measurement site, it is expected that NO mixing ratios would become significant at night due to the close proximity to three major highways, as well as frequently heavy local traffic. Preliminary data from a local Ontario Ministry of the Environment (OME) site showed nighttime hourly-averaged NO mixing ratios up to 20 ppb during the study period. These high NO mixing ratios account for the low NO₃ mixing ratios observed through much of this study.

The diurnal O₃ trend measured during this study is consistent with a previous air quality study performed at this same location (Campagnolo, 1994). Campagnolo (1994)

observed average nighttime NO mixing ratios for the months of July and August in the range of a few ppb to over 10 ppb, with the minimum occurring at sunset and rapidly increasing near midnight. Also observed in the 1994 study was the frequent occurrence of “titration” events, large spikes of NO for short durations, with mixing ratios upwards of 30 ppb. Campagnolo (1994) also observed a seasonal variation of NO mixing ratios with the monthly average nighttime NO peaking in the winter months, which was attributed to a lowering of the mixing layer thus confining the components to a smaller volume, increasing their concentration. With higher average NO mixing ratios during the winter months, it is expected that NO₃ would be lower in the winter at this location. In addition, with the rapid development growth near the location of the measurement site since the 1994 study it is expected that the impact of direct emissions, particularly that of NO, would be even higher at the present time.

Another potential loss of NO₃ is through the heterogeneous reaction of N₂O₅ with water to produce HNO₃. The relative humidity increases to relatively high values as the temperature decreases during the night, often reaching values in excess of 80%. The uptake coefficient, γ , the probability of reaction resulting from collisions of the gas molecules with the surface, for N₂O₅ has been measured in the range of 0.05 to 0.1 (Mozurkewich and Calvert, 1988), and is dependent on the relative humidity, temperature, and also the aerosol composition. Liquid water can be present on particles below saturation due to the hygroscopic properties of the particles. For example, ammonium bisulphate particles, NH₄HSO₄, a common component of particulate matter,

deliquesce above a relative humidity of 39.7% (Mozurkewich and Calvert, 1988). As the relative humidity increases, more liquid water is taken up by particles, increasing the efficiency of uptake of N_2O_5 on particles.

Based on the local atmospheric chemistry, NO_3 levels are expected to peak immediately after sunset, and steadily decrease as the night progresses. Therefore, NO_3 chemistry is most important during these early evening hours.

The nitrate radical can play a role as a nighttime oxidant of VOCs, with relative oxidizing capacity similar to that of OH during the day for some species, in particular, unsaturated hydrocarbons such as terpenes. Using a one-hour NO_3 mixing ratio of 2 ppt, the fractional loss rate per hour of various VOCs and CH_2O is shown in Table 4-2. The NO_3 reaction with CH_2O is important as it is a potential pathway for nighttime OH production (Platt *et al.* 1990). From the table, it can be seen that the relative hourly loss rate is typically higher for reaction with OH than with NO_3 with the exception of α -pinene. Even with the low NO_3 mixing ratios (<2 ppt) at this location, highly reactive species can still be impacted by oxidation with NO_3 .

VOC	OH	O ₃	NO ₃
Isoprene	0.89 (1.01×10 ⁻¹⁰)*	0.04 (1.43×10 ⁻¹⁷)*	0.11 (5.9×10 ⁻¹³)*
α-Pinene	0.48 (5.37×10 ⁻¹¹)*	0.23 (8.50×10 ⁻¹⁷)*	1.0 (5.8×10 ⁻¹²)*
β-Pinene	0.70 (7.89×10 ⁻¹¹)*	0.43 (1.60×10 ⁻¹⁷)*	0.42 (2.40×10 ⁻¹²)*
CH ₂ O	0.09 (9.77×10 ⁻¹²)*		0.00011 (6.0×10 ⁻¹⁶) [†]

Table 4-2 Fractional hourly loss rate for reaction of various VOCs with OH, O₃, and NO₃. Room temperature rate constants in brackets (cm³ molecule⁻¹ s⁻¹). OH, O₃, and NO₃ mixing ratios held constant at 0.1 ppt, 30 ppb and 2 ppt, respectively. References: * Atkinson (1990), †Platt et al. (1990)

Although prior to the outdoor experiments it was expected that the NO₃ would be negligible, the instrument performed well in this field study environment. Table 4-3 shows the detection limits of other studies of the nitrate radical, both cavity-based (CEA and CRD) and non cavity-based (laser induced fluorescence) as reported in the references. The optical detection limits (neglecting losses) obtained in this study compare very well with the other references.

Method	Optical DL	Experimental DL	Integration Time	Reference
cw-CEA	0.5ppt (1 σ)		5min	This work
cw-CRD	0.51ppt(1 σ)	2ppt	90s	This work
cw-CEA	220ppt(1 σ)		3s	Kasyutich <i>et al.</i> (2002)
cw-CRD	1.4ppt(2 σ)		5s	Ayers <i>et al.</i> (2005)
cw-CRD	1.6ppt(2 σ)	2.4ppt(2 σ)	25s	Simpson, 2003
cw-CRD	2ppt(1 σ)		30s	King <i>et al.</i> (2000)
pulsed CRD	0.4ppt (2 σ)	0.5ppt(2 σ)	5s	Brown <i>et al.</i> (2002a)
pulsed CRD		0.3ppt(1 σ)	50s	Brown <i>et al.</i> (2001)
LIF	4ppt(1 σ)		10min	Matsumoto <i>et al.</i> (2005)
cw-LIF	76ppt(2 σ)		60s	Wood <i>et al.</i> (2003)

Table 4-3 Comparison of detection limits of various nitrate radical based spectroscopic instruments with integration time and confidence levels as reported in the references. The optical detection limit is the instrumental performance based on the minimum detected fractional absorbance, whereas the experimental detection limit takes into account the system losses

5 CONCLUSIONS AND FUTURE WORK

The CEA/ICOS and CRD techniques were investigated for the measurement of trace atmospheric species with the aim to develop an instrument capable of atmospheric trace measurements. A CEA instrument was designed and built for measurement of CO, CO₂ and NH₃ in the near-IR. Software for data acquisition and control of the various modulation outputs was also successfully developed and applied. The experimentally determined detection limits (3σ) for CO₂ and NH₃ were 10 ppm and 10 ppb, respectively, while the estimated detection limits for H₂O, CH₄, and C₂H₂ were 8 ppm, 100 ppb, and 10 ppb, respectively. Although the cavity enhancement effect was significant, these detection limits are slightly too high for typical real-world measurements. The effective pathlengths were on the order of a few kilometers. These effective pathlengths corresponded to mirror reflectivities slightly lower than those specified, most likely due to extensive use and potential degradation over time. As mirrors with higher reflectivity become available for the near-IR, the effective pathlengths will increase, thus increasing the sensitivity of the technique in the near-IR.

The cavity enhanced technique was also applied to the visible region at 662 nm. In this spectral region, the cavity effects were visible to the naked eye, and the cavity mirrors available for this region exhibited much higher reflectivity than in the near-IR allowing for longer effective pathlengths.

The CEA/ICOS technique was investigated using NO₂ and O₃ as test and calibration gas sources. Based on the results of these tests the equivalent NO₃ detection limit was determined to be 1.2 ppt and 0.6 ppt (3σ) from the results from NO₂ and O₃ absorption respectively, in the absence of sampling losses. The effective pathlengths obtained were roughly 18 km and it was found that the pathlength and stability were dependent on the cavity alignment. One of the main drawbacks of the CEA/ICOS method was the requirement for calibration with either NO₂ or O₃ as the effective pathlength is not known. It was observed that the effective pathlengths varied widely, thus requiring frequent calibration. Frequent calibration also decreases the duty cycle of the sample measurement as the necessary calibration and background measurements take time.

The CRD technique was investigated for the detection of NO₃. This technique has the advantage of not requiring a calibration as the effective pathlength is implicitly known from the measured ringdown times in the absence of absorbing analyte. In addition, the sensitivity of this technique is generally superior as the resulting ringdown time is independent of the initial intensity. For laboratory experiments, the detection limit for NO₃ was 0.3 ppt ($\alpha = 1.5 \times 10^{-10} \text{ cm}^{-1}$) for a 5-minute average in the absence of sampling losses. The results from a simultaneous study of the ringdown and CEA techniques showed the ringdown technique to be generally more stable, sensitive and with the lack of required calibration, allowed for greater sample data acquisition.

Nighttime measurements of NO₃ were conducted at York University to test the instrument performance under ambient conditions. The NO₃ and N₂O₅ mixing ratios were below the detection limit during this study with the exception of a possible small peak occurring immediately after sunset on the night of July 30. During the study, the detection limit of the instrument for NO₃ was measured to be 2.0 ppt (1σ) with inclusion of wall and filter losses.

While the cavity ringdown instrument exhibited excellent stability and reproducibility under the controlled conditions of the laboratory, instabilities of the instrument in the field limited not only the detection limits but also reduced the amount of data acquisition. Modifications to the portable instrument would be required to increase stability and reproducibility for NO₃ measurements. Increased stability at higher flow rates will help to increase the sensitivity by reducing the impact of wall losses.

The cavity enhanced techniques for measurement of NO₃ could also be extended to investigate the kinetics of the oxidation of various species with NO₃ (Kasyutich *et al.*, 2002; Pfrang *et al.*, 2006) providing a highly sensitive method for laboratory NO₃ measurements.

With current and future technological advances, resonant optical cavity absorption techniques can be applied to other species in other regions of the spectrum. Application of the cavity ringdown and cavity enhanced absorption techniques has been recently extended to the mid-IR (Bakhirkin *et al.*, 2004; Kosterev *et al.*, 2001; Provencal *et al.*, 2005). Highly reflective mirrors are currently available for some regions of the mid-IR,

the spectral region containing fundamental vibrational absorption transitions. The recent introduction of the much more reliable quantum cascade lasers (QCLs) has made available a higher-powered alternative to lead salt lasers for such experiments.

In this research, various resonant optical cavity techniques were investigated for the measurement of trace gases. With the long effective pathlengths achievable in a compact instrument, these techniques provide high-sensitivity measurements and have the potential to find widespread application in studies of the composition and chemistry of the atmosphere.

6 REFERENCES

Anderson, D. Z., Alignment of resonant optical cavities, *Appl. Opt.*, **23**, 2944-2949, 1984.

Atkins, P. W., Physical chemistry, 2nd edition, W. H. Freeman and Company, San Francisco, 1982.

Atkinson, R., Gas-phase tropospheric chemistry of organic compounds: A review, *Atmos. Environ.*, **24A**, 1-41, 1990.

Ayers, J. D., R. L. Apodaca, W. R. Simpson, and D. S. Baer, Off-axis cavity ringdown spectroscopy: application to atmospheric nitrate radical detection, *Appl. Opt.*, **44**, 7239-7242, 2005.

Baer, D. S., J. P. Paul, M. Gupta, and A. O'Keefe, Sensitive absorption measurements in the near-infrared region using off-axis integrated-cavity-output spectroscopy, *Appl. Phys. B*, **75**, 261-265, 2002.

Bakhirkin, Y., A. Kosterev, C. Roller, R. Curl, and F. Tittel, Mid-infrared quantum cascade laser based off-axis integrated cavity output spectroscopy for biogenic nitric oxide detection, *Appl. Opt.*, **43**, 2257-2266, 2004.

Ball, S. M., I. M. Povey, E. G. Norton, and R. L. Jones, Broadband cavity ringdown spectroscopy of the NO₃ radical, *Chem. Phys. Lett*, **342**, 113-120, 2001.

Berden, G., R. Peeters, and G. Meijer, Cavity ring-down spectroscopy: experimental

- schemes and applications, *Int. Reviews in Physical Chemistry*, **19**, 565-607, 2000.
- Brassington, D. J., Tunable diode laser spectroscopy for the measurement of atmospheric species, in: R. J. H. Clark, R. E. Hester (eds.), *Spectroscopy in Environmental Science*, J. Wiley, New York, 1995.
- Braun, W., J. T. Herron, and D. K. Kahaner, Accuchem: a computer program for modeling complex reaction systems, *Int. J. Chem. Kinet.*, **20**, 51-62, 1988.
- Brown, S. S., H. Stark, S. J. Ciciora, R. J. McLaughlin, and A. R. Ravishankara, Simultaneous in situ detection of atmospheric NO₃ and N₂O₅ via cavity ring-down spectroscopy, *Rev. Sci. Instr.*, **73**, 3291-3301, 2002a.
- Brown, S. S., H. Stark, S. J. Ciciora, and A. R. Ravishankara, In-situ measurement of atmospheric NO₃ and N₂O₅ via cavity ring-down spectroscopy, *Geophys. Res. Lett.*, **28**, 3227-3230, 2001.
- Brown, S. S., H. Stark, and A. R. Ravishankara, Cavity ring-down spectroscopy for atmospheric trace gas detection: application to the nitrate radical (NO₃), *Appl. Phys. B*, **75**, 173-182, 2002b.
- Brown, S. S., H. Stark, and A. R. Ravishankara, Applicability of the steady state approximation to the interpretation of atmospheric observations of NO₃ and N₂O₅, *J. Geophys. Res.*, **108**, 4539-4548, 2003.
- Burrows, J. P., A. Dehn, B. Deters, S. Himmelmann, A. Richter, S. Voigt, and J. Orphal, Atmospheric remote-sensing reference data from GOME: 1. Temperature-

dependent absorption cross sections of NO₂ in the 231-794 nm range, *J. Quant. Spectrosc. Radiat. Transfer*, **60**, 1025-1031, 1998.

Burrows, J. P., A. Dehn, B. Deters, S. Himmelmann, A. Richter, S. Voigt, and J. Orphal, Atmospheric remote-sensing reference data from GOME: 2. Temperature-dependent absorption cross sections of O₃ in the 231-794 nm range, *J. Quant. Spectrosc. Radiat. Transfer*, **61**, 509-517, 1999.

Campagnolo, S., Characterization of the Toronto air mass, Honours Thesis, York University, Toronto, ON, Canada, 1994.

Cantrell, C. A., J. A. Davidson, A. H. McDaniel, R. E. Shetter, and J. G. Calvert, Infrared absorption cross sections for N₂O₅, *Chem. Phys. Lett.*, **148**, 358-363, 1988.

Curtis, A. R. and P. Sweetenham, FACSIMILE release H users manual, 1987.

Davidson, J. A., C. A. Cantrell, R. E. Shetter, A. H. McDaniel, and J. G. Calvert, The NO₃ radical decomposition and NO₃ scavenging in the troposphere, *J. Geophys. Res.*, **95**, 13,963-13,969, 1990.

Davidson, J. A., A. A. Viggiano, C. J. Howard, I. Dotan, F. C. Fehsenfeld, D. L. Albritton, and E. E. Ferguson, Rate constants for the reactions of O₂⁺, NO₂, NO⁺, H₃O, CO₃⁻, NO₂⁻, and halide ions with N₂O₅ at 300 K^{a)}, *J. Chem. Phys.*, **68**, 2085-2087, 1978.

Engeln, R., G. Berden, R. Peeters, and G. Meijer, Cavity enhanced absorption and cavity enhanced magnetic rotation, *Rev. Sci. Instr.*, **69**, 3763-3769, 1998.

Environment Canada, Canadian Climate Data,

http://www.climate.weatheroffice.gc.ca/climateData/canada_e.html, 2007.

Harrison, R. M. and N. K. Abdul-Massih, Estimation of the rate constant for the reaction of acid sulphate aerosol with NH_3 gas from atmospheric measurements, *J. Atmos. Chem.*, **15**, 133-143, 1992.

Herriott, D. and H. J. Schulte, Folded optical delay lines, *Appl. Opt.*, **4**, 883-889, 1965.

Hu, J. H. and J. P. D. Abbatt, Reaction probabilities for N_2O_5 hydrolysis on sulfuric acid and ammonium sulfate aerosols at room temperature, *J. Phys. Chem. A*, **101**, 871-879, 1997.

Johnston, H. S., C. A. Cantrell, and J. G. Calvert, Unimolecular decomposition of NO_3 to form NO and a review of $\text{N}_2\text{O}_5/\text{NO}_3$ kinetics, *J. Geophys. Res.*, **91**, 5159-5172, 1986.

Johnston, H. S., H. F. Davis, and Y. T. Lee, NO_3 photolysis product channels: quantum yields from observed energy thresholds, *J. Phys. Chem.*, **100**, 4713-4723, 1996.

Kasyutich, V. L., C. E. Canosa-Mas, C. Pfrang, S. Vaughan, and R. P. Wayne, Off-axis continuous-wave cavity-enhanced absorption spectroscopy of narrow-band and broad band absorbers using red diode lasers, *Appl. Phys. B*, **75**, 755-761, 2002.

King, M. D., E. M. Dick, and W. R. Simpson, A new method for the atmospheric detection of the nitrate radical (NO_3), *Atmos. Environ.*, **34**, 685-688, 2000.

- Kogelnik, H. and T. Li, Laser beams and resonators, *Appl. Opt.*, **5**, 1550-1567, 1966.
- Kosterev, A. A., A. L. Malinovsky, F. Tittel, C. Gmachl, F. Capasso, D. Sivco, J. Baillargeon, A. Hutchinson, and A. Cho, Cavity ringdown spectroscopic detection of nitric oxide with a continuous-wave quantum-cascade laser, *Appl. Opt.*, **40**, 5522-5529, 2001.
- Linde, D. E. e., CRC Handbook of Chemistry and Physics (85th ed.), 2004-2005, CRC Press, New York, 2005.
- Lundsberg-Neilson, L., F. Hegelund, and F. M. Nicolaisen, Analysis of the high-resolution spectrum of ammonia ($^{14}\text{NH}_3$) in the near-infrared Region, 6400-6900 cm^{-1} , *J. Mol. Spectrosc.*, **162**, 230-245, 1993.
- Matsumoto, J., N. Kosugi, H. Imai, and Y. Kajii, Development of a measurement system for nitrate radical and dinitrogen pentoxide using a thermal conversion/laser-induced fluorescence technique, *Rev. Sci. Instr.*, **76**, 064101, 2005.
- Mazurenka, M., A. J. Orr-Ewing, R. Peverall, and G. A. D. Ritchie, Cavity ring-down and cavity enhanced spectroscopy using diode lasers, *Annu. Rep. Prog. Chem., Sect. C*, **101**, 100-142, 2005.
- McLaren, R., R. A. Salmon, Liggio, J., Hayden, K. L., Anlauf, K. G., Leitch, W. R., Nighttime chemistry at a rural site in the Lower Fraser Valley, *Atmos. Environ.*, **38**, 5837-5848, 2004.
- McManus, J. B., P. L. Keabian, and M. S. Zahniser, Astigmatic mirror multipass

- absorption cells for long-path-length spectroscopy, *Appl. Opt.*, **34**, 3336-3348, 1995.
- Mozurkewich, M. and J. Calvert, Reaction probability of N₂O₅ on aqueous aerosols, *J. Geophys. Res.*, **93**, 15889-15896, 1988.
- Murphy, D. M. and Fahey, D. W., Mathematical treatment of the wall loss of a trace species in denuder and catalytic converter tubes, *Anal. Chem.* **59**, 2753-2759, 1987.
- O'Keefe, A. and D. A. G. Deacon, Cavity ring-down optical spectrometer for absorption measurements using pulsed laser sources, *Rev. Sci. Instrum.*, **59**, 2544-2551, 1988.
- Osborne, B. A., G. Marston, L. Kaminski, N. C. Jones, J. M. Gingell, N. Mason, I. C. Walker, J. Delwiche, and M.-J. Hubin-Franksin, Vacuum ultraviolet spectrum of dinitrogen pentoxide, *J. Quant. Spectrosc. Radiat. Transfer*, **64**, 67-74, 2000.
- Paul, J. P., L. Lapson, and J. G. Anderson, Ultrasensitive absorption spectroscopy with a high finesse optical cavity and off-axis alignment, *Appl. Opt.*, **40**, 4904-4910, 2001.
- Peeters, R., G. Berden, A. Apituley, and G. Meijer, Open-path trace gas detection of ammonia based on cavity-enhanced absorption spectroscopy, *Appl. Phys. B*, **71**, 231-236, 2000.
- Pfrang, C., R. S. Martin, C. E. Canosa-Mas, and R. P. Wayne, Gas-phase reactions of

- NO₃ and N₂O₅ with (Z)-hex-4-en-1-ol, (Z)-hex-3-en-1-ol ('leaf alcohol'), (E)-hex-3-en-1-ol, (Z)-hex-2-en-1-ol and (E)-hex-2-en-1-ol, *Phys. Chem. Chem. Phys.*, **8**, 354-363, 2006.
- Platt, U., D. Perner, A. M. Winer, G. W. Harris, and J. N. Pitts, Detection of NO₃ in the polluted troposphere by differential optical absorption, *Geophys. Res. Lett.*, **7**, 89, 1980.
- Platt, U. and F. Heintz, Nitrate radicals in tropospheric chemistry, *Isr. J. Chem.*, **34**, 289-300, 1994.
- Platt, U., G. LeBras, G. Poulet, J. P. Burrows, and G. Moortgat, Peroxy radicals from night-time reaction of NO₃ with organic compounds, *Nature*, **348**, 147-149, 1990.
- Platt, U. F., A. M. Winer, H. W. Biermann, R. Atkinson, and J. N. Pitts, Measurement of nitrate radical concentrations in continental air, *Environ. Sci. Technol.*, **18**, 365-369, 1984.
- Provencal, R., M. Gupta, T. G. Owano, D. S. Baer, K. N. Ricci, A. O'Keefe, and J. R. Podolske, Cavity-enhanced quantum-cascade laser-based instrument for carbon monoxide measurements, *Appl. Opt.*, **44**, 6712-6717, 2005.
- Romanini, D., A. A. Kachanov, N. Sadeghi, and F. Stoeckel, CW cavity ring down spectroscopy, *Chem. Phys. Lett.*, **264**, 316-322, 1997.
- Rothman, L. S., D. Jacquemart, A. Barbe, D. C. Benner, M. Birk, L. R. Brown, M. R. Carleer, C. Chackerian Jr., K. Chance, L. H. Coudert, V. Dana, V. M. Devi, J.-M.

Flaud, R. R. Gamache, A. Goldman, J.-M. Hartmann, K. W. Jucks, A. G. Maki, J.-Y. Mandin, S. T. Massie, J. Orphal, A. Perrin, C. P. Rinsland, M. A. H. Smith, J. Tennyson, R. N. Tolchenov, R. A. Toth, J. Vander Auwera, P. Varanasi, and G. Wagner, The HITRAN 2004 molecular spectroscopic database, *J. Quant. Spectrosc. Radiat. Transfer*, **96**, 139-204, 2004.

Russell, A. G., G. R. Cass, and J. H. Seinfeld, On some aspects of nighttime atmospheric chemistry, *Environ. Sci. Technol.*, **20**, 1167-1172, 1986.

Sander, S. P., R.R. Friedl, A. R. Ravishankara, D. M. Golden, C. E. Kolb, M. J. Kurylo, M. J. Molina, G. K. Moortgat, H. Keller-Rudek, B. J. Finlayson-Pitts, P. H. Wine, R. E. Huie, and V. L. Orkin, Chemical Kinetics and Photochemical Data for Use in Atmospheric Studies. Evaluation Number 15; JPL Publication 06-2, 2006.

Savitzky, A. and M. J. E. Golay, Smoothing and differentiation of data by simplified least squares procedures, *Anal. Chem.*, **36**, 1627-1639, 1964.

Seinfeld, J. H. and Pandis, S. N., Atmospheric chemistry and physics: from air pollution to climate change, J. Wiley, New York, 1998.

Silfvast, W. T., Laser Fundamentals, Cambridge University Press, New York, 1996.

Simpson, R. E., Introductory electronics for scientists and engineers, 2nd edition, Prentice Hall, Englewood Cliffs, New Jersey 07632, 1987.

Simpson, W. R., Continuous wave cavity ring-down spectroscopy applied to in situ detection of dinitrogen pentoxide (N_2O_5), *Rev. Sci. Instr.*, **74**, 3442-3452, 2003.

- Tsukahara, H., T. Ishida, and M. Mayumi, Gas-phase oxidation of nitric oxide: chemical kinetics and rate constant, *Nitric Oxide*, **3**, 191-198, 1999.
- Voigt, S., J. Orphal, and J. P. Burrows, High-resolution reference data by UV-visible Fourier-Transform Spectroscopy: 1. Absorption cross-sections of NO₂ in the 250-800 nm range at atmospheric temperatures (223-293 K) and pressures (100-1000 mbar), *Chem. Phys. Lett.*, in preparation.
- Voigt, S., J. Orphal, K. Bogumil, and J. P. Burrows, The temperature dependence (203-293 K) of the absorption cross-sections of O₃ in the 230-850 nm region measured by Fourier-Transform Spectroscopy, *J. Photochem. Photobiol. A.*, **143**, 1-9, 2001.
- Wayne, R. P., I. Barnes, P. Biggs, J. P. Burrows, C. E. Canosa-Mas, J. Hjorth, G. Lebras, G. K. Moortgat, D. Perner, G. Poulet, G. Restelli, and H. Sidebottom, The nitrate radical: Physics, chemistry, and the atmosphere, *Atmos. Environ.*, **25**, 1, 1991.
- Webber, M. E., D. S. Baer, and R. K. Hanson, Ammonia monitoring near 1.5 μm with diode-laser absorption sensors, *Appl. Opt.*, **40**, 2031-2042, 2001.
- Werle, P., R. Mücke, and F. Slemr, The limits of signal averaging in atmospheric trace-gas monitoring by tunable diode-laser absorption spectroscopy (TDLAS), *Appl. Phys. B*, **57**, 131-139, 1993.
- Wheeler, M. D., Stuart M. Newman, Andrew J. Orr-Ewing, and Michael N. R. Ashfold, Cavity ring-down spectroscopy, *J. Chem. Soc., Faraday Trans.*, **94**, 337-351, 1998.

Wood, E. C., P. J. Wooldridge, J. H. Freese, T. Albrecht, and R. C. Cohen, Prototype for in situ detection of atmospheric NO_3 and N_2O_5 via laser-induced fluorescence, *Environ. Sci. Technol.*, **37**, 5732-5738, 2003.

Yokelson, R. J., T. J. Christian, I. T. Bertschi, and W. M. Hao, Evaluation of absorption effects on measurements of ammonia, acetic acid, and methanol, *J. Geophys. Res.*, **108**, 4649-4657, 2003.

Yokelson, R. J., J. B. Burkholder, R. W. Fox, R. K. Talukdar, and A. R. Ravishankara, Temperature dependence of the NO_3 absorption spectrum, *J. Phys. Chem.*, **98**, 13144-13150, 1994.

Yu, F. T. S. and X. Yang, Introduction to optical engineering, Cambridge University Press, Cambridge, UK, 1997.